EXOPLANET SURFACE MAPPING

Simon van Oosterom

Delft University of Technology

Bachelor Thesis

*This space we declare to be infinite since neither
reason, convenience, possibility,
sense-perception
nor nature assign to it a limit.
In it are infinitly of worlds of the same kind*
as our own.

GIORDANO BRUNO

EXOPLANET SURFACE MAPPING

Author
SIMON VAN OOSTEROM

Supervised by
DR. PAUL M. VISSER
DR. AURÈLE J.L. ADAM
committee members
DR. IR. WOLTER GROENEVELT
DR. AKIRA ENDO
DR. DAPHNE STAM

TUDelft

Main Equations

Reflective light-curves for Lambertian reflection

Time domain
$$f(t) = \frac{1}{\pi R^2} \iint_{\mathbb{D}} (-\hat{\mathbf{r}} \cdot \hat{\mathbf{s}})(\hat{\mathbf{s}} \cdot \hat{\mathbf{o}}) M(\mathbf{s}, t) d^2 S$$

Fourier coefficients (edge-on)
$$f_k^n = \frac{s^2}{R^2} \sum_{l=|n|}^{\infty} \sum_{m=-l}^{l} \left[2(-1)^k c_k c_{k+n} y_l^{-n} d_l^{-n,m}(-\beta) e^{-i(m+n)\alpha} \right] M_l^m$$

Fourier coefficients (face-on)
$$f_k^n = \frac{2s^2}{R^2} (-1)^n c_n \delta_{n,-k} \sum_{l=|n|}^{\infty} \sum_{m=-l}^{l} y FO_l^{-n} d_l^{-nm}(-\beta) M_l^m$$

Nomenclature

A vector is displayed in boldface ($\mathbf{v}$), a unit vector is denoted with a hat ($\hat{\mathbf{v}}$)

s	Radius of the exoplanet
R	Radius of the star
I_0	Power output of the star
ω	Orbit angular velocity
Ω	Spin angular velocity
$\mathbf{r}$	Vector from the star to the planet
$\hat{\mathbf{n}}$	Spin axis of the planet
$\mathbf{s}$	Vector from the center of the planet to the surface
$\hat{\mathbf{o}}$	Vector from the star to the observer
$\mathbb{D}$	Part of the exoplanet that is both visible and illuminated
θ	Latitude
ϕ	Longitude
β	Obliquity of the exoplanet
α	Angle between Vernal equinox of the exoplanet and the observer
(α, β)	Axial-tilt of the exoplanet
θ_o	Orbital inclination, angle between the observer and the orbital plane
θ_p	Latitude of the exoplanet
ϕ_p	Longitude of the exoplanet
M	Albedo map in pixel basis
$\mathbf{M}$	Coefficients of the albedo map in the Y_l^m basis
$\mathbf{M}_L$	All coefficients from $\mathbf{M}$ corresponding to Y_l^m with $l \leq L$
f	LC in time domain
$\mathbf{f}$	Coefficients of LC in frequency domain
$\arg\max_{x \in X} g(x)$	The elements of X that maximize f
$\arg\min_{x \in X} g(x)$	The elements of X that minimize f

Abstract

In this thesis we consider the reconstruction of albedo maps of exoplanets. This is done with a new variant of spin-orbit tomography that has been described in [Cowan and Agol, 2008] and more in depth in [Fujii and Kawahara, 2012]. This method reconstructs the albedo map from the reflected-light curve, the total intensity of the light that originates from the host star and is reflected by the planet.

In the mentioned papers, the surface map of the planet is modeled as a sum of finite sized surface elements with constant albedo, and the relation between this approximation of the map and the light-curve in the time domain is determined. In this report, we use that the signal is quasi periodic due to diurnal and annual motion, and work with the Fourier peaks of the light-curve. We also approximate the map in a different way, writing it as the sum of spherical harmonics, and neglecting spherical harmonics with high spatial frequencies. This has the advantage that the relation can be worked out analytically (for edge-on and face-on observations) without the use of complex mathematics, and that both the surface map and the light-curve contain a daily frequency.

We derive an equation for the reflective light-curve under the assumption that the surface map is not a function of time (no clouds), and that the reflection is Lambertian (equal in magnitude in all directions). This transformation is found to be a linear function of the surface map. This equation is worked out for edge-on and face-on observations with arbitrary axial tilt, which describes the orientation of the spin axis with respect to the observer and the orbital plane. Furthermore, we describe how to invert this relation if the axial tilt is known to the observer.

We also aimed at recovering the map if the axial tilt is unknown to the observer, since this would make sure that the reconstruction does not rely on other observations. In contrast to what was found in papers like [Fujii and Kawahara, 2010] and [Fujii and Kawahara, 2012], we did not succeed in this. A number of methods were used for this. The first two looked at the problem from a mathematical perspective: the minimization of the distance between the measured light-curve and the light-curve from the reconstructed map, and Tikhonov regularization. The two failed because both the column space and the singular values respectively are not a function of the axial tilt. The third method that has been treated and tested involved the maximization of the 'amount' of positive albedo on the reconstructed map, but a test showed that the distinction that this method makes is in the same order of magnitude as the numerical error, thus proving that this method was not useful as well. Further study might show what causes the results of the two methods to differ in this respect.

(this page was intentionally left blank)

Contents

(this page was intentionally left blank)

INTRODUCTION

EXOPLANETS

For hundreds of years humans from all different disciplines: scientists, philosophers, and science fiction writers suspected that the notion of a planet was not limited to our solar system. This began in the sixteenth century, when the Italian frair (philosopher, mathematician and cosmological theorist) Giordano Bruno, an early supporter of heliocentrism, put forward the possibility of an infinite universe, and with it the idea of exoplanets [1] . This idea was way ahead of it's time, and was not developed for political reasons, but after the idea was mentioned again by Isaac Newton in his Principia, support for the idea began to grow.

But in spite of the strong believe in the existence of exoplanets, there was no way to observe them or to know their properties. It took humanity until 1988 for the first suspected scientific detection of an exoplanet occurred, and until 1992 to confirm the discovery. The first exoplanet known to man: the planets orbiting the star PSR B1257+12 was found [NASA, 2018] Currently, 3964 exoplanets have been confirmed and 3520 candidates are waiting verification. It is estimated that the number of exoplanets in this galaxy is exceeds a trillion.

The huge distance between us and even the nearest exoplanets unfortunately makes direct imaging of the planet a nearly impossible job. There have been direct observations of a few, but the vast majority have been detected through indirect methods. Most of the indirectly observed planets have been discovered via the transit method, as shown in figure 1 [2]. When a planet orbits its star, and the observer (we) is looking at it at a sufficiently small angle, the planet will move in front of the star and block some of the light. If such an event is observed, we can conclude that there is an exoplanet. A simulation of such a transit can be seen in figure 1b, where Jupiter and two of its moons are transiting the Sun.

EXO-CARTOGRAPHY AND SPIN-ORBIT TOMOGRAPHY

One of the ultimate goals in the study of exoplanets is to answer the open question of the existence of extraterrestrial life. The so-called spectral biomarkers, the spectral lines of molecules of which the presence is necessary for life as we know to exist, will play a vital part in the search for life on the candidate exoplanets [Fujii and Kawahara, 2011].

But the objective of the study of exoplanets is not limited to the discovery of other lifeforms. There are theories which have been developed, such as plate tectonics, of which properties cannot be empirically tested without exoplanets. We can, for example, not test whether or not plate tectonics occurs depends on the mass of the planet because we only have the Earth to test the theory on. But if we could determine the surface of exoplanets, we might find an answer [Cowan, 2014]. This is the field of exo-cartography. The aspect of exo-cartography that will be focused on, is the reflectivity (or albedo) of a planet.

Exo-carthography and the limits of technology

The problem with this field is one of the obvious kind: the limits of human technology. Suppose that we observe some distant solar system with a star and one or more planets, located at a distance D from the observer, as seen in figure 2. Zoom in on one planet. The planet orbits the star in an approximately circular orbit with radius R, which is orders of magnitude magnitudes larger then the radius of the planet

---

[1]For this idea (amongst other ones), Bruno was excommunicated by the Catholic church, the Calvinists and Lutherists, and was convicted by the Inquisition.

[2]Other methods for discovering exoplanets include the radial velocity method, in which one measures the periodic Doppler shift in the light from the star, and the gravitational micro-lensing method, which uses the property that light 'curves' around a heavy object.
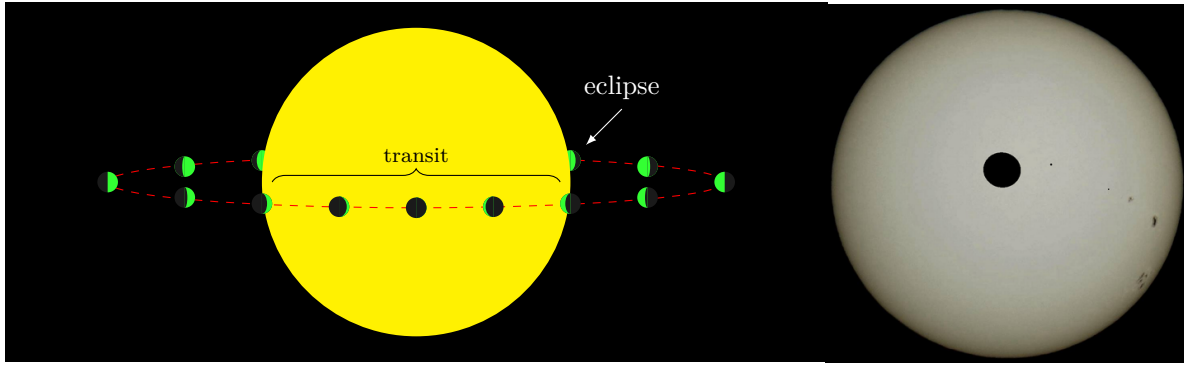
(a) *Transit monitoring of an exoplanet*

(b) *A simulated view of Jupiter and two of its moons transiting the sun.*

Figure 1: *Transit monitoring, a method for the detection of exoplanets and possibly their surface. When a planet is moving in front of the star, and is the star, planet and observant (us) are in the same plane, the light from the star that reaches the observer drops. This portion is proportional to the square of the ratio or the radii of the star and the planet.*

itself, s. If the planet were large enough, the observer would take multiple photographs of the planet with his or her telescope and 'sew' them together to construct a map. For this to work, we would need a telescope with an angular resolution which is at least $a_1 \approx s/D$ radians. Since we work with visible light rays, the diffraction limit gives us the required diameter of said telescope:

$$d_1 = \frac{1.22\lambda}{a_1} \approx 24 \text{ kilometers} \tag{1}$$

depending on the size of the planet and the wavelength, this being an exoplanet with the size of the earth (12 742km) at a distance of 10 Parsecs (3×10^{14}km) and blue light ($\lambda = 400$nm) [Cowan and Fujii, 2017]. Even though this value may vary from situation to situation, a telescope with this diameter is beyond our technological capabilities.

A method to observe the surface without direct imaging

From the year 2005 and on, a technique has been in development that can image the surface of an exoplanet without the use of direct imaging [3].

Consider the planet from figure 2. One half of the planet is visible to the observer and another half is illuminated by the star. Let ☽ be the intersection of these two hemispheres. Suppose that we cannot measure the details on the surface of the planet, but have a telescope that allows us to measure the total intensity of the light that is emitted by the star and reflected by the planet in our direction. This is referred to as the reflected light-curve. This signal is a function of the surface map in ☽. When the planet is rotating around its own axis (daily rotation) and around the star (annual), the surface on ☽, and the signal, changes in time. So information about the surface of the planet is transmitted via the reflected light-curve. Reconstructing the surface map is the inverse problem.

Even though the planet is at least a thousand times fainter than the star, there have been measurements of this signal. An example of the variation in the light-curve over a year can be seen in figure 3. One can see that between a transit and an eclipse, the the brightness becomes smaller due to the reduction of the size of ☽. The opposite is happening when the planet is moving from eclipse to transit. With the assurance that such data was available, [Cowan and Agol, 2008] recreated a longitudinal brightness map by 2008 [4]. From 2010 and on, this method was expanded in [Fujii and Kawahara, 2010] with latitudinal variations in the map, and the influence of clouds was added in [Fujii and Kawahara, 2011] and [Fujii and Kawahara, 2012]. They also introduced the name that this technique goes by: Spin-Orbit Tomography (or SOT). Since then, there have been advances in the field, amongst others, the detection of oceans or polar caps [Visser and van der Bult, 2015].

---

[3]The groundwork for this theory had actually already been established in the beginning of the twentieth century by Henry Russel, see [Russel, 1905] and [Russel, 1916]

[4]Before that, a day-night contrast map was made in [Knutson et al., 2007]

In this report, a new variation of SOT is explored. If we use the techniques as proposed over here, we only need to know the angle with which we look at the star system. This angle can be deduced from observation of the orbit of the exoplanet and the assumption that this orbit is circular. Thus, it suffices to have a telescope with angular resolution $a_2 \approx R/D$ (see figure 2), which gives a required diameter (with the same values as before, but taking $R = 10^4 s$):

$$d_2 = \frac{1.22\lambda}{a_2} \approx 2.4 \text{ meters} \tag{2}$$

Which is a fairly reasonable size. To get an even better measurement of the light-curve, occulters are used that block out light from the host star [Cowan and Fujii, 2017]. In all articles mentioned prior, the
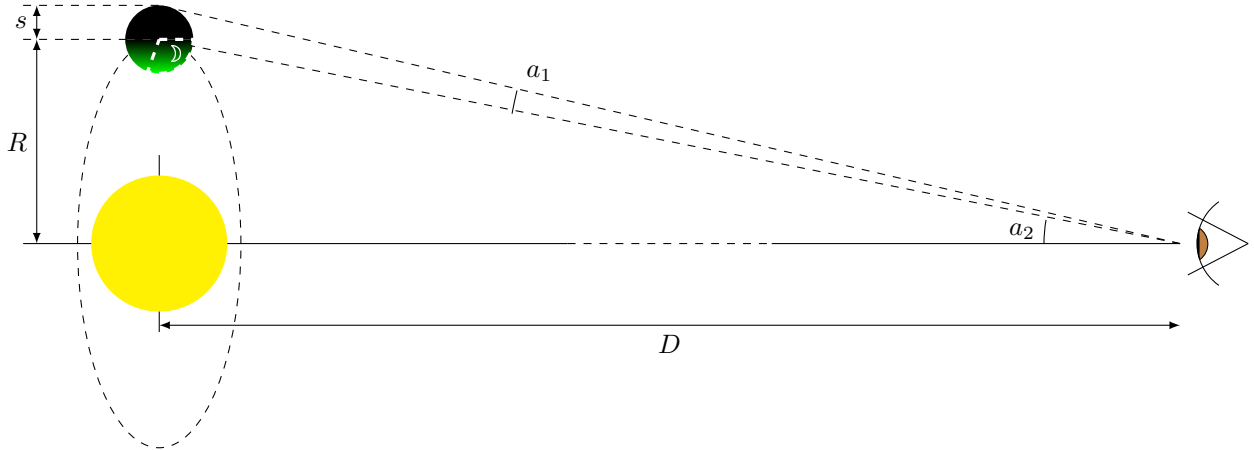
Figure 2: *The required angular resolution for observation of the surface of exoplanets. An exoplanet with radius s is orbiting the star at a distance R. The observer is located at a distance D from the solar system and needs an resolution $a_1 = s/D$ to observe the surface of the planet with direct imaging and $a_2 = R/D$ with the technique from this report.*

albedo map of the exoplanet has been split up in discrete parts; finite sized pixels. Over time, each of the pixels contributes to the signal in its own specific manner. In this report, a variation of SOT, is explored. Instead of decomposing the surface map in pixels and work with the signal as a function of time, the map is decomposed in spherical harmonics and the signal in its frequency components. This has a number of advantages:

1. The transformation from the surface map to the signal can be determined without numerical approximations (albeit with the help of *Mathematica*). This gives valuable insight in the process.

2. The analysis of the Fourier transform of the signal allows the observer to separate one process from another: the signal from different planets can be separated, as well as the influence of moons.

The contents of this report has been divided in four chapters. In the first chapter, we start by introducing the medium though which we shall recover the albedo map, called the reflective light-curve. In the second chapter, a function for the light-curve will be determined for the simplest of observations (but with a arbitrary map), along with a method to inverse this function in this situation. In chapter 3, the axial tilt of a exoplanet is introduced, and it's effects on the light-curve are determined. In the last chapter, a number of methods to retrieve the map along with the axial tilt of the planet are discussed.

Finally, a couple of assumptions are made throughout this report:

1. Circular orbits

2. Absence of clouds

3. Absence of moons

4. General Time-invariance of the surface map

5. Light is not absorbed by the atmosphere

This bachelor thesis has been supervised by Dr. Paul Visser and Dr. Aurèle Adam. For similar reports on exoplanets, see [Mol, 2018] for an analysis of eclipses by exomoons, and [Beekman, 2016] for an analysis of reflected light-curves for non-spherical objects.
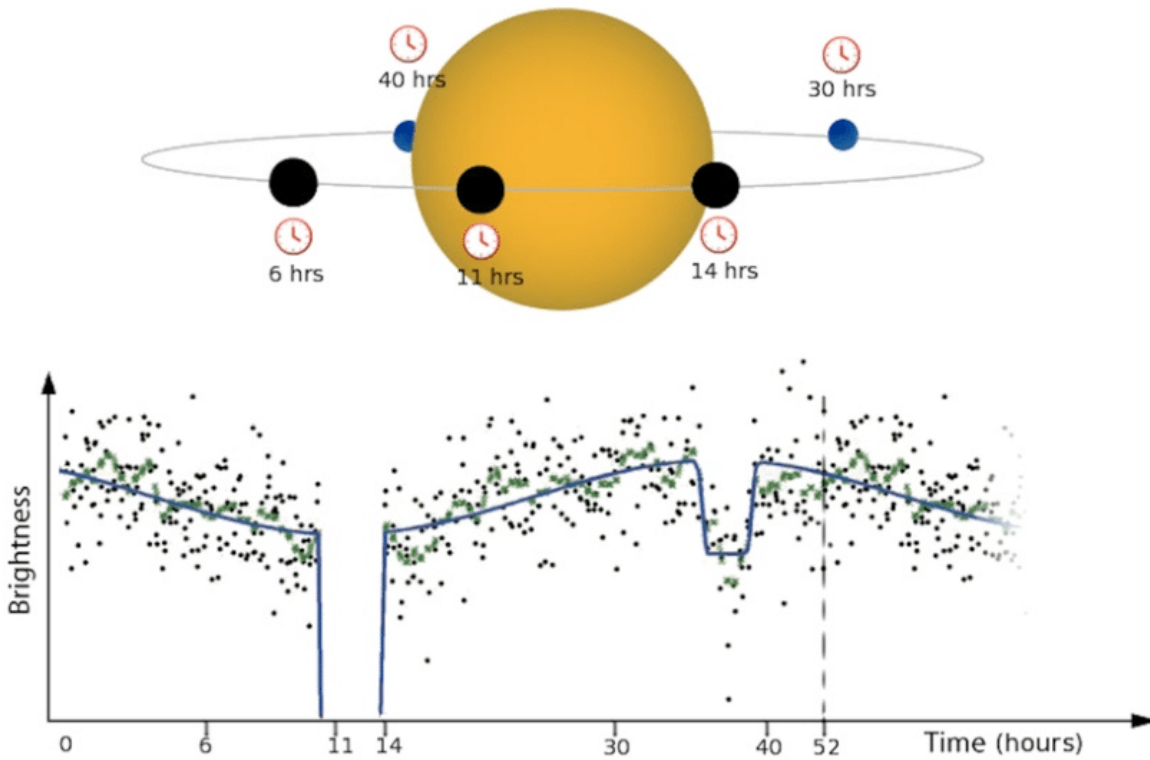
Figure 3: *Measured annual variation in the light-curve of HAT-P-7b. measurements by [Borucki et al., 2009], figure by [Tinetti et al., 2012]. The large dip (at 11 hours) is the transit, the small dip (at 35 hours) is the eclipse. The overall variation is the sum of solar light and reflected light.*

CHAPTER 1

THE REFLECTIVE LIGHT-CURVE OF A PLANET

In this chapter we will see how the we can describe a light-curve, a one-dimensional signal dependent on the reflective properties of an exoplanet. In later chapters we shall use this knowledge to invert this mapping. In the first section, the parameters that describe the planet we presume to observe are introduced, and we derive the light-curve. In the second section, shall apply this formula. We work out the light-curve for a simple albedo map, and we derive a numerical expression which allows us to compute the light-curve for any map.

1.1   Parameters

Have a look at figure 1.1: this is the general case we shall study in this report. A solar system with one planet, and with a star located at the origin. The planet is moving in a circular orbit with radius R around the star and mean motion (angular frequency) ω, it's position is denoted by $\mathbf{r}$. The angle corresponding to this motion is denoted by ϕ, and is given by $\phi = \omega t$. Furthermore, the planet is spinning with angular frequency Ω around it's own spin axis, $\hat{\mathbf{n}}$ (the vector from the south pole to the north pole). The angle that the spin covered is given by Φ, $\Phi = \Omega t$. See the table below:

Motion	Angular frequency	Angle
Spin	Ω	$\Phi = \Omega t$
Orbit	ω	$\phi = \omega t$

We choose the basis vectors $\hat{\mathbf{x}}$, $\hat{\mathbf{y}}$ and $\hat{\mathbf{z}}$ such that the x-y plane is the orbital plane, and $\hat{\mathbf{x}}$ is parallel to the projection of $\hat{\mathbf{o}}$ on the x-y plane. The observer of the system (telescope) remains on Earth, with time-independent position, $\mathbf{o}$ ('o' for *o*bserver). In spherical coordinates, these vectors are:

$$\mathbf{r} = R \begin{pmatrix} \cos \omega t \\ \sin \omega t \\ 0 \end{pmatrix} \quad \hat{\mathbf{n}} = \begin{pmatrix} \cos \alpha \sin \beta \\ \sin \alpha \sin \beta \\ \cos \beta \end{pmatrix} \quad \mathbf{o} = R_o \begin{pmatrix} \sin \theta_o \\ 0 \\ \cos \theta_o \end{pmatrix} \quad \mathbf{s} = s \begin{pmatrix} \cos \phi_p \sin \theta_p \\ \sin \phi_p \sin \theta_p \\ \cos \theta_p \end{pmatrix} = s \begin{pmatrix} \cos \phi_p \sqrt{1 - z^2} \\ \sin \phi_p \sqrt{1 - z^2} \\ z \end{pmatrix}$$

$$(1.1)$$

where $\alpha, \beta, \theta_o, \theta_p$ and ϕ_p are spherical coordinates. ϕ_p and z are cylindrical coordinates. Furthermore, any point on the planet surface is given by the vector $\mathbf{s}$, the vector from the center of the planet to the surface.

Remark. *There are a few special cases of the polar angles which we are going to study. The edge-on and the face on position. For edge-on observation, the observer is in the star-planet plane: $\theta_o = \pi/2$. For face-on observation, the observer is perpendicular to the (star-planet) orbital plane, and thus $\theta_o = 0$ or $\theta_o = \pi$. A planet is said to be non-inclinated if $\beta = 0$, and $\mathbf{n}$ is thus perpendicular to the star-planet plane.*

Remark. *We assume that the distance from the observer to the solar system, R_o, is at least multiple orders of magnitude larger than R. But since we are talking about exoplanets, this is not a real limitation at all. We are dealing with planets outside our own solar system, the closest exoplanet we know of*
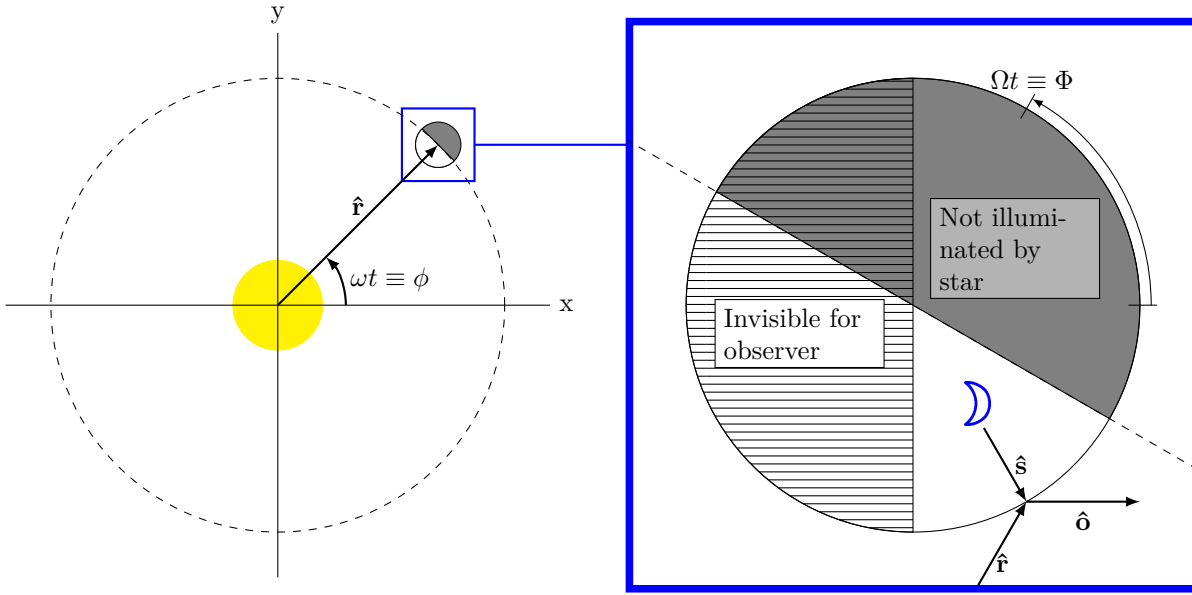
Figure 1.1: *The planet is moving in a circular orbit in the xy-plane, making an angle $\phi = \omega t$ with the x-axis. The planet is spinning around it's axis, making an angle of $\Phi = \Omega t$. Light from the star comes in from $\boldsymbol{r}$, and part of it is reflected in the direction of the observer: $\hat{\boldsymbol{o}}$. The part of the planet that is illuminated by the star and visible to the observer is indicated by $\mathbb{D}$.*

is Proxima Centrauri b which orbits Proxima Centauri. R is limited to approximately 10.000 ls, so $R/R_0 > 4.2ly/10.000ls \approx 13 \times 10^3$ so this assumption is not really a constraint.

We are interested in the reflectivity of the planet's surface, but as explained in the introduction, we do not have the resolution to resolve inhomogeneities on the planet by direct imaging. What could be measured is the total light that is reflected towards us, this physical quantity is the reflective light-curve of an exoplanet, and it is denoted with f:

Definition 1.1. *A reflective light-curve f of a planet is the total intensity of the light that has been emitted by its host star, reflected by the planet's surface, and recieved by the observer.*

When the planet rotates around the star and spins around its own axes, different parts (e.g. continents) face the star and the observer. If the reflectivity changes, the light-curve changes along with it. In this model, we shall assume that there is only one planet (with no moons) that orbits the star. As a result of this, the light-curve is dependent on the location and orientation of the planet, the angles ϕ and Φ respectively. And since these angles are both a function of time, we can say that:

$$f = f(\phi, \Phi) = f(\omega t, \Omega t) = f(t)$$

Thus, if we know the configuration of the planet (reflectivity map and axial tilt), we can calculate the light-curve. Furthermore, from the fact that we must have $f(\phi + 2\pi, \Phi) = f(\phi, \Phi)$ and $f(\phi, \Phi + 2\pi) = f(\phi, \Phi)$, the light-curve is quasi periodic. Therefore, we can represent f with it's Fourier coefficients (see for example [Oppenheim, 2014] or [Hecht, 2017]):

$$f(\phi, \Phi) = \sum_{k=-\infty}^{\infty} \sum_{n=-\infty}^{\infty} f_k^n e^{i(k\phi + n\Phi)} \qquad \text{with} \qquad f_k^n = \frac{1}{(2\pi)^2} \int_0^{2\pi} \int_0^{2\pi} f(\phi, \Phi) e^{-i(k\phi + n\Phi)} d\phi d\Phi$$

and thus:

$$f(t) = \sum_{k=-\infty}^{\infty} \sum_{n=-\infty}^{\infty} f_k^n e^{i(k\omega + n\Omega)t} = \sum_{k=-\infty}^{\infty} \sum_{n=-\infty}^{\infty} f_k^n e^{i\nu_{n,k} t}$$

Where $k, n \in \mathbb{Z}$. As long as f_k^n decreases sufficiently fast for large values of $|k|$, and ω and Ω differ sufficiently (for example, Earth has $\Omega \approx 365.25\omega$), we can retrieve f_k^n by looking at the Fourier transform of f. Such a transform can be seen in figure 1.2. Since f is a real signal, the Fourier transform is conjugate symmetric around frequency $\nu = 0$.
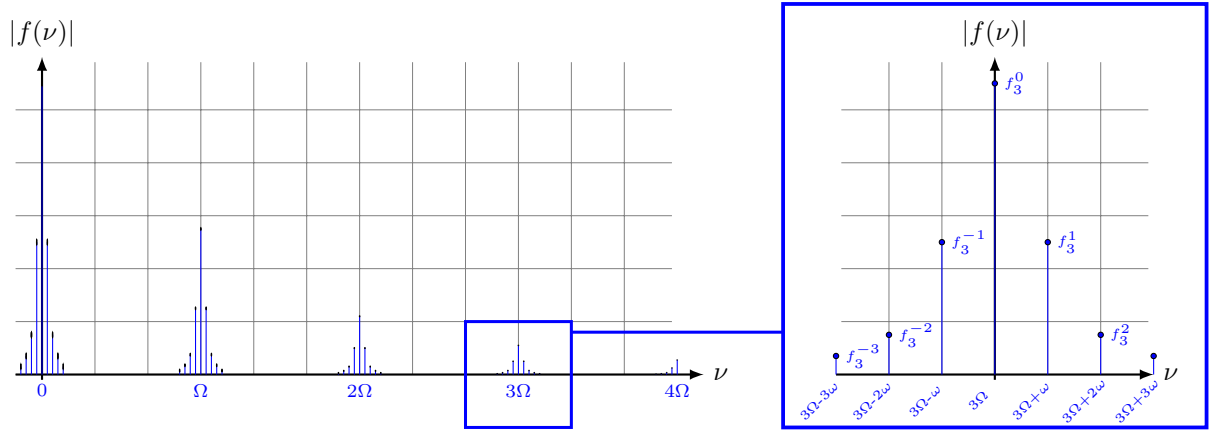
Figure 1.2: *The absolute value of the Fourier transform of the light-curve f for a planet with orbital angular frequency ω and spinning angular frequency $\Omega(=30\omega)$.*

1.2 The light-curve formula for Lambertian reflection

The fact that the scattering of light is a complex process with more than one mechanism, such as mirror-like reflection from oceans and absorption in the atmosphere, makes it impossible to know the exact value of the light-curve. We can however limit ourselves to a planet if which the entire surface is Lambertian [Koppal, 2014]:

Definition 1.2. *Lambertian reflectance is a scene property that distributes the energy from any incident illumination into all viewing directions equally. A Lambertian map consists only of points with Lambertian reflectance.*

This will allow us to compute the light-curve. Let's start: we need to account for the fact that not the entire surface of the planet contributes to the signal, see figure 1.1. It is always dark on one hemisphere, and the observer can only see one hemisphere at a time. The part of the planet that is illuminated by the star is characterized by $\hat{\mathbf{s}} \cdot \hat{\mathbf{r}} < 0$, and the part of the planet which is visible to the observer has $\hat{\mathbf{s}} \cdot \hat{\mathbf{o}} > 0$. Thus, the surface domain from which the observer receives light, denoted by $\mathbb{D}$ is given by:

$$\mathbb{D} = \{\mathbf{s} : \hat{\mathbf{s}} \cdot \hat{\mathbf{r}} < 0 \wedge \hat{\mathbf{s}} \cdot \hat{\mathbf{o}} > 0\}$$

We split up $\mathbb{D}$ in pieces of $\mathrm{d}^2\mathbf{S}$ located at $\mathbf{s}$. What the observer receives is given by a multiplication of four terms, each describing a "event" in the journey of the light from the star to the observer:

$$\text{observed intensity} = \text{star power} \times$$
$$\text{fraction that reaches the surface} \times$$
$$\text{surface reflectivity} \times$$
$$\text{fraction of reflected light that reaches observer}$$

We call the total power of the star I_0. At distance R from the sun, the intensity has decreased to $I_0/4\pi R^2$. The power that the surface receives is given by the intensity times the frontal surface, given by $-(\hat{\mathbf{r}} \cdot \hat{\mathbf{s}})d^2S$. The surface reflectivity is given by the albedo map or surface map:

Definition 1.3. *The albedo/surface map of a planet, M, maps any point on the surface of the planet to the interval $[0,1]$ according to their reflectivity. $M = 0$ corresponds with total absorption and $M = 1$ with total reflection.*

We can only define the albedo map if we assume Lambertian reflection, since otherwise, the reflection could not only depend on the location on the location of the point on the planet, but also on the locations of the star and the observer. To calculate the fraction of the light reflected by the planet that reaches the observer, we use this surface map. The fraction is again proportional to the frontal surface $\hat{\mathbf{s}} \cdot \hat{\mathbf{o}} d^2\Omega_o$, where $d^2\Omega_o$ is the solid angle of the observer. We need to normalize it such that the integral over all

directions is equal to 1 (the observer that completely surrounds the surface would receive all reflected light if $M = 1$), it follows from:

$$\iint (\hat{\mathbf{s}} \cdot \hat{\mathbf{o}}) d^2\Omega_o = \int_0^{\pi/2} \int_0^{2\pi} \begin{pmatrix} 0 \\ 0 \\ 1 \end{pmatrix} \cdot \begin{pmatrix} \cos\theta\sin\phi \\ \sin\theta\sin\phi \\ \cos\phi \end{pmatrix} \sin(\phi) d\theta d\phi = 2\pi \left[\frac{\sin^2\phi}{2} \right]_0^{\pi/2} = \pi$$

that the received fraction is given by $\hat{\mathbf{s}} \cdot \hat{\mathbf{o}} d^2\Omega_o / \pi$.

We now have all the ingredients to calculate the contribution of a small area of the surface to the light received by the observer. Multiplying these gives net reflected power of:

$$I_0 M(\mathbf{s}) \frac{(-\hat{\mathbf{r}} \cdot \hat{\mathbf{s}})(\hat{\mathbf{s}} \cdot \hat{\mathbf{o}})}{4\pi^2 R^2} d^2 S d^2\Omega_o$$

Astronomers can compare this small variation to the total light emitted by the star that reaches them, which is given by $\frac{I_0}{4\pi} d^2\Omega_o$, so we divide by that term. Now we integrate what's left of the light of surface area $d^2 S$ over $\mathbb{D}$. This gives the light-curve for Lambertian reflection:

$$f(t) = \frac{1}{\pi R^2} \iint_{\mathbb{D}} (-\hat{\mathbf{r}} \cdot \hat{\mathbf{s}})(\hat{\mathbf{s}} \cdot \hat{\mathbf{o}}) M(\mathbf{s}, t) d^2 S \tag{1.2}$$

This is the general equation, and starting from this we can derive the light curve for any situation.

1.2.1   EXAMPLE: EDGE-ON OBSERVATION OF A HOMOGENEOUS PLANET

We now look at the simplest case to work out equation 1.2, the planet is homogeneous (say $M = 1$), and the observation is edge-on ($\phi_o = \pi/2$). This means that the whether or not a point on planet surface $\mathbf{s}$ is in $\mathbb{D}$ does not depend on the z coordinate of $\mathbf{s}$, such that we use cylindrical coordinates:

$$\mathbf{s} = s(\sqrt{1 - z^2}\cos\phi_p, \sqrt{1 - z^2}\sin\phi_p, z)^T$$

where $(\phi_p, z) \in [-\pi, \pi] \times [-1, 1]$. The advantage is that $\mathbb{D}$ only depends on ϕ_p:

$$\mathbb{D} = \{(\phi_p, z) : z \in [-1, 1] \wedge \phi_p \in I(t)\}$$

where I is given by $[-\pi/2, -\pi/2 + o]$ for $0 < \phi < \pi$ and $[\pi/2 + o, \pi/2]$ for $-\pi < \phi < 0$. Working out the inner products gives us:

$$\hat{\mathbf{s}} \cdot \hat{\mathbf{r}} = \sqrt{1 - z^2}(\cos\phi_p \cos o + \sin\phi_p \sin o) = \sqrt{1 - z^2}\cos(\phi_p - o)$$
$$\hat{\mathbf{s}} \cdot \hat{\mathbf{o}} = \sqrt{1 - z^2}\cos\phi_p$$

Therefore the integrand becomes $(1 - z^2)\cos(\phi_p)\cos(\phi_p - o)$, and the differential element $d^2 S$ is given by:

$$d^2 S = \left| \frac{\partial \mathbf{s}}{\partial \phi_p} \times \frac{\partial \mathbf{s}}{\partial z} \right| dz d\phi_p = s^2 dz d\phi_p$$

Filling in this expression gives:

$$\begin{aligned}
f(t) &= -\frac{1}{\pi R^2} \int_{-1}^{1} \int_{I(t)} s^2 (1 - z^2) \cos\phi_p \cos(\phi_p - \omega t) d\phi_p dz \\
&= -\frac{s^2}{\pi R^2} \left[z - \frac{z^3}{3} \right]_{-1}^{1} \left[\frac{2\phi_p \cos(\omega t) - \sin(\omega t - 2\phi_p))}{4} \right]_{I(t)} \\
&= \frac{s^2}{3\pi R^2} \begin{cases} +2\omega t \cos\omega t - 2\sin\omega t & \text{for } 0 < \omega t < \pi \\ -2\omega t \cos\omega t + 2\sin\omega t & \text{for } -\pi < \omega t < 0 \end{cases} \\
&= \frac{2s^2}{3\pi R^2} \left(|\omega t| \cos|\omega t| - 2\sin|\omega t| \right)
\end{aligned} \tag{1.3}$$

for $|\omega t| < \pi$, A graph of this can be seen in figure 1.3.
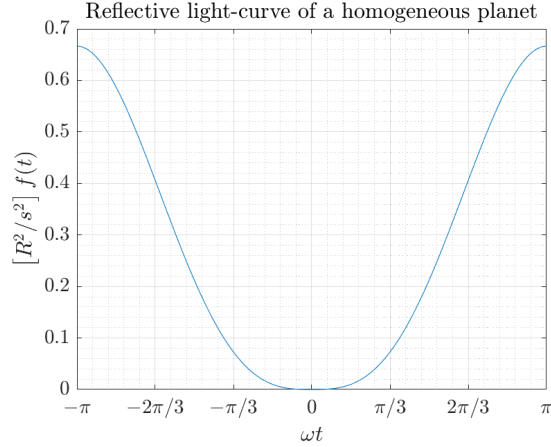
Figure 1.3: *Light signal f as a function of the orbital phase angle ωt(dimensionless unit) of a homogeneous planet that orbits the star with (angular) frequency ω, from equation 1.3.*

1.3 Numerical calculation of the light-curve for Earths albedo map

The last section delivered the general equation for the light-curve, but if we find ourselves in need of simulating a light-curve of a random planet, the equation is only useful if we have a description for the albedo on every point on the map. In this section we shall derive a method to determine the light-curve that works if we have a discrete number of data points for the albedo map.

1.3.1 THE NUMERICAL LIGHT-CURVE FORMULA FOR LAMBERTIAN REFLECTION

Suppose our map is on a grid with dimensions k_{max} by j_{max}, described by a matrix with entries $M_{k,j}$, corresponding to respectively the θ_p and ϕ_p direction (an equirectangular projection of the map). We work out the integral in equation 1.2 with these variables in the coordinate system of the planet itself, which means that a given coordinate (θ_p, ϕ_p) points to the same point on the map for any time. As a consequence of this choice, we have to rotate our vectors in the inertial system ($\hat{\mathbf{o}}$ and $\hat{\mathbf{r}}$) with the rotation: $\mathbf{v}' = R_z(-\Omega t)R_y(-\beta)R_z(-\alpha)\mathbf{v}$, which gets them in the planet's system. We also have to deal with the implicit expression for $\mathcal{D}$, and we can do this by introducing the function $(\hat{\mathbf{s}}\cdot\hat{\mathbf{v}})^+$ [1]. By applying this function to $\hat{\mathbf{o}}'$ and $-\hat{\mathbf{r}}'$m the light-curve becomes:

$$f(t) = \frac{1}{\pi R^2} \oiint (\hat{\mathbf{s}} \cdot \hat{\mathbf{o}}')^+ (\hat{\mathbf{s}} \cdot -\hat{\mathbf{r}}')^+ M(\hat{\mathbf{s}}) d^2 S$$

$$= \frac{s^2}{\pi R^2} \int_0^\pi \int_0^{2\pi} (\hat{\mathbf{s}} \cdot \hat{\mathbf{o}}')^+ (\hat{\mathbf{s}} \cdot -\hat{\mathbf{r}}')^+ M(\theta_p, \phi_p) \sin(\theta_p) d\phi_p d\theta_p$$

If we discretize the integral on the given data points, we get:

$$f(t) = \frac{s^2}{\pi R^2} \sum_{j=0}^{j_{max}} \sum_{k=0}^{k_{max}} [\hat{\mathbf{s}}(\theta_{p,k}, \phi_{p,j}) \cdot \hat{\mathbf{o}}']^+ [\hat{\mathbf{s}}(\theta_{p,k}, \phi_{p,j}) \cdot -\hat{\mathbf{r}}']^+ (\hat{\mathbf{s}}(\theta_{p,k}, \phi_{p,j})) \sin(\theta_{p,k}) M_{j,k} \Delta\theta_p \Delta\phi_p \quad (1.4)$$

$$\Delta\theta_p = \frac{\pi}{k_{max}} \qquad \Delta\phi_p = \frac{2\pi}{j_{max}} \qquad \theta_{p,k} = k\Delta\theta_p$$

$$\phi_{p,j} = j\Delta\phi_p \qquad M_{j,k} = M(\phi_{p,j}, \theta_{p,k})$$

---

[1] We define the function g^+ by $g^+(x) \equiv \max\{0, g(x)\}$

1.3.2 APPLICATION TO EARTH

In this subsection, Equation 1.2 is applied to Earth. An albedo map from NASA is used [NASA, 2017a], which can be seen in figure 1.4.
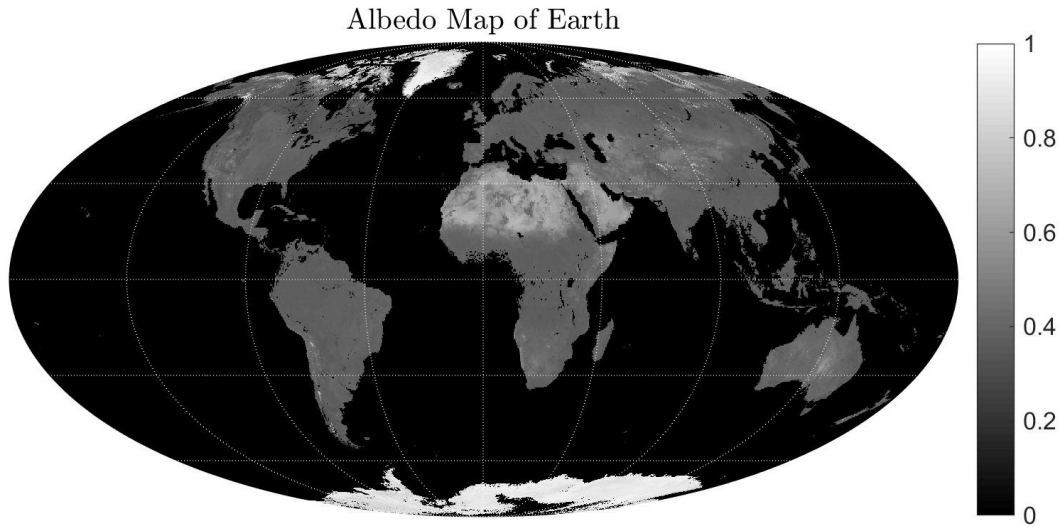
Albedo Map of Earth

Figure 1.4: *Albedo map of Earth as recorded by NASA in september 2017 [NASA, 2017a], integrated over all visible wavelengths. White denotes high albedo while black indicates low albedo.*

Two versions of the Earths light-curve have been constructed. In the first case, $\beta = 0°$, which means that the spin axis is perpendicular to the orbital plane. This case is interesting for us, and it is build upon in chapter 2. Next we have a situation with a tilted spin axis, taking the actual value of the inclination: $\beta = 23°$. In both simulations, we have edge-on observation and $\alpha = 0$.

The annual variation in the light-curve of Earth can be seen in figures 1.5 and 1.6. The black line denotes the light-curve, sampled every hour. The other (green and blue) lines represent the light curve when sampled with a period of exactly 24 hours. The diurnal variation in the light-curve of Earth when it is on the opposite side of the sun as the observer can be seen in figure 1.7a. The "visible" part of the Earth can be seen below the graph, showing that the signal is minimal when the pacific is facing the observer, and maximal when Africa and central Asia face the observer. Finally, the (absolute value of the) Fourier transform of the light-curve for $\beta = 23°$ can be seen in figure 1.8, illustrating how the value's of ω and Ω can be recovered.

As can be seen, at $t = 0$, and $t = 365$ days the signal is 0, reflecting the fact that the earth is directly between the observer and the star. Of course, the signal would also be 0 exactly in between these two times, when the planet is eclipsed by the star. However, this would only occur in an exact edge-on observation.
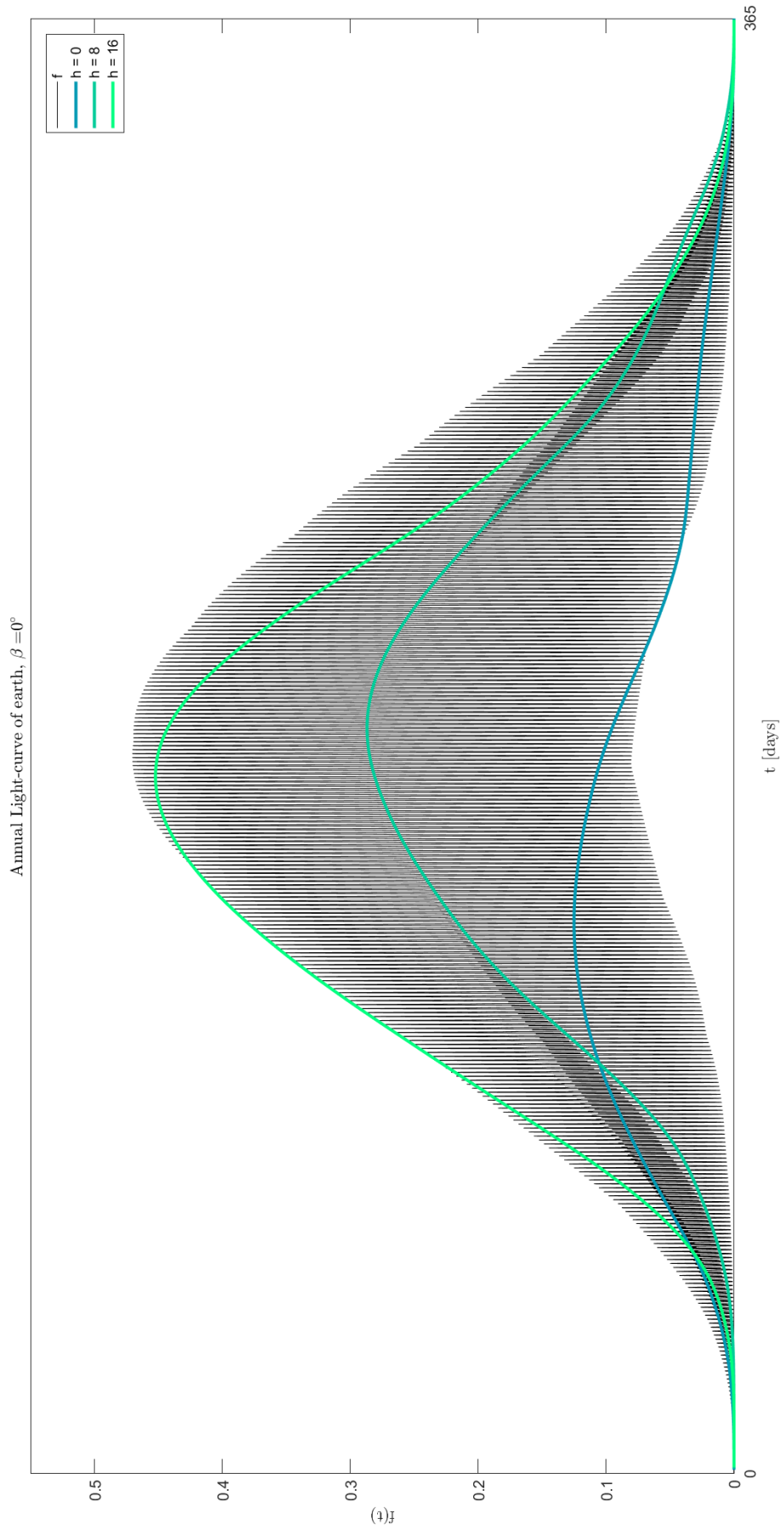
Figure 1.5: *Annual variation in the light-curve. The green and blue lines indicate light-curve sampled with a period of 24 hours (at 8 AM, 4 PM and at midnight with respect to GMT).*
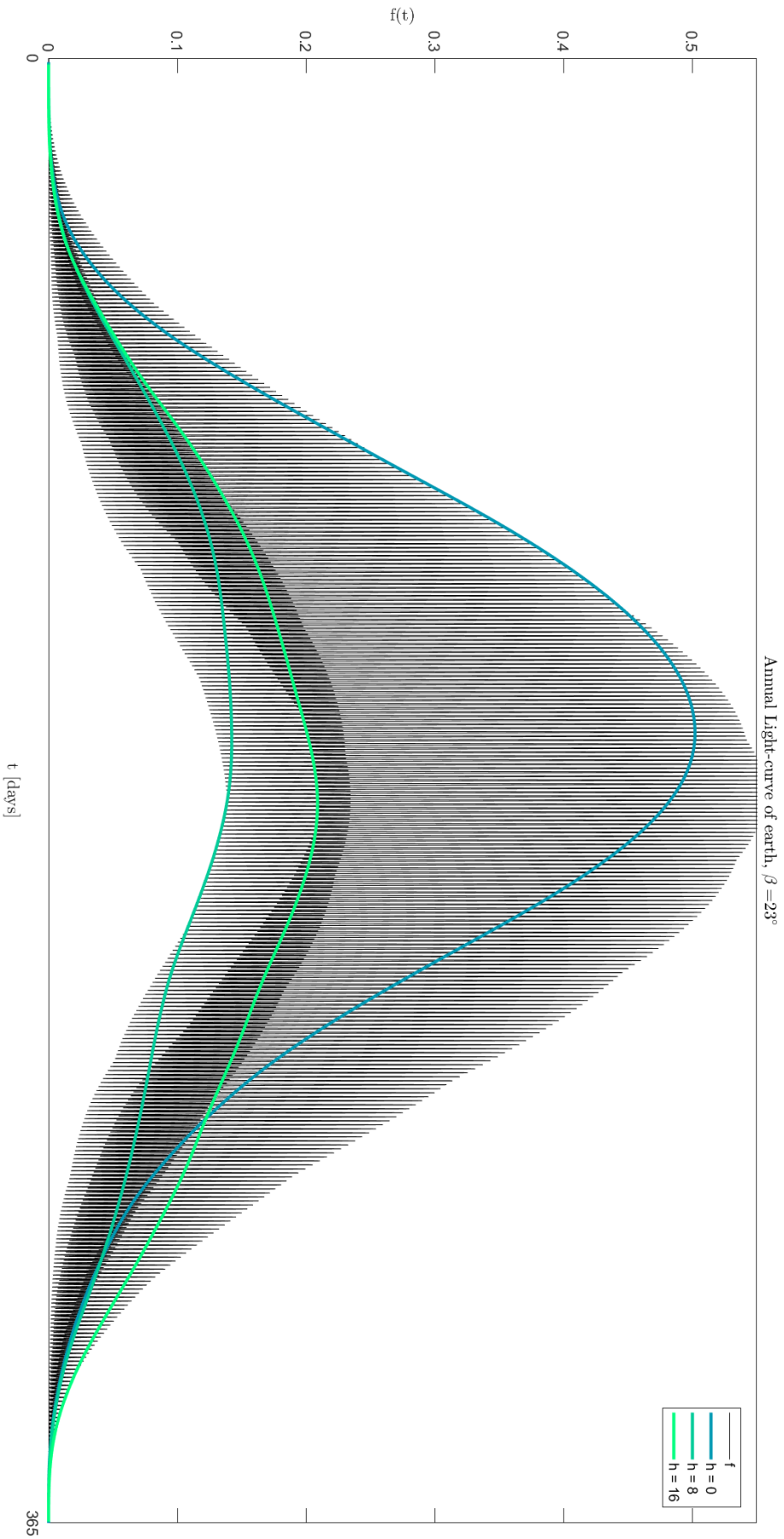
Figure 1.6: *Annual variation in the light-curve. The green and blue lines indicate light-curve sampled with a period of 24 hours (at 8 AM, 4 PM and at midnight with respect to GMT).*

Light-curve for one day period, $\beta = 0°$
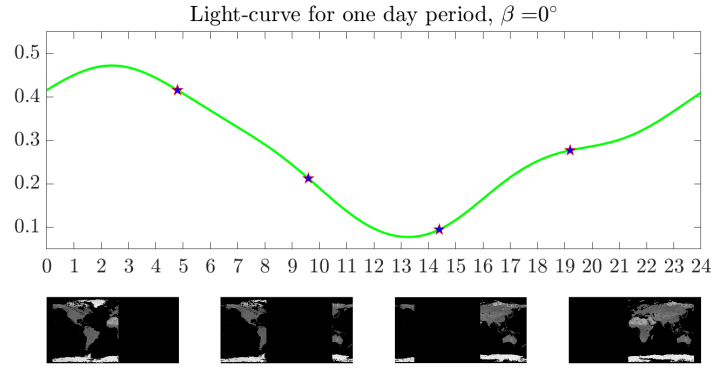
(a) *Diurnal light-curve for a situation without axial tilt, during the time that the star is approximately in-between the observer and the planet (full phase).*

Light-curve for one day period, $\beta = 23°$
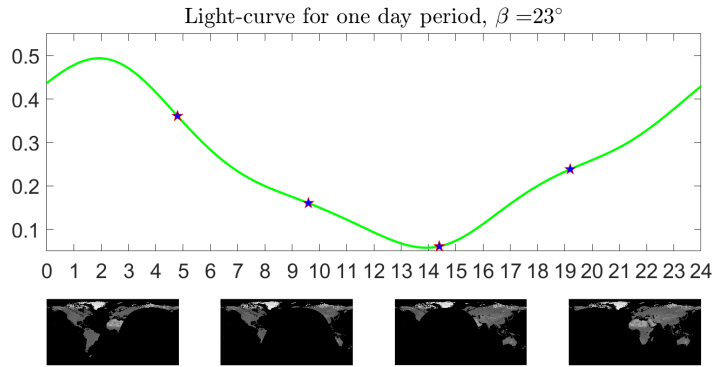
(b) *Diurnal light-curve for a situation with axial tilt $\beta = 23°$, during summer solstice on the northern hemisphere (21 June). The star is approximately in-between the observer and the planet (full phase).*

Figure 1.7: *Diurnal light-curve of the albedo map of Earth, for two different values of the axial tilt, and edge-on observation.*
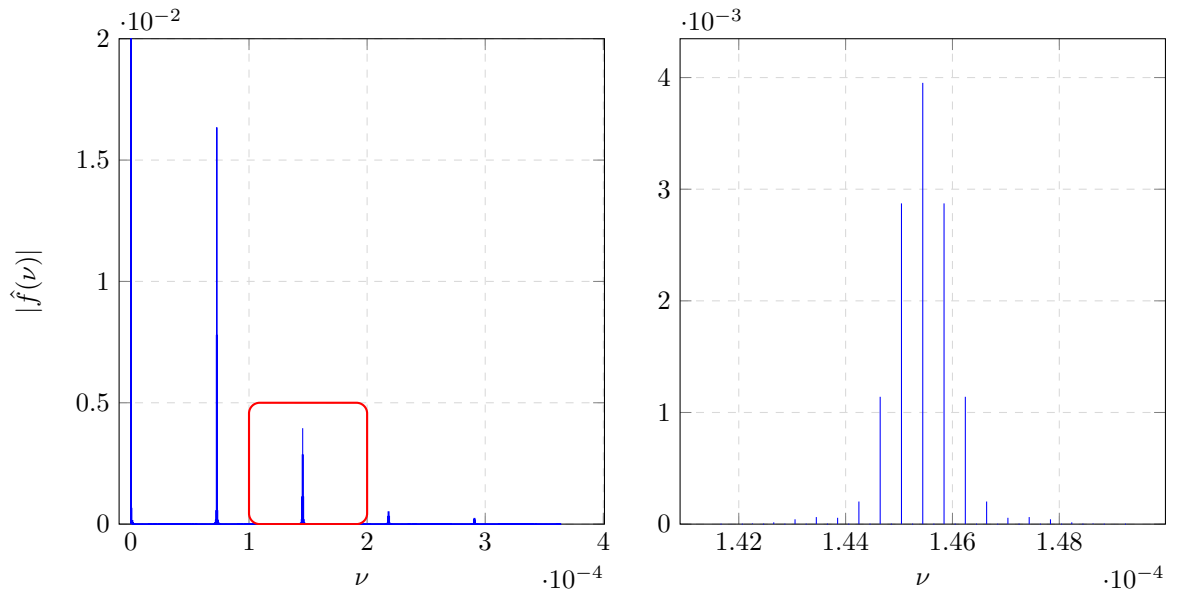
Figure 1.8: *Fourier transform of the light-curve of the Earth for $\beta = 23°$. On the left, the horizontal range 5Ω (the vertical axis has been limited for visibility purposes), while on the right, the range is $2\Omega \pm 20\omega$.*

CHAPTER 2

MAPPING A PLANET WITH ZERO TILT

In the first chapter of this report, we saw that we can write the light-curve of an exoplanet as a linear function of its albedo map, see equation 1.2. For the inversion of this transformation this property shall be exploited by decomposing the light-curve and the albedo map on two different orthogonal bases such that we can write this equation in matrix-vector notation. Firstly, in paragraph 2.1, we shall describe the decomposition. Secondly, in sections 2.2 and 2.3, we shall work out the transformation for exoplanets without axial tilt for edge-on and face-on observations respectively, and in section 2.4 a method will be described to invert the transformations if the axial tilt is known to the observer. Finally, the theory is applied to the albedo map of Earth.

2.1   Decomposing the signal and albedo map

Recall that in chapter 1, it was shown that the light-curve is quasi-periodic and can be written as a combination of complex exponentials. Furthermore, the amplitudes of these exponentials can be recovered from the Fourier-transform of the light-curve. This gives the following expression for f:

$$f(\phi, \Phi) = \sum_{n=-\infty}^{\infty} \sum_{k=-\infty}^{\infty} f_k^n e^{i(k\phi + n\Phi)} \tag{2.1}$$

$$f_k^n = \frac{1}{(2\pi)^2} \int_0^{2\pi} \int_0^{2\pi} f(\phi, \Phi) e^{-i(k\phi + n\Phi)} d\phi d\Phi \tag{2.2}$$

where $k\omega$ is the orbital frequency, describing the motion of the planet around the star, and $n\Omega$ is the spin-frequency, describing the motion of the planet around its own axis.

The albedo map, M, can be decomposed in terms of the spherical harmonics Y_l^m. The definition of the spherical harmonics which shall be used in this report (also: [Griffiths, 2004] and [Wikipedia, 2018b]), as well as some properties, are listed in Appendix A. With spherical coordinates (θ_p, ϕ_p), The decomposition of the albedo map is given by the following equations:

$$M(\theta_p, \phi_p) = \sum_{l=0}^{\infty} \sum_{m=-l}^{l} M_l^m Y_l^m(\theta_p, \phi_p) \tag{2.3}$$

$$M_l^m = \frac{1}{4\pi} \int_0^{2\pi} \int_0^{\pi} M(\theta_p, \phi_p) Y_l^m(\theta_p, \phi_p) \sin\theta_p d\phi_p d\theta_p \tag{2.4}$$

Such a decomposition can be seen in figure 2.1, applied to the albedo map of Earth. The original albedo map is displayed in the upper left panel, and in each of the other panels the function $\sum_{l=0}^{l_{max}} \sum_{m=-l}^{l} M_l^m Y_l^m(\theta_p, \phi_p)$ is displayed for different values of L. Due to the fact that only a finite number of spherical harmonics are used and the presence of Gibbs phenomena, the surface map becomes negative at some points. In this, and all of the following figures, negative values are displayed as black.

There are a number of reasons for the use of spherical harmonics. Firstly, the advantage that they have over a discretization of the map into pixels (as can be seen in reference), is that the matrix components

of the transformation can be calculated analytically, giving insight in the process. Furthermore, there are two coefficients that are associated with rotation around the spin axis: n and m, which will be helpful. The advantage that the spherical harmonics have over a two dimensional Fourier series is that spherical harmonics lie 'naturally' on a spherical surface: the values of the spherical harmonics on the north- and south pole are irrespective of the longitude, thus not creating any discontinuities there.
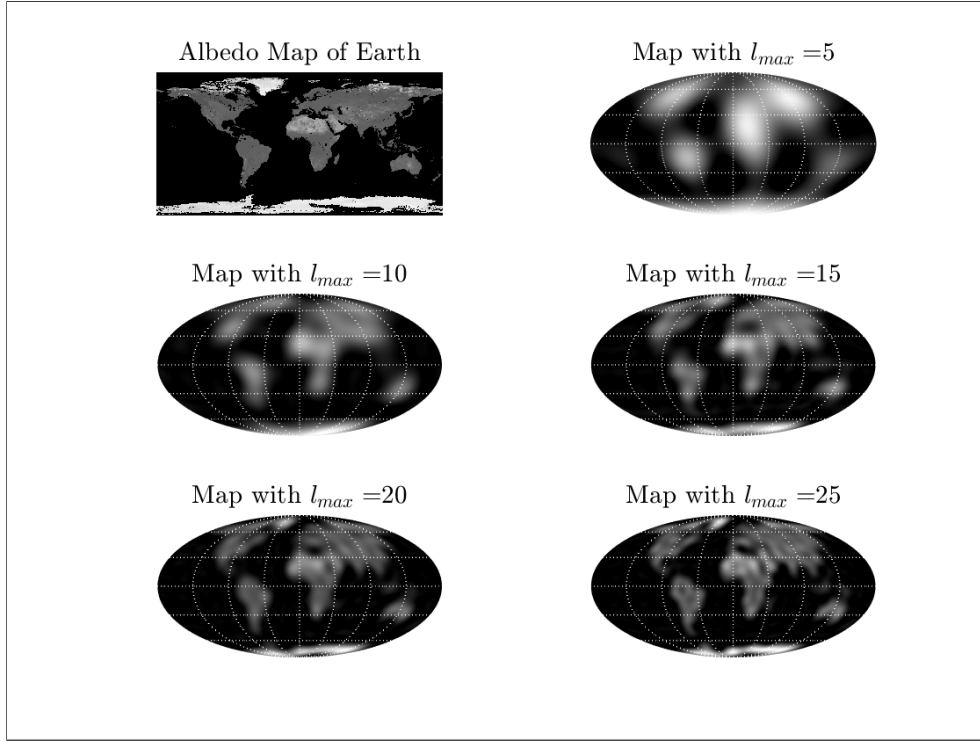
Figure 2.1: *The albedo map of earth from figure 1.4, decomposed in the spherical harmonics Y_l^m, where $0 \le l \le L$ with different values of L.*

We now can link f_k^n to M_l^m, but we need a plan. This plan will be used four times in this report (twice in this chapter, twice in the next), and is as follows:

1. Calculate the contribution of one spherical harmonic to the light-curve, as a function of the spin-, and orbit- angles. This contribution is given by equation 1.2:

$$f_l^m(\phi, \Phi) = \frac{1}{\pi R^2} \iint_{\mathbb{D}} (-\hat{\mathbf{r}} \cdot \hat{\mathbf{s}})(\hat{\mathbf{s}} \cdot \hat{\mathbf{o}}) Y_l^m(\mathbf{s}) d^2 S \tag{2.5}$$

2. Project this contribution to the orthonormal basis of complex exponentials in order to calculate the contribution of a single spherical harmonic to the Fourier coefficients. This can be done by combining equation 2.2 and equation 2.5: $f_{k,l}^{n,m}$.

3. Use the linearity from equations 1.2 on page 8 and 2.3. These give that the coefficient of the total light-curve is the sum of the coefficients from the light-curves due to one spherical harmonic:

$$f_k^n = \sum_{l,m} f_{k,l}^{n,m} M_l^m$$

In the next two sections, we shall see that we can calculate the coefficients of the linear transformation that links them. The edge-on observation ($\theta_o = \pi/2$) is considered first, followed by the face-on observation ($\theta_o = 0$).

2.2 Calculating the Fourier coefficients for edge-on observations

Now we use what we know about the situation with which we are dealing: an *edge-on* observation of an exoplanet *zero axial tilt*. We use the same vectors as in equation 1.1 on page 5, and fill in the appropriate $\hat{\mathbf{o}}$:

$$\hat{\mathbf{o}} = (1, 0, 0)^T = \hat{\mathbf{x}}$$
$$\hat{\mathbf{r}} = (R \cos \phi, R \sin \phi, 0)^T$$
$$\hat{\mathbf{s}} = (\sqrt{1 - z^2} \cos \phi_p, \sqrt{1 - z^2} \sin \phi_p, z)^T$$

which we obtain by substitution of the appropriate values in 1.1. This gives the following expressions for the inner products:

$$\hat{\mathbf{s}} \cdot \hat{\mathbf{x}} = \sqrt{1 - z^2} \cos(\phi_p)$$
$$\hat{\mathbf{s}} \cdot \hat{\mathbf{r}} = \sqrt{1 - z^2} \cos(\phi_p - \phi)$$
$$d^2 S = s^2 dz d\phi_p$$
$$\mathbb{D} = \{(\phi_p, z) : \sqrt{1 - z^2} \cos(\phi_p) > 0 \wedge \sqrt{1 - z^2} \cos(\phi_p - \phi) < 0\}$$
$$= \{(\phi_p, z) : \cos(\phi_p) > 0 \wedge \cos(\phi_p - \phi - \pi) > 0\}$$

where s is the radius of the exoplanet. The expression for $\mathbb{D}$ is tricky, but we will resolve this issue by making use of the $\cos^+$ function [1].

Calculating the light-curve of one spherical harmonic

We substitute these three expressions in equation 2.5, and obtain:

$$f_l^m(\phi, \Phi) = \frac{1}{\pi R^2} \iint_{\mathbb{D}} (-\hat{\mathbf{r}} \cdot \hat{\mathbf{s}})(\hat{\mathbf{s}} \cdot \hat{\mathbf{o}}) Y_l^m(\mathbf{s}) d^2 S$$
$$= \frac{s^2}{\pi R^2} \int_{-1}^{1} \int_0^{2\pi} (1 - z^2) \cos^+(\phi_p) \cos^+(\phi_p - \Phi) Y_l^m(\arccos(z), \phi_p - \Phi) dz d\phi_p$$
$$= \frac{s^2}{\pi R^2} \int_{-1}^{1} (1 - z^2) \mathcal{N}_l^m P_l^m(z) dz \int_0^{2\pi} \cos^+(\phi_p) \cos^+(\phi_p - \phi - \pi) e^{im(\phi_p - \Phi)} d\phi_p$$

Where the $-\Phi$ in the spherical harmonic accounts for the spin rotation, $\mathcal{N}_l^m$ is a normalization constant, and P_l^m is an associated Legendre polynomial (from appendix A). is We have split the surface integral into two line integrals, of which the first is a constant, and the second depends on the planets configuration. The following abbreviations shall be used :

$$y_l^m \equiv \mathcal{N}_l^m \int_{-1}^{1} (1 - z^2) P_l^m(z) dz \tag{2.6}$$

$$\mathcal{G}_l^m \equiv \int_0^{2\pi} \int_0^{2\pi} \cos^+(\phi) \cos^+(\phi - \theta - \pi) e^{-i(m\phi + l\theta)} d\phi d\theta \tag{2.7}$$

to keep the relations readable.

Calculating the Fourier coefficients of the light-curve of one spherical harmonic

Substituting this expression for the light-curve of a single spherical harmonic into equation 2.2 results in the following (rather complicated) calculation, in which we now integrate over three angles: the spin and orbit angles Φ and ϕ, and the longitude ϕ_p (step 2).

---

[1]Remember that at the end of chapter 1, we introduced the positive part of a function as $f^+(x) = \max\{f(x), o\}$

$$(2\pi)^2 f_{k,l}^{n,m} = \int_0^{2\pi} \int_0^{2\pi} \left[\frac{s^2}{\pi R^2} y_l^m \int_0^{2\pi} \cos^+(\phi_p) \cos^+(\phi_p - \phi - \pi) e^{im(\phi_p - \Phi)} d\phi_p \right] e^{-i(k\phi + n\Phi)} d\phi d\Phi$$

$$= \frac{s^2}{\pi R^2} y_l^m 2\pi \delta_{m,-n} \int_0^{2\pi} \int_0^{2\pi} \cos^+(\phi_p) \cos^+(\phi_p - \phi - \pi) e^{i(m\phi_p - k\phi)} d\phi d\phi_p$$

$$= \frac{2s^2}{R^2} y_l^m \delta_{m,-n} \int_0^{2\pi} \int_0^{2\pi} \cos^+(\phi_p) \cos^+(\phi_p - \phi - \pi) e^{-i(n\phi_p + k\phi)} d\phi d\phi_p$$

$$\equiv \frac{2s^2}{R^2} \mathcal{G}_k^n y_l^m \delta_{m,-n}$$

Calculating the Fourier coefficients for an arbitrary map

We now know the Fourier coefficients of the light-curve for a single spherical harmonic. The Fourier coefficients for an arbitrary map can be obtained by using the linearity of the transformation (step 3):

$$f_k^m = \sum_{l,m} M_l^m f_{k,l}^{n,m} = \frac{s^2}{R^2} \frac{\mathcal{G}_k^n}{2\pi^2} \sum_{l=|n|}^{\infty} M_l^{-n} y_l^{-n}$$

As can be seen in the equation, the Fourier coefficients f_k^n only depend on map coefficients M_l^m with $m = -n$. This confirms our suspicion that we stated in section 2.1. One can compute the coefficients y_l^n and $\mathcal{G}_k^n$ numerically, but we shall calculate them analytically in the next sections. This will also give us more insight their behavior.

2.2.1 CALCULATING THE y COEFFICIENTS

The calculation of y_l^m cannot be done straigtforeward, due to the definition of the associated Legendre polynomials:

$$P_l^m(x) = \frac{(-1)^m}{2^l l!} (1 - x^2)^{m/2} \frac{d^{l+m}}{dx^{l+m}} (x^2 - 1)^l \tag{2.8}$$

which makes integration particularly difficult.

First consider the cases in which $l + m$ is an odd number. This means that the Legendre polynomials has degree $l - m$, which is odd. This means P_l^m is an odd function of x. Combined with the fact that the function $(1 - x^2)$ is even, we get an integrand that is odd and thus that $y_l^m = 0$.

Secondly: one can also verify that, $y_l^{-m} = (-1)^m y_l^m$, using properties of the Associated Legendre Polynomials. So, the only values of l and m that are left to consider are $l + m$ even, and $m \geq 0$.

Assume from now on that $l + m$ is even, and that $m \geq 0$ we can use Newton's Binomial Theorem to get rid of the differentiation and expand the Legendre polynomials as:

$$P_l^m(x) = \frac{(-1)^m}{2^l l!} (1 - x^2)^{m/2} \frac{d^{l+m}}{dx^{l+m}} \left[\sum_{k=0}^{l} \binom{l}{k} (x^2)^k (-1)^{l-k} \right] \qquad \text{Using Newtons Binomial Theorem}$$

$$= \frac{(-1)^{l+m}}{2^l l!} (1 - x^2)^{m/2} \sum_{k=0}^{l} \binom{l}{k} (-1)^k \frac{d^{l+m}}{dx^{l+m}} x^{2k}$$

$$= \frac{1}{2^l l!} (1 - x^2)^{m/2} \sum_{k=(l+m)/2}^{l} \binom{l}{k} (-1)^k \frac{(2k)!}{(2k - l - m)!} x^{2k - l - m} \qquad \text{Since } l + m \text{ is even}$$

This expression is already much easier to work with. Filling this in into the definition of y_l^m gives:

$$y_l^m = \mathcal{N}_l^m \sum_{k=\frac{l+m}{2}}^{l} \frac{1}{2^l l!} \frac{(2k)!}{(2k - l - m)!} \binom{l}{k} (-1)^k \int_{-1}^{1} (1 - x^2)^{1 + \frac{m}{2}} x^{2k - l - m} dx$$

The integral has a known solution:

$$\int_{-1}^{1} (1-x^2)^a x^b dx = \frac{(1+(-1)^b)\Gamma(1+a)\Gamma(\frac{1+b}{2})}{2\Gamma(\frac{3+b}{2}+a)} \qquad \text{if } a > -1 \text{ and } b > -1$$

If we want to use this, we need that $2k - l - m > -1$, which is always the case because of the range of our summation. Furthermore, we need that $m > -4$. These conditions are both satisfied with $l \leq m \leq 0$

$$y_l^m = k_l^m \sum_{k=\frac{l+m}{2}}^{l} \frac{1}{2^l l!} \frac{(2k)!}{(2k-l-m)!} \binom{l}{k} (-1)^k \frac{(1+(-1)^{2k-l-m})\Gamma(2+\frac{m}{2})\Gamma(1/2+k-\frac{l+m}{2})}{2\Gamma\left(\frac{1}{2}(5+2k-l)\right)}$$

$$= k_l^m \sum_{k=\frac{l+m}{2}}^{l} \frac{1}{2^l l!} \frac{(2k)!}{(2k-l-m)!} \binom{l}{k} (-1)^k \frac{\Gamma(2+\frac{m}{2})\Gamma(\frac{1}{2}+k-\frac{l+m}{2})}{\Gamma\left(\frac{1}{2}(5+2k-l)\right)}$$

For some values of m, this expression is almost always equal to 0:

$$y_l^m = \begin{cases} \sqrt{\frac{8}{15\pi}}\delta_{l,2}, & \text{if } |m| = 2 \\ \frac{2}{3\sqrt{\pi}}\delta_{l,0} - \frac{2}{3\sqrt{5\pi}}\delta_{l,2}, & \text{if } m = 0 \end{cases} \tag{2.9}$$

2.2.2 Calculating the $\mathcal{G}$ coefficients

We shall obtain the $\mathcal{G}$ coefficients by representing the $\cos^+$ function as a Fourier series, this reduces the integral to a sum of standard integrals.

$$\cos^+(x) = \sum_{n\in\mathbb{Z}} c_n e^{inx} \qquad c_n = \begin{cases} \frac{1}{4} & n \in \{-1,1\} \\ \frac{i^n}{\pi(1-n^2)} & \text{n even} \\ 0 & \text{otherwise} \end{cases} \tag{2.10}$$

Now we substitute this in $\mathcal{G}$, and get:

$$\mathcal{G}_l^m = \int_0^{2\pi} \int_0^{2\pi} \cos^+(\phi_p) \cos^+(\phi_p - \theta - \pi) e^{-i(m\phi_p + l\theta)} d\theta d\phi_p$$

$$= \int_0^{2\pi} \int_0^{2\pi} \left[\sum_{n\in\mathbb{Z}} c_n e^{n\phi i}\right] \left[\sum_{k\in\mathbb{Z}} c_k e^{k(\phi-\theta-\pi)i}\right] e^{-i(m\phi+l\theta)} d\theta d\phi$$

$$= \sum_{n,k} (-1)^k c_k c_n \int_0^{2\pi} \int_0^{2\pi} e^{i(n-m+k)\phi} e^{-i(k+l)\theta} d\phi d\theta$$

$$= \sum_{n,k} (-1)^k c_k c_n 2\pi\delta_{k,-l} \int_0^{2\pi} e^{i(n-m+k)\phi} d\phi$$

$$= \sum_{n} (-1)^{-l} c_{-l} c_n (2\pi)^2 \delta_{n,l+m}$$

$$= (-1)^l c_l c_{l+m} (2\pi)^2$$

If we now put this result back into the formula of the light-curve Fourier coefficients, we get:

$$\boxed{f_k^n = \frac{2s^2}{R^2}(-1)^k c_k c_{k+n} \sum_{l=|n|}^{\infty} M_l^{-n} y_l^{-n}} \tag{2.11}$$

These are the Fourier-coefficients of an edge-on observation of a single planet, assuming Lambertian reflection.

With what we now know about the y_l^m coefficients, we can conclude that the range of this sum is (in most cases) infinite. Therefore if we were to write down this problem for some values of k and n, we

would need an infinite wide matrix. We shall thus have to find a suitable approximation in the form of a matrix, only then can we solve the map coefficients M_l^m for given Fourier coefficients of the light-curve. One possible approximation is given in the table below (table 2.1). The element in the row of f_k^n and column of M_l^m denotes $(-1)^k c_k c_{k+n} y_l^{-n}$ if $m = -n$ and 0 else. As we could have suspected, the matrix is sparse. This is because we only take one value of m for every l per Fourier coefficient. Last, it might seem strange that some spherical harmonics such as M_1^0 have no influence on the light-curve at all, they are in the null-space. This is because, in contrast to the albedo map, spherical harmonics can be both positive and negative. Thus they can cancel themselves out.

2.3 Calculating the Fourier coefficients for face-on observations

We now consider the face-on observation. For an Earth twin with no axial tilt, the observer that views the planet face-on would see either figure 2.2a or 2.2b.

In this section, repetition will occur[2]. We use the exact same scheme as from section 2.2; starting from equation 2.5. We keep the cylindrical coordinates for $\hat{\mathbf{r}}$ and $\hat{\mathbf{s}}$, but rotate $\hat{\mathbf{o}}$ such that it corresponds to a face-on observation:

$$\hat{\mathbf{o}} = (0, 0, 1)^T = \hat{\mathbf{z}}$$

This gives the following:

$$\hat{\mathbf{s}} \cdot \hat{\mathbf{o}} = \hat{\mathbf{s}} \cdot \hat{\mathbf{z}} = z$$

$$\hat{\mathbf{s}} \cdot \hat{\mathbf{r}} = \sqrt{1 - z^2} \cos(\phi_p - \omega t)$$

$$d^2 S = s^2 dz d\phi_p$$

$$\mathfrak{D} = \{(\phi_p, z) : z > 0 \wedge \sqrt{1 - z^2} \cos(\phi_p - \omega t) < 0\}$$

$$= \{(\phi_p, z) : z > 0 \wedge \cos(\phi_p - \omega t - \pi) > 0\}$$

By replacing the cos with $\cos^+$, as we have done before, we can integrate over $0 < z < 1$ and $0 < \phi_p < 2\pi$.

Calculating the light-curve for one spherical harmonic

If these expressions are substituted in equations 1.2, one obtains the signal from one spherical harmonic Y_l^m:

$$f_l^m(\phi, \Phi) = \frac{1}{\pi R^2} \iint_{\mathfrak{D}} (-\hat{\mathbf{r}} \cdot \hat{\mathbf{s}})(\hat{\mathbf{s}} \cdot \hat{\mathbf{o}}) Y_l^m(\mathbf{s}) d^2 S$$

$$= \frac{1}{\pi R^2} \int_0^1 \int_0^{2\pi} \sqrt{1 - z^2} \cos^+(\phi_p - \omega t - \pi) z \mathcal{N}_l^m P_l^m(z) e^{im(\phi_p - \Omega t)} s^2 d\phi_p dz$$

$$= \frac{s^2}{\pi R^2} \mathcal{N}_l^m \int_0^1 z\sqrt{1 - z^2} P_l^m(z) dz \int_0^{2\pi} \cos^+(\phi_p - \phi - \pi) e^{im(\phi_p - \Phi)} d\phi_p$$

Let's introduce the coefficients y and $\mathcal{G}$ for the face-on observation:

$$y_l^m \equiv \mathcal{N}_l^m \int_0^1 z\sqrt{1 - z^2} P_l^m(z) dz \tag{2.12}$$

$$\mathcal{G}_k^n \equiv \int_0^{2\pi} \int_0^{2\pi} \cos^+(\theta - \phi - \pi) e^{-i(n\theta + k\phi)} d\phi d\theta \tag{2.13}$$

Note that the same name has been used as in the edge-on observations, but they are not the same.

Calculating the Fourier coefficients of the light-curve of one spherical harmonic

Next, we can calculate the f_k^n contribution due to Y_l^m:

$$(2\pi)^2 f_{k,l}^{n,m} = \int_0^{2\pi} \int_0^{2\pi} f_l^m(\phi, \Phi) e^{-i(k\phi + n\Phi)} d\phi d\Phi$$

$$= \int_0^{2\pi} \int_0^{2\pi} \left[\frac{s^2}{\pi R^2} y_l^m \int_0^{2\pi} \cos^+(\phi_p - \phi - \pi) e^{im(\phi_p - \Phi)} d\phi_p \right] e^{-i(k\phi + n\Phi)} d\phi d\Phi$$

$$= \frac{s^2}{\pi R^2} y_l^m \int_0^{2\pi} e^{-i(m+n)\Phi} d\Phi \int_0^{2\pi} \int_0^{2\pi} \cos^+(\phi_p - \phi - \pi) e^{i(m\phi_p - k\phi)} d\phi d\phi_p$$

---

[2]I can't help it either
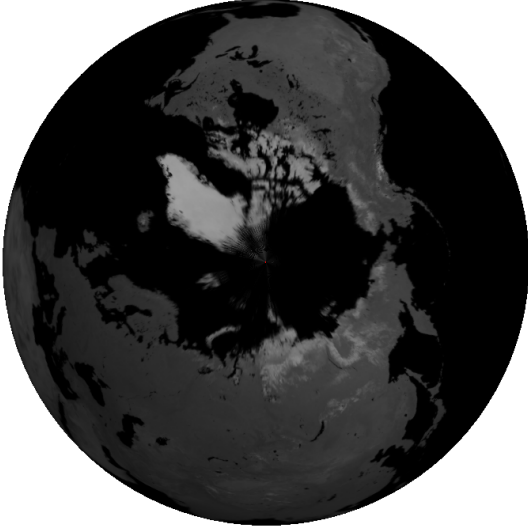
(a) *View of the north pole.* **(b)** *View of the south pole.*
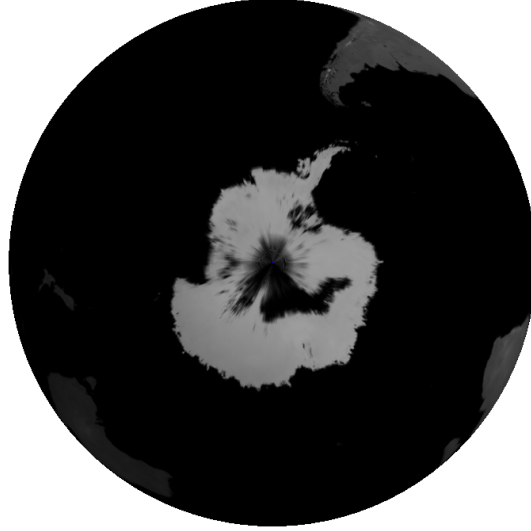
Figure 2.2: *View of the north-, and south-pole of the Earth, which are the observable parts of the planet in an face-on observation.*

$$
\begin{aligned}
(2/pi)^2 f_{k,l}^{n,m} &= \frac{s^2}{\pi R^2} y_l^m 2\pi \delta_{-n,m} \int_0^{2\pi} \int_0^{2\pi} \cos^+(\phi_p - \phi - \pi) e^{i(m\phi_p - k\phi)} d\phi d\phi_p \\
&= \frac{2s^2}{\pi R^2} y_l^m \delta_{-n,m} \int_0^{2\pi} \int_0^{2\pi} \cos^+(\phi_p - \phi - \pi) e^{-i(n\phi_p + k\phi)} d\phi d\phi_p \\
&= \frac{2s^2}{R^2} y_l^m \mathcal{G}_k^n \delta_{m,-n}
\end{aligned}
$$

Note that this is similar to the equation from last section, but the definitions of y and $\mathcal{G}$ are different.

Calculating the Fourier coefficients of the light-curve of an arbitrary map

If we plug in a arbitrary map, we can use the linearity of the transformation (step 3):

$$
(2\pi)^2 f_k^n = \sum_{l=0}^{\infty} \sum_{m=-l}^{l} M_l^m \left[\frac{2s^2}{R^2} y_l^{-n} \mathcal{G}_k^n \delta_{m,-n} \right]
$$

$$
f_k^n = \frac{s^2}{2\pi^2 R^2} \mathcal{G}_k^n \sum_{l=|n|}^{\infty} y_l^{-n} M_l^{-n}
$$

We shall see that working out $\mathcal{G}$ gives us the Fourier coefficients of the (reflective) light-curve for face-on observation :

$$
\boxed{ f_k^n = \frac{2s^2}{R^2} (-1)^n c_n \delta_{n,-k} \sum_{l=|n|}^{\infty} y_l^{-n} M_l^{-n} } \tag{2.14}
$$

where c_n are the Fourier coefficients of $\cos^+$, which can be found in equation 2.10. Notice that every spherical harmonic contributes only to one component of the light-curve. The Kronecker-δ in the expression reflects the fact that the signal is independent of the position relative to the star. However, the orbital velocity adds with the spin velocity (or rather, we subtract one from another), such that the peaks do not appear at $k = 0$ (corresponding to frequency $\nu = n\Omega$), but at $k = -n$ (corresponding to $\nu = n(\Omega - \omega)$).

2.3.1 CALCULATING y FOR FACE-ON OBSERVATIONS

We calculate y_l^m and $\mathcal{G}_k^n$, which is very similar to the calculation of y_l^m and $\mathcal{G}_k^n$ from chapter 2. Let's start with y_l^m, for which we once again use Newton's Binomial theorem to expand the Associated Legendre polynomials:

$$
\begin{aligned}
y_l^m &= \mathcal{N}_l^m \int_0^1 z\sqrt{1-z^2}P_l^m(z)dz \\
&= \mathcal{N}_l^m \int_0^1 z\sqrt{1-z^2}\left[\frac{(-1)^{l+m}}{2^l l!}(1-z^2)^{m/2}\sum_{k=0}^l \binom{l}{k}(-1)^k\frac{d^{l+m}}{dz^{l+m}}z^{2k}\right]dz \\
&= \mathcal{N}_l^m\frac{(-1)^{l+m}}{2^l l!}\sum_{k=0}^l\left[\binom{l}{k}(-1)^k\int_0^1 z(1-z^2)^{(m+1)/2}\frac{d^{l+m}}{dz^{l+m}}z^{2k}dz\right] \\
&= \mathcal{N}_l^m\frac{(-1)^{l+m}}{2^l l!}\sum_{k=\lceil\frac{l+m}{2}\rceil}^l\left[\binom{l}{k}(-1)^k\int_0^1 z(1-z^2)^{(m+1)/2}\frac{(2k)!}{(2k-l-m)!}z^{2k-l-m}dz\right] \\
&= \mathcal{N}_l^m\frac{(-1)^{l+m}}{2^l l!}\sum_{k=\lceil\frac{l+m}{2}\rceil}^l\left[\binom{l}{k}(-1)^k\frac{(2k)!}{(2k-l-m)!}\int_0^1 z^{2k-l-m+1}(1-z^2)^{(m+1)/2}dz\right]
\end{aligned}
$$

Now we use the known integral:

$$
\int_0^1 z^a(1-z^2)^b dz = \frac{\Gamma\left(\frac{a+1}{2}\right)\Gamma(b+1)}{2\Gamma\left(\frac{a}{2}+b+\frac{3}{2}\right)} \qquad \text{if } a>-1 \text{ and } b>-1 \tag{2.15}
$$

and obtain:

$$
y_l^m = \mathcal{N}_l^m\frac{(-1)^{l+m}}{2^l l!}\sum_{k=\lceil\frac{l+m}{2}\rceil}^l\binom{l}{k}(-1)^k\frac{(2k)!}{(2k-l-m)!}\frac{\Gamma\left(\frac{m+3}{2}\right)\Gamma\left(k-\frac{l}{2}-\frac{m}{2}+1\right)}{2\Gamma\left(k-\frac{l}{2}+\frac{5}{2}\right)} \tag{2.16}
$$

But this expression only holds for $m \geq 0$, as we can learn from equation 2.15. But as we know: $P_l^{-m}(x)=(-1)^m\frac{(l-m)!}{(l+m)!}P_l^m(x)$, giving $y_l^{-m}=(-1)^m y_l^m$. So now we can use the formula for any value of m.

2.3.2 CALCULATING $\mathcal{G}$ FOR FACE-ON OBSERVATIONS

For the calculation of the $\mathcal{G}$ coefficients, we use the Fourier series of $\cos^+$ from equation 2.10 on page 19. This gives us the expression

$$
\begin{aligned}
\mathcal{G}_k^n &= \int_0^{2\pi}\int_0^{2\pi}\cos^+(\theta-\phi-\pi)e^{-i(n\theta+k\phi)}d\phi d\theta \\
&= \int_0^{2\pi}\int_0^{2\pi}\left[\sum_{l=-\infty}^\infty c_l e^{il(\theta-\phi-\pi)}\right]e^{-i(n\theta+k\phi)}d\phi d\theta \\
&= \sum_{l=-\infty}^\infty c_l e^{il\pi}\int_0^{2\pi}e^{i(l-n)\theta}d\theta\int_0^{2\pi}e^{i(-l-k)\phi}d\phi \\
&= \sum_{l=-\infty}^\infty c_l(-1)^l(2\pi\delta_{l,n})(2\pi\delta_{l,-k}) \\
\mathcal{G}_k^n &= (2\pi)^2(-1)^n c_n\delta_{n,-k} \tag{2.17}
\end{aligned}
$$

And after substituting this back into the expression of f_k^n, one obtains 2.14.

Table 2.1: *A table of the coefficients of the transformation for an edge-on and a face on observation of a non-tilted planet: each entry is given by a element of equation 2.11 or 2.14.*

Edge-on

	M_0^0	M_1^{-1}	M_1^0	M_1^1	M_2^{-2}	M_2^{-1}	M_2^0	M_2^1	M_2^2	M_3^{-3}	M_3^{-2}	M_3^{-1}	M_3^0	M_3^1	M_3^2	M_3^3
f_{-2}^{-2}	0	0	0	0	0	0	0	0	$-\frac{4\sqrt{\frac{2}{15}}}{45\pi^{5/2}}$	0	0	0	0	0	0	0
f_{-1}^{-2}	0	0	0	0	0	0	0	0	0	0	0	0	0	0	0	0
f_0^{-2}	0	0	0	0	0	0	0	0	$\frac{4\sqrt{\frac{2}{15}}}{3\pi^{5/2}}$	0	0	0	0	0	0	0
f_1^{-2}	0	0	0	0	0	0	0	0	$-\frac{1}{2\sqrt{30\pi}}$	0	0	0	0	0	0	0
f_2^{-2}	0	0	0	0	0	0	0	0	$\frac{4\sqrt{\frac{2}{15}}}{3\pi^{5/2}}$	0	0	0	0	0	0	0
f_{-2}^{-1}	0	0	0	0	0	0	0	0	0	0	0	0	0	0	0	0
f_{-1}^{-1}	0	0	0	$\frac{1}{32}\sqrt{\frac{3}{2\pi}}$	0	0	0	0	0	0	0	0	0	$-\frac{1}{256}\sqrt{\frac{7}{3\pi}}$	0	0
f_0^{-1}	0	0	0	$\frac{-3}{32}\sqrt{\frac{3}{2\pi}}$	0	0	0	0	0	0	0	0	0	$\frac{\sqrt{\frac{21}{\pi}}}{256}$	0	0
f_1^{-1}	0	0	0	$\frac{3}{32}\sqrt{\frac{3}{2\pi}}$	0	0	0	0	0	0	0	0	0	$-\frac{\sqrt{\frac{21}{\pi}}}{256}$	0	0
f_2^{-1}	0	0	0	$-\frac{1}{32}\sqrt{\frac{3}{2\pi}}$	0	0	0	0	0	0	0	0	0	$\frac{1}{256}\sqrt{\frac{7}{3\pi}}$	0	0
f_{-2}^0	$\frac{4}{27\pi^{5/2}}$	0	0	0	0	0	$-\frac{4}{27\sqrt{5}\pi^{5/2}}$	0	0	0	0	0	0	0	0	0
f_{-1}^0	$-\frac{1}{12\sqrt{\pi}}$	0	0	0	0	0	$\frac{1}{12\sqrt{5\pi}}$	0	0	0	0	0	0	0	0	0
f_0^0	$\frac{4}{3\pi^{5/2}}$	0	0	0	0	0	$-\frac{4}{3\sqrt{5}\pi^{5/2}}$	0	0	0	0	0	0	0	0	0
f_1^0	$-\frac{1}{12\sqrt{\pi}}$	0	0	0	0	0	$\frac{1}{12\sqrt{5\pi}}$	0	0	0	0	0	0	0	0	0
f_2^0	$\frac{4}{27\pi^{5/2}}$	0	0	0	0	0	$-\frac{4}{27\sqrt{5}\pi^{5/2}}$	0	0	0	0	0	0	0	0	0
f_{-2}^1	0	$\frac{1}{32}\sqrt{\frac{3}{2\pi}}$	0	0	0	0	0	0	0	0	0	$-\frac{1}{256}\sqrt{\frac{7}{3\pi}}$	0	0	0	0
f_{-1}^1	0	$\frac{-3}{32}\sqrt{\frac{3}{2\pi}}$	0	0	0	0	0	0	0	0	0	$\frac{\sqrt{\frac{21}{\pi}}}{256}$	0	0	0	0
f_0^1	0	$\frac{3}{32}\sqrt{\frac{3}{2\pi}}$	0	0	0	0	0	0	0	0	0	$-\frac{\sqrt{\frac{21}{\pi}}}{256}$	0	0	0	0
f_1^1	0	$-\frac{1}{32}\sqrt{\frac{3}{2\pi}}$	0	0	0	0	0	0	0	0	0	$\frac{1}{256}\sqrt{\frac{7}{3\pi}}$	0	0	0	0
f_2^1	0	0	0	0	0	0	0	0	0	0	0	0	0	0	0	0
f_{-2}^2	0	0	0	0	$\frac{4\sqrt{\frac{2}{15}}}{3\pi^{5/2}}$	0	0	0	0	0	0	0	0	0	0	0
f_{-1}^2	0	0	0	0	$-\frac{1}{2\sqrt{30\pi}}$	0	0	0	0	0	0	0	0	0	0	0
f_0^2	0	0	0	0	$\frac{4\sqrt{\frac{2}{15}}}{3\pi^{5/2}}$	0	0	0	0	0	0	0	0	0	0	0
f_1^2	0	0	0	0	0	0	0	0	0	0	0	0	0	0	0	0
f_2^2	0	0	0	0	$-\frac{4\sqrt{\frac{2}{15}}}{45\pi^{5/2}}$	0	0	0	0	0	0	0	0	0	0	0

Face-on

	M_0^0	M_1^{-1}	M_1^0	M_1^1	M_2^{-2}	M_2^{-1}	M_2^0	M_2^1	M_2^2	M_3^{-3}	M_3^{-2}	M_3^{-1}	M_3^0	M_3^1	M_3^2	M_3^3
f_{-2}^{-2}	0	0	0	0	0	0	0	0	0	0	0	0	0	0	0	0
f_{-1}^{-2}	0	0	0	0	0	0	0	0	0	0	0	0	0	0	0	0
f_0^{-2}	0	0	0	0	0	0	0	0	0	0	0	0	0	0	0	0
f_1^{-2}	0	0	0	0	0	0	0	0	0	0	0	0	0	0	0	0
f_2^{-2}	0	0	0	0	0	0	0	0	$\frac{1}{2\sqrt{30}\pi^{3/2}}$	0	0	0	0	0	$\frac{1}{64}\sqrt{\frac{35}{6\pi}}$	0
f_{-2}^{-1}	0	0	0	0	0	0	0	0	0	0	0	0	0	0	0	0
f_{-1}^{-1}	0	0	0	0	0	0	0	0	0	0	0	0	0	0	0	0
f_0^{-1}	0	0	0	0	0	0	0	0	0	0	0	0	0	0	0	0
f_1^{-1}	0	0	0	$\frac{1}{16}\sqrt{\frac{3}{2\pi}}$	0	0	0	$\frac{1}{2\sqrt{30\pi}}$	0	0	0	0	0	$\frac{1}{32}\sqrt{\frac{7}{3\pi}}$	0	0
f_2^{-1}	0	0	0	0	0	0	0	0	0	0	0	0	0	0	0	0
f_{-2}^0	0	0	0	0	0	0	0	0	0	0	0	0	0	0	0	0
f_{-1}^0	0	0	0	0	0	0	0	0	0	0	0	0	0	0	0	0
f_0^0	$\frac{1}{3\pi^{3/2}}$	0	$\frac{\sqrt{\frac{3}{\pi}}}{16}$	0	0	0	$\frac{1}{6\sqrt{5}\pi^{3/2}}$	0	0	0	0	0	$-\frac{\sqrt{\frac{7}{\pi}}}{64}$	0	0	0
f_1^0	0	0	0	0	0	0	0	0	0	0	0	0	0	0	0	0
f_2^0	0	0	0	0	0	0	0	0	0	0	0	0	0	0	0	0
f_{-2}^1	0	0	0	0	0	0	0	0	0	0	0	0	0	0	0	0
f_{-1}^1	0	$-\frac{1}{16}\sqrt{\frac{3}{2\pi}}$	0	0	0	$-\frac{1}{2\sqrt{30\pi}}$	0	0	0	0	0	$-\frac{1}{32}\sqrt{\frac{7}{3\pi}}$	0	0	0	0
f_0^1	0	0	0	0	0	0	0	0	0	0	0	0	0	0	0	0
f_1^1	0	0	0	0	0	0	0	0	0	0	0	0	0	0	0	0
f_2^1	0	0	0	0	0	0	0	0	0	0	0	0	0	0	0	0
f_{-2}^2	0	0	0	0	$\frac{1}{2\sqrt{30}\pi^{3/2}}$	0	0	0	0	0	$\frac{1}{64}\sqrt{\frac{35}{6\pi}}$	0	0	0	0	0
f_{-1}^2	0	0	0	0	0	0	0	0	0	0	0	0	0	0	0	0
f_0^2	0	0	0	0	0	0	0	0	0	0	0	0	0	0	0	0
f_1^2	0	0	0	0	0	0	0	0	0	0	0	0	0	0	0	0
f_2^2	0	0	0	0	0	0	0	0	0	0	0	0	0	0	0	0

2.4   Linear transformations and the pseudoinverse

The linear transformation, hereafter transformation $\mathcal{A}$, that we derived in the last two sections for edge-, and face-on observations, gave us a full analytical description of the Fourier coefficients of the light curve in terms of the coefficients M_l^m. We can write this as $\mathbf{f} = \mathcal{A}(\mathbf{M})$, where $\mathbf{f} \in \mathbb{R}^\infty$ and $\mathbf{M} \in \mathbb{R}^\infty$. Since we are limited by the resolutions of the observations of the light-curve, only a number of coefficients from $\mathbf{f}$ can be obtained, and a finite number of map coefficients are considered. Now, the transformation can be written in matrix-vector form: $\mathbf{f} = A\mathbf{M}$. Now we suppose we know $\mathbf{f}$ and we want the map. We could try $\mathbf{M} = A^{-1}\mathbf{f}$, where A^{-1} is the inverse of A, but there is a problem with obtaining this inverse. These problems shall be explained, together with a solution.

First, A is in general not a square matrix, so an inverse is not defined. And even if the vectors are chosen such that they are of equal length, the transformation is not injective. For example: if we have an edge-on observation, the maps 0 and $Y_1^0(\theta_p, \phi_p)$ both result in $\mathbf{f} = 0$. Hence, the normal inverse of A does not exist.

However, there does exist an alternative to the normal inverse. Let $A : \mathbb{R}^m \to \mathbb{R}^n$. Any $\mathbf{M}$ can be decomposed as the sum of a vector in Row(A), called $\mathbf{M}_r$, and a vector in Null(A), called $\mathbf{M}_n$. Figure 2.3 shows how A transforms $\mathbf{M}$ to $\mathbf{f}_c$ [Strang, 2006]. $\mathbf{M}_n$ is transformed to $\mathbf{0}$, while $\mathbf{M}_r$ is mapped to the same light-curve as $\mathbf{M}$. As long as Null(A) $\neq \emptyset$, this means that given a vector $\mathbf{f}$, we cannot determine a unique $\mathbf{M}$ such that $\mathbf{f} = A\mathbf{M}$.
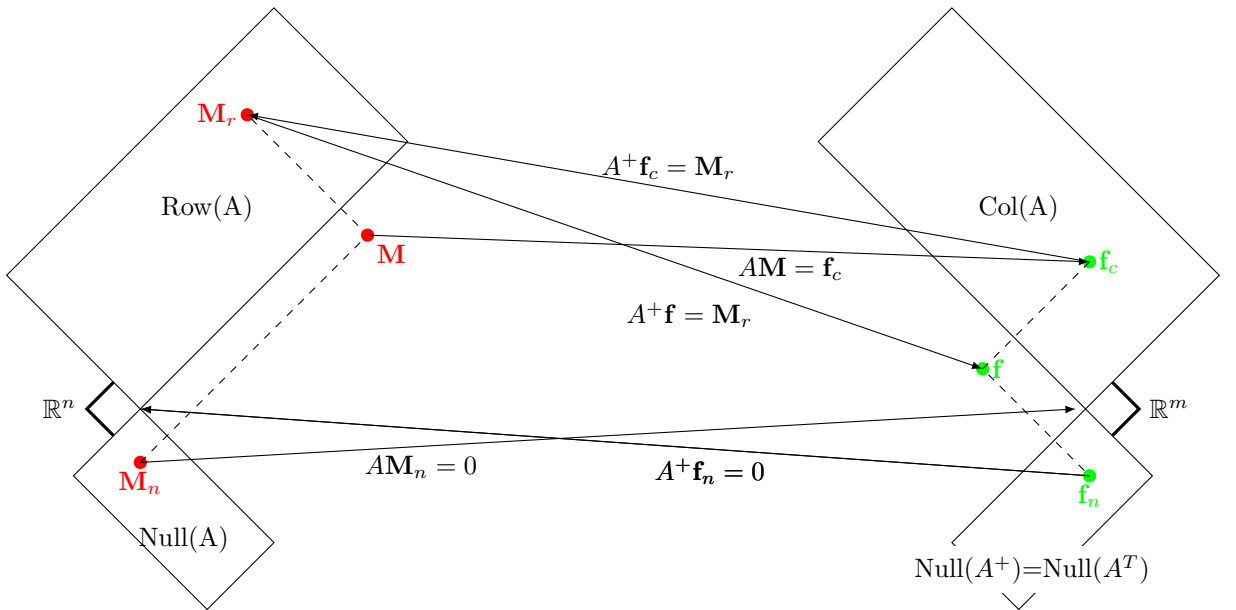
Figure 2.3: *The action of the matrix A, and it's pseudoinverse A^+. The Pseudoinverse map's all $\mathbf{f}$ in Col(A) back to $\mathbf{M}_r$, and all $\mathbf{f}$ in the left null space of A back to 0.*

However, the transformation from Row(A) to Col(A) is actually invertible. The inverting operator is called the **Moore-Penrose (pseudo)inverse** denoted with the symbol A^+ [Strang, 2006]. It is defined such that

$$A^+ \mathbf{f} = \begin{cases} \mathbf{M}_r & \text{if there exists an } \mathbf{M}_r \in \text{Row}(A) \text{ such that } A\mathbf{M}_r = \mathbf{f} \\ \mathbf{0} & \text{if } \mathbf{f} \in \text{Null}(A^T) \end{cases} \tag{2.18}$$

For a map $\mathbf{M}$ the pseudoinverse has the property that:

$$A^+ \mathbf{f} = A^+(A\mathbf{M}) = A^+ A(\mathbf{M}_r + \mathbf{M}_n) = \mathbf{M}_r + \mathbf{0} = \mathbf{M}_r$$

And since Row(A) is perpendicular to Null(A), $\mathbf{M}_r$ intuitively gives the best obtainable approximation for $\mathbf{M}$. In the next subsection, it is show how the pseudoinverse is obtained.

2.4.1   THE PSEUDOINVERSE AND SINGULAR VALUE DECOMPOSITION

The pseudoinverse of A is related to the singular value decomposition of A. This is the generalization of the spectral decomposition for non-square matrices. We can write any matrix A as a product of three matrices :

$$A = U\Sigma V^T = (\text{Orthogonal})(\text{Diagonal})(\text{Orthogonal})$$

The diagonal entries of the (diagonal) matrix Σ are the so-called singular values of A (denoted by σ), the square roots of the eigenvalues of $A^T A$. If A has the rank r, then there exist r singular values. The columns of U and V are respectively the eigenvectors of AA^T and $A^T A$. Similar to the spectral decomposition, r columns of U form a basis of the column space of A, and r columns of V form a basis of the row space of A. And furthermore, every column of V is mapped to a multiple of a column from U:

$$A\mathbf{v}_i = U\Sigma V\mathbf{v_i} = U\Sigma\mathbf{e}_i = \sigma_i\mathbf{u}_i \tag{2.19}$$

The singular value decomposition, together with the four spaces of A are shown in figure 2.4. The size of each matrix is indicated next to the arrows.
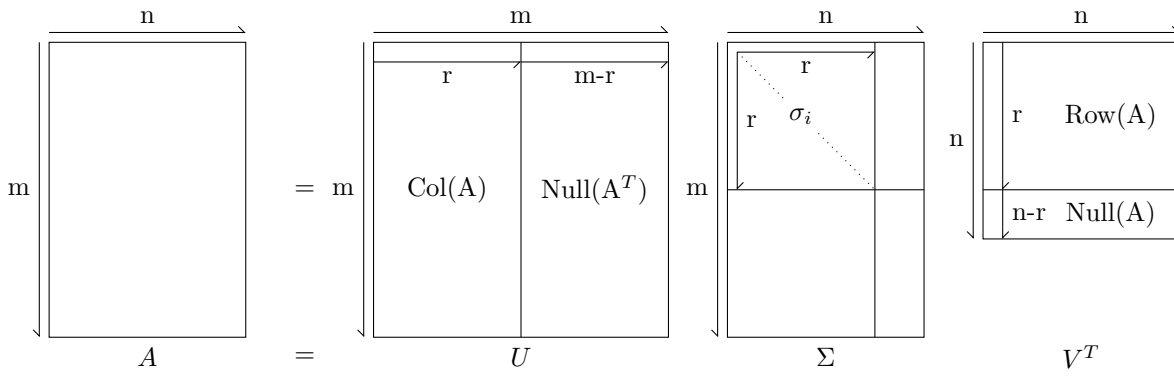
Figure 2.4: *Singular value decomposition of the m×n matrix A. The columns of U span the column space of A, while the columns of V span the row space of A.*

Now we can introduce the formula of the pseudoinverse of A:

$$A = \sum_{k=1}^{r} \sigma_k\mathbf{u}_k\mathbf{v}_k^T \qquad\qquad = U\Sigma V^T$$

$$A^+ = \sum_{k=1}^{r} \frac{1}{\sigma_k}\mathbf{v}_k\mathbf{u}_k^T \qquad\qquad = V\Sigma^+ U^T \tag{2.20}$$

We can check that this postulated equation satisfies the definition of A^+ from equation 2.18. For this we need the following property: let $\mathbf{u}_i$ be a column of U. Then:

$$A^+\mathbf{u}_i = \sum \sigma_k^{-1}\mathbf{v}_k\mathbf{u}_k^T\mathbf{u}_i = \mathbf{v}_i/\sigma_i \tag{2.21}$$

This is similar to equation 2.19.

Firstly, let $\mathbf{f}$ be a vector in the column space of A, given by $\mathbf{f} = A\mathbf{M} = A\mathbf{M}_r$. $\mathbf{M}_r$ can be written down as $\mathbf{M}_r = \sum_{k=1}^{r} m_k\mathbf{v}_k$. If we apply A^+ we get:

$$A^+\mathbf{f} = A^+ A\mathbf{M}_r = \sum_{k=1}^{r} m_k A^+ A\mathbf{v}_k = A\sum_{k=1}^{r} m_k A^+\mathbf{u}_k\sigma_k = \sum_{k=1}^{r} m_k\mathbf{v}_k = \mathbf{M}_r$$

Where we have used equations 2.19, 2.21 and 2.20.
Secondly, if $\mathbf{f} \in \text{Null}(A)$, then $\mathbf{f}$ is orthogonal to all of the columns of U. Thus $A^+\mathbf{f} = 0$. Thus, this expression for A^+ satisfies 2.18.

2.4.2   THE PSEUDOINVERSE AND PROJECTIONS

There is an alternative way of thinking about and obtaining the pseudoinverse. Suppose we have received a light-curve $\mathbf{f}$ and wonder: "What map would have produced the most-alike light curve?", which is uniquely determined up to addition of a vector from the null space. The most alike curve is of course defined via the euclidean norm, which means that the map we are searching for is the projection of $\mathbf{f}$ onto Col(A)[3]. This map that we are searching for, the estimate, shall be called $\hat{\mathbf{M}}$. The situation can be seen in figure 2.5.
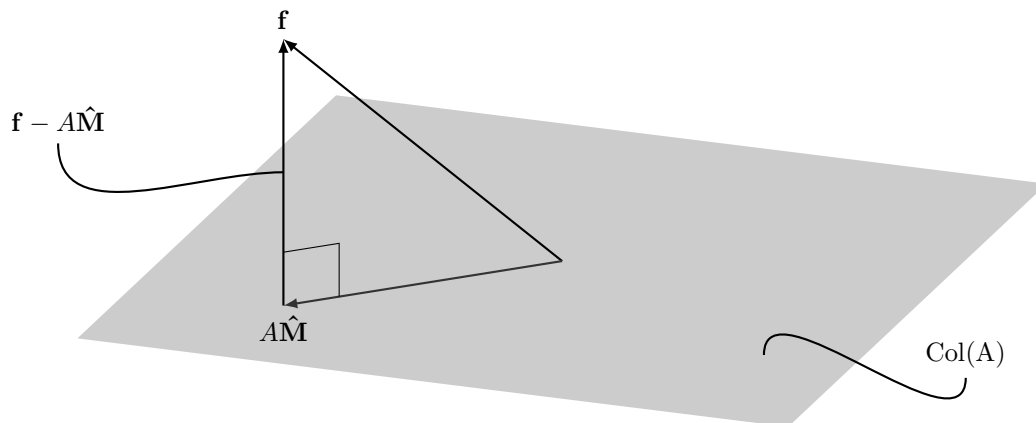
Figure 2.5: *Projection onto the linear subspace Col(A)*

We can get $\hat{\mathbf{M}}$ by observing that, since the distance from $\mathbf{f}$ and $A\hat{\mathbf{M}}$ is minimal, we must have that $A\hat{\mathbf{M}} \perp (\mathbf{f} - A\hat{\mathbf{M}})$, an thus it follows that $(A\hat{\mathbf{M}})^T(\mathbf{f} - A\hat{\mathbf{M}}) = (A\hat{\mathbf{M}}) \cdot (\mathbf{f} - A\hat{\mathbf{M}}) = 0$. Some algebra gives: $\hat{\mathbf{M}} = \left[(A^T A)^{-1} A^T \right] \mathbf{f}$. Now we can use the Singular Value Decomposition of A to obtain:

$$(A^T A)^{-1} A^T = \left(V \Sigma^T U^T U \Sigma V^T \right)^{-1} V \Sigma^T U^T = V \Sigma^+ U^T = A^+$$

Thus we can conclude that $\hat{\mathbf{M}} = A^+ \mathbf{f}$ is the linear projection of $\mathbf{f}$ onto Col(A).

---

[3]Since the light-curve is given by $\mathbf{f} = A\mathbf{M}$, we usually don't consider a $\mathbf{f}$ which is not an element of Col(A). However, due to the addition of noise and limitations in the resolution, a measured $\mathbf{f}$ might not be in Col(A).

2.5   Recovering Earths albedo map without axial tilt

In this section we present the results of application(s) of the methods that we have discussed in this chapter to Earths albedo map. The theory has been applied to other albedo maps as well. The results of this can be found in the appendix.

2.5.1   CORRECTNESS OF THE FORWARD TRANSFORM

Firstly, there is a need to verify the correctness of equations 2.11 and 2.14 to assure that no mistakes were made. We will do this by comparing these light-curves with the ones which we get by taking the Fourier transform of the signal which we obtain with equation 1.4.

The results can be seen in figures 2.6 and 2.7. The former compares the numerically computed light-curve (equation 1.4) with the analytically computed light-curve (equations 2.11 and 2.14, with $L = 20$). The upper two rows correspond the edge-on observation, and the lower two rows with the face-on observation. In the latter figure, the error $\|\mathbf{f} - A_l \mathbf{M}_l\|_2$ between the numerical and analytical light-curve as a function of l is displayed.

For practical reasons, the indices of the coefficients are limited to $|n| < N, |k| < K$, such that $f(\phi, \Phi) \approx \sum_{k=-K}^{K} \sum_{n=-N}^{N} f_k^n e^{i(k\phi + n\Phi)}$. We take $N = 3$ and $K = 5$, corresponding to the peaks which should be recoverable. Observe that for $L > 7$, the signal does not improve in figure 2.7.
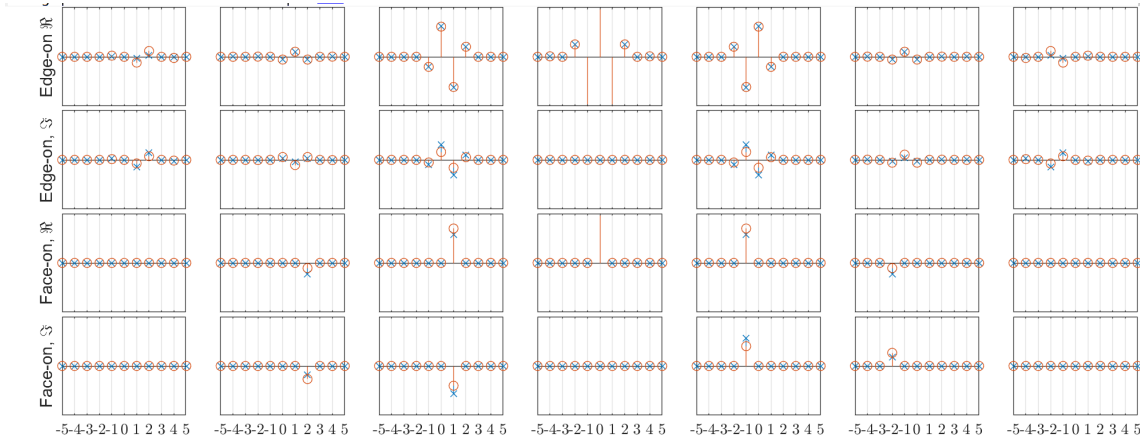
Figure 2.6: *A comparison between the numerically (red 'o') and analytically (blue '×') computed Fourier coefficients of the light-curve for a edge-on (upper two rows) and face-on (lower two rows) observation. Each column of plots corresponds to a value of n, the value of k is indicated.*
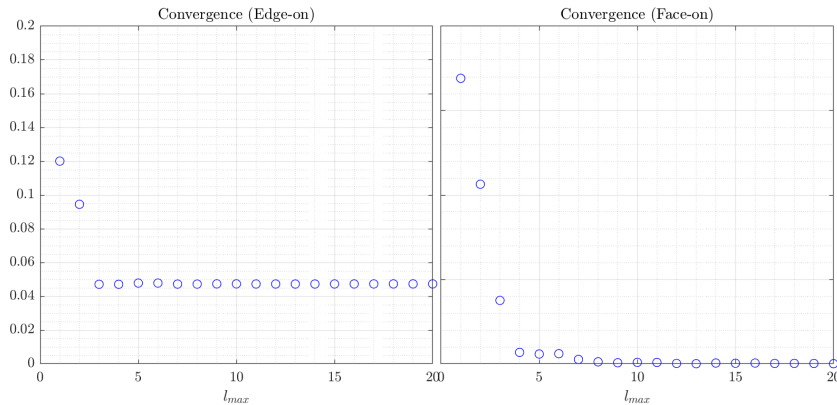
Figure 2.7: *The error $\|\mathbf{f} - A_l \mathbf{M}_l\|_2$ between the numerical ($\mathbf{f}$) and analytical ($A_l \mathbf{M}_l$) light-curve for $0 \leq l \leq 20$. The vertical axis is given in units of s^2/R^2.*

2.5.2   RECOVERING EARTH'S ALBEDO WITHOUT AXIAL TILT

Now that we have verified that the analytical expression for Fourier coefficients is correct, we turn our attention to actually solving our problem $\mathbf{f} = A\mathbf{M}$. For this we start with the coefficient vector $\mathbf{M}_{20}$, which contains more than enough information about our map, and compute:

$$\hat{\mathbf{M}}_{10} = A_{10}^{+}(A_{20}\mathbf{M}_{20})$$

Where $\hat{\mathbf{M}}_{10}$ is the reconstructed map. The coefficients of our original map with $l \leq 10$ map right back onto themselves (if they are in Col(A)) or 0 (if they are in Null(A^T)). One can see this by splitting A_{20} up in two sets of columns $A_{20} = [A_{10} \; A_{11-20}]$, which gives:

$$\hat{\mathbf{M}}_{10} = A_{10}^{+}(A_{10}\mathbf{M}_{10} + A_{11-20}\mathbf{M}_{11-20}) = \mathbf{M}_{10,c} + A_{10}^{+}A_{11-20}\mathbf{M}_{11-20}$$

Where $\mathbf{M}_{10,c}$ is the projection of $\mathbf{M}_{10}$ on Col(A_{10}). The results if this procedure can be seen in figure 2.10. The figure consists of four rows: in the upper row, the original map is displayed together with the best possible obtainable map $\mathbf{M}_{10}$, in the second row the result for the edge-on observation, and in the third and fourth row the results for the face-on observation. Just as in 1.4, negative albedo values are displayed as black.

Edge-on observation

The recovered map for the edge-on observation can be seen in the first column of the second row (we will get to the second column later). Although the reconstruction does neither resemble the original map nor the maximum obtainable map, the continents of America, Africa, and east-Asia are visible. The reason for this, is that since they lie close to the equator, they give the largest contribution to the light-curve.

Face-on observation

The procedure that we used to reconstruct the albedo map for edge-on observations can be repeated for face-on observations, the only difference being that it is performed twice (northern/southern hemisphere).

When observing the northern hemisphere, Canada and Russia are the most visible parts of Earth and can be found back in the recovered map. However, when observing the map of the southern hemisphere, there are no real visible areas. This is due to two reasons. First, the amount of land on the southern hemisphere is much smaller than on the northern hemisphere, and second, the largest land mass (Antartica) barely receives light from the star, making it practically invisible. What can be seen are the contributions from Australia and Southern-America.

2.5.3   INTERPRETATION OF THE RECONSTRUCTION WITH ZERO AXIAL TILT

Light-curve of the difference and uniqueness of the reconstruction

In order to evaluate the quality of our reconstructed map, we can look at the difference between the original map and the reconstruction. Because, if the original and the reconstructed map reproduce the same signal, the difference between these maps should produce no signal at all. For this, see figure 2.8. Here, one can see the real and imaginary part (in the upper and lower row respectively) of the light-curve as emitted by the original map and the reconstructed map (in red 'o' and blue '×'). Each column of the figure denotes a different value of n, k runs from -5 to 5 in each plot, **and have the same scale**. As can be seen, the difference map emits a light curve in the order of magnitude of about $10^{-7}s^2/R^2$, while the vertical limits of the plot are $\pm 0.004 s^2/R^2$

Latitudinal variations with an edge-on observation

One other thing to be noticed in figure 2.10: there is something odd about the variation of the reconstructed map along the latitudinal direction. Due to the configuration of our system (edge-on with no tilt), we cannot recover any information about how the map depends on θ_p. And yet, our reconstruction does show that the map is dependent on θ_p. However, if we divide the reconstruction by $\sin^2(\theta_p)$, we observe that the map is no longer dependent on θ_p (up to numerical errors). This 'modified' map is also plotted in figure 2.10 (second row and column).

The reason for the dependence on θ_p is that it is very hard for spherical harmonics to form a function that is invariant in θ_p. For all of these functions, except $M = 1$, need an infinite number of spherical harmonics to be constructed. Since we only use a finite number of spherical harmonics, we could not make such a map. However, we can compare the average value in the ϕ_p direction of both maps. This can be seen in figure 2.9. What the reason is for the second observation made, I do not know.

The dimension of Col(A) and the limits of reconstruction

In hindsight, one could ask whether it was justified to take arbitrary values of l_{max} for both the forward and the backward transformation. After all, given a vector $\mathbf{f}$, there are only so many map coefficients that can be retrieved and (depending on l_{max}) the problem is either underdetermined or overdetermined.

The number of coefficients that can be determined equals on the rank of the transformation matrix, and from equations 2.11 and 2.14, one obtains that

$$\mathrm{rank}(A) = 1 + 2 \min\{L, N\} \tag{2.22}$$

for edge-on observations, and

$$\mathrm{rank}(A) = \begin{cases} 1 & \text{if } \min\{L, N, K\} = 0 \\ 3 + 2 \left\lfloor \frac{\min\{L, N, K\}}{2} \right\rfloor & \text{else} \end{cases} \tag{2.23}$$

for face-on observations. In our case this means that we have only put 7 independent coefficients in our light-curve, and can only hope to recover as much as that.
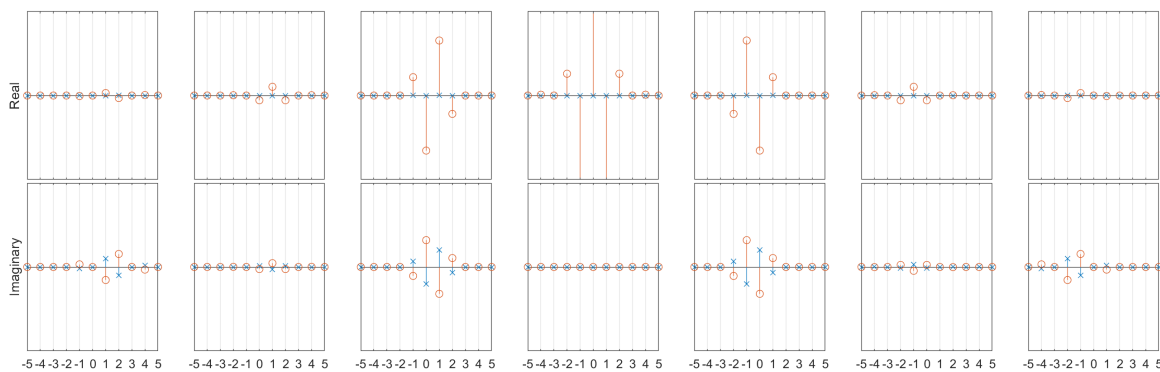
Figure 2.8: *A comparison of the real and imaginary part of the light-curve from the original map (red with 'o') and the difference between the original map and the reconstructed map (blue with '×'). Each column corresponds to a value of n, ranging from -3 to 3, and each in each plot, the value of k ranges from -5 to 5.*
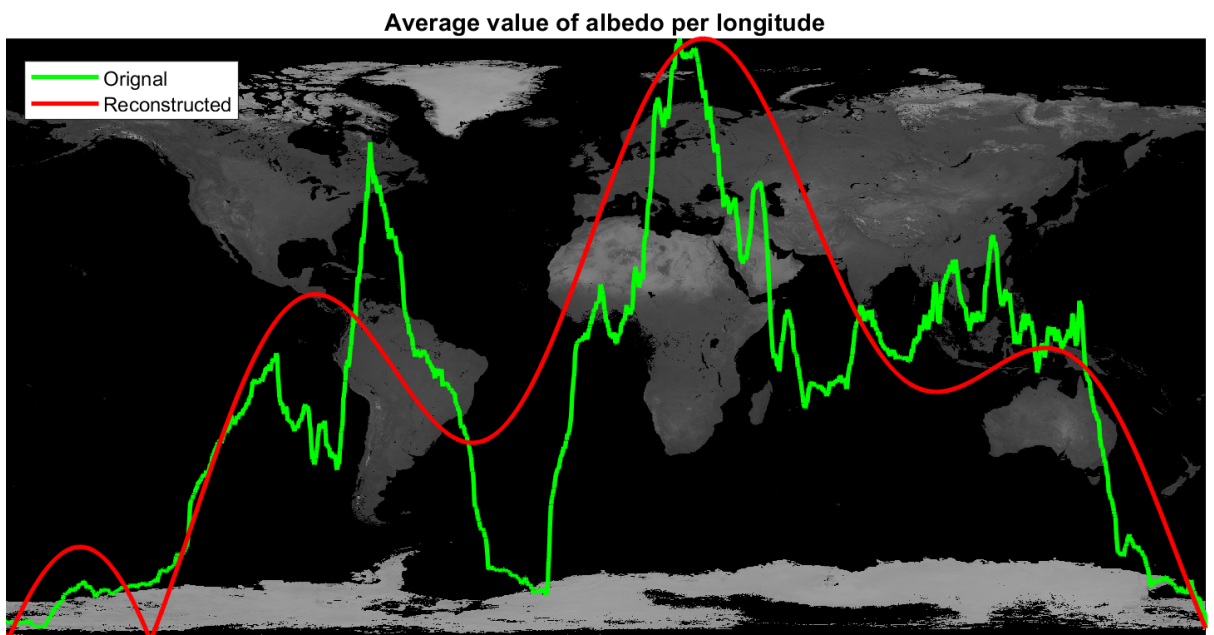
Figure 2.9: *The (absolute value of the) average of both the original and the reconstructed map for every longitude compared. In green, the longitudinal average of the original map. In red the longitudinal average of the reconstructed map. Notice the presence of negative albedo around the pacific ocean.*
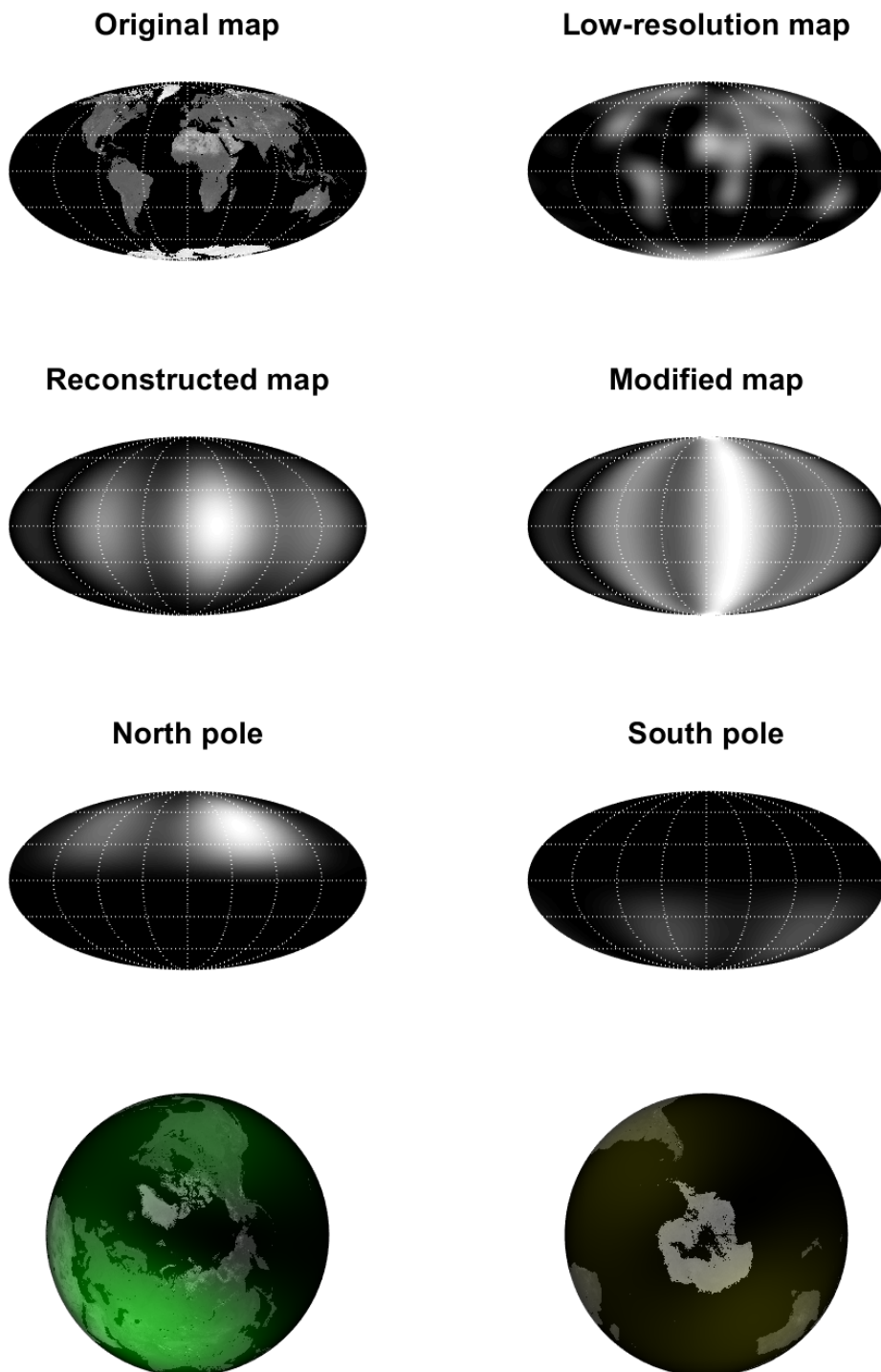
Figure 2.10: *Reconstruction of Earth's albedo map for face-observation with zero tilt (β = 0). In the first row, the original map and the map with spherical harmonics up to l = 10 are plotted. In the second row, the reconstructed maps of the northern and southern hemisphere are plotted in the first and third column respectively. They are plotted together with the real map of earth in the second and fourth columns. All plots do not display negative albedo, negative values are made black.*

CHAPTER 3

MAPPING A PLANET WITH TILTED SPIN AXIS

In the last chapter, we considered planets with no axial tilt. Although this simplified the problem to a set of linear equations, it also limited the applications and deformed the recovered map. In this chapter we shall investigate what happens if we do not restrict ourselves to zero axial tilt, and shall see that we can still find some workable equations. First, a extensive description of the physical system is given, and the characteristic angles are explained. Next, the 'machinery' which is used is treated. Last, this is applied to edge-, and face-on observations of exoplanets, and the results when this theory is applied to an exoplanet with the surface map of Earth are presented.

3.1   Parameters of axial tilt

Consider the situation as shown in figure 3.1, an expansion of figure 1.1 on page 6. We choose our basis vectors such that the x-y plane is the orbital plane of the planet, and let $\hat{\mathbf{x}}$ be parallel to the projection of $\hat{\mathbf{o}}$ on the x-y plane. As in the previous chapters, the planet is orbiting the star with angular speed ω, the annual revolution. Second, the planet is rotating around it's own north-south pole spin axis , $\hat{\mathbf{n}}$, with Ω, the diurnal rotation. The difference with the previous chapter is that $\hat{\mathbf{n}} \neq \pm\hat{\mathbf{z}}$; the has a tilted spin axis. This is described by the axial tilt:

Definition 3.1. *The axial tilt (α, β) of an exoplanet gives the orientation of its spin axis with respect to the observer.* $\hat{\mathbf{n}} = (\cos\alpha\sin\beta, \sin\alpha\sin\beta, \cos\beta)^T$ *with:*

- *α is the angle ϕ at winter solstice.*

- *β, the obliquity, is the angle between $\hat{\mathbf{n}}$ and $\hat{\mathbf{z}}$.*

The reason why we refer to the angles that define the axial tilt as α and β instead of using a notation that is more common under astronomers (which refer to the angles as Θ_{eq} and i respectively) will become apparent in the next sections, when we determine the reflective light-curve with equation 1.2.

Both angles are visualized in figure 3.1. In the upper figure, α is shown. Since the projection of $\hat{\mathbf{o}}$ is parallel to $\hat{\mathbf{x}}$, ϕ is the angle between $\hat{\mathbf{r}}$ and $\hat{\mathbf{x}}$. When the planet revolves around the star, different parts of it are illuminated. At summer solstice, the north pole is closest to the star; it is summer on the northern hemisphere. At winter equinox, the north pole is furthest from the star; it is winter on the northern hemisphere. Spring and fall equinox are located between summer and winter solstice. α determines where these events occur. When the planet is located at $\phi = \alpha$, winter solstice occurs. α can take on any value in the interval $[0, 2\pi)$.

In the lower figure β is shown. We observe the situation in the x-y plane. β, or the *obliquity*, is the angle between the normal vector of the orbital plane, $\hat{\mathbf{z}}$, and the spin axis $\hat{\mathbf{n}}$. In theory, β can take on any value from the interval $[0, \pi]$, but in practice it is often small, either close to 0 or to π. For example, Mercury has $\beta = 0.01°$, and Jupiter has $\beta = 3.13°$. The major exception in our solar system is Uranus, spinning almost perpendicular to its orbital plane.

For face-on observations, the projection of $\hat{\mathbf{o}}$ on the x-y plane is $\mathbf{0}$, such that α is underdetermined. However, we don't need to. We fix $\hat{\mathbf{x}}$ such that winter solstice occurs when $\Phi = 0$.
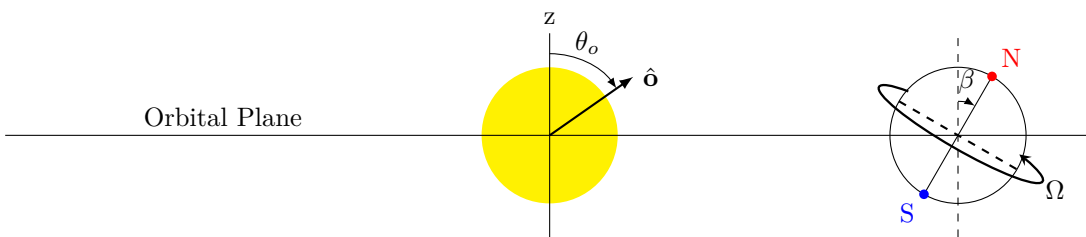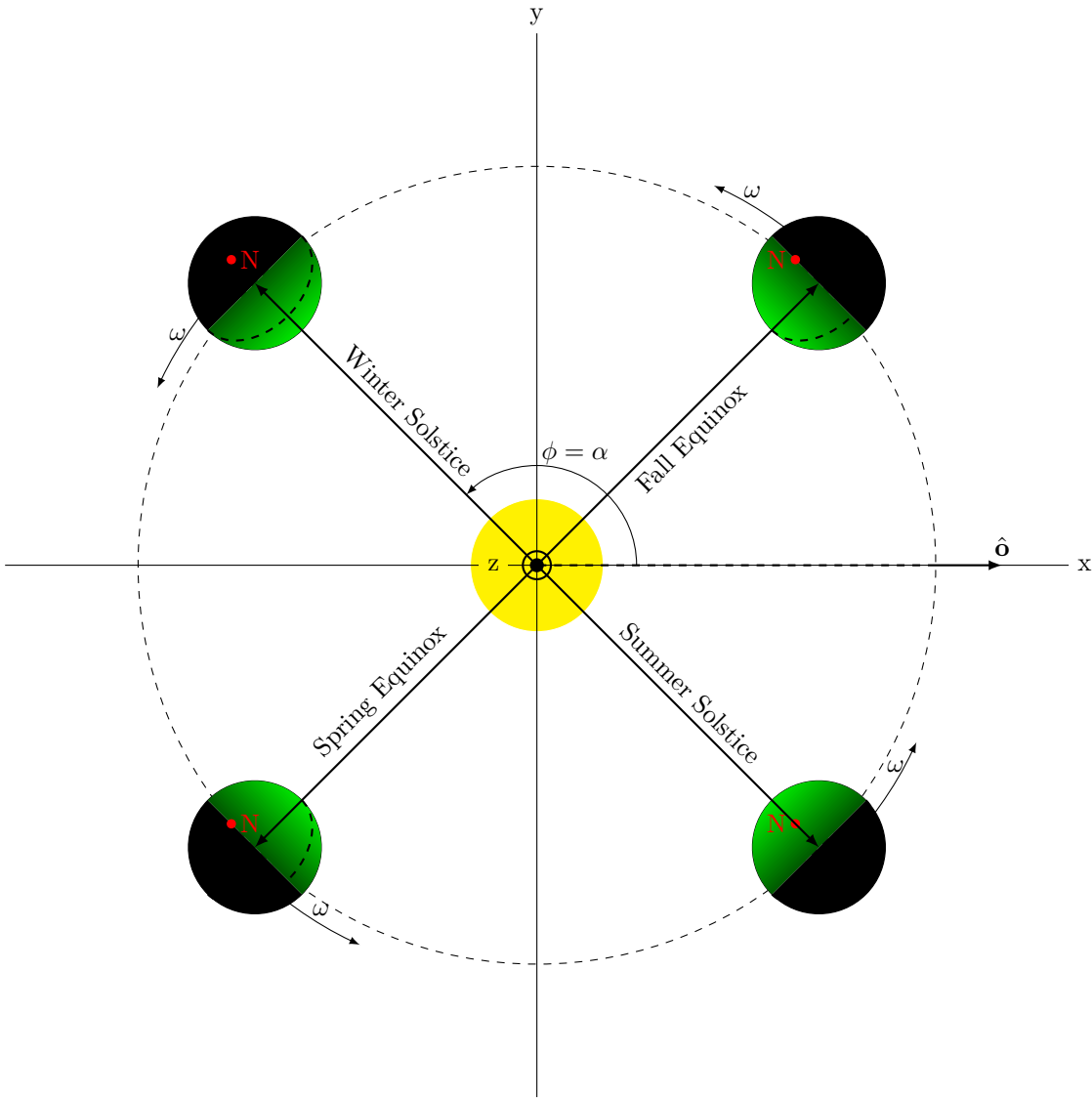
Figure 3.1: *General situation for observation of an exoplanet. On top of the existing parameters from figure 1.1. We add two new angles that describe the tilt of the planet: α gives the angle between $\hat{\mathbf{x}}$ and $\hat{\mathbf{r}}$ at winter solstice, and β gives the angle between $\hat{\mathbf{z}}$ and $\hat{\mathbf{n}}$. In this report, we only consider situations with $\theta_o = 0$ (face-on observation) or $\theta_o = \pi/2$ (edge-on observation).*

3.2   Euler Angles

In order to calculate the light-curve for a planet with nonzero axial tilt, we shall need rotations with the so-called Euler angles.

3.2.1   ROTATION WITH EULER ANGLES

A rotation with the **Euler angles** (see also [Goldstein, 1950] or [Wikipedia, 2018a]), are defined as follows. Suppose we start in coordinate system **E**, with unit vectors $(\hat{\mathbf{x}}, \hat{\mathbf{y}}, \hat{\mathbf{z}})$. We rotate three times: around the z-axis, the new y-axis, and than around the new z-axis. The first rotation is with an angle α, and with this we arrive in coordinate system with unit vectors $(\hat{\mathbf{u}}, \hat{\mathbf{v}}, \hat{\mathbf{z}})$. Now we rotate around the u-axis with an angle of $\beta \in [-\pi/2, \pi/2]$, and arrive in coordinate system $(\hat{\mathbf{w}}, \hat{\mathbf{v}}, \hat{\mathbf{z}}')$. The last rotation is around the z-axis with an angle of γ. Now we arrive in coordinate system **F**, which has unit vectors $(\hat{\mathbf{x}}', \hat{\mathbf{y}}', \hat{\mathbf{z}}')$. The process can be seen in figure 3.2 [1].
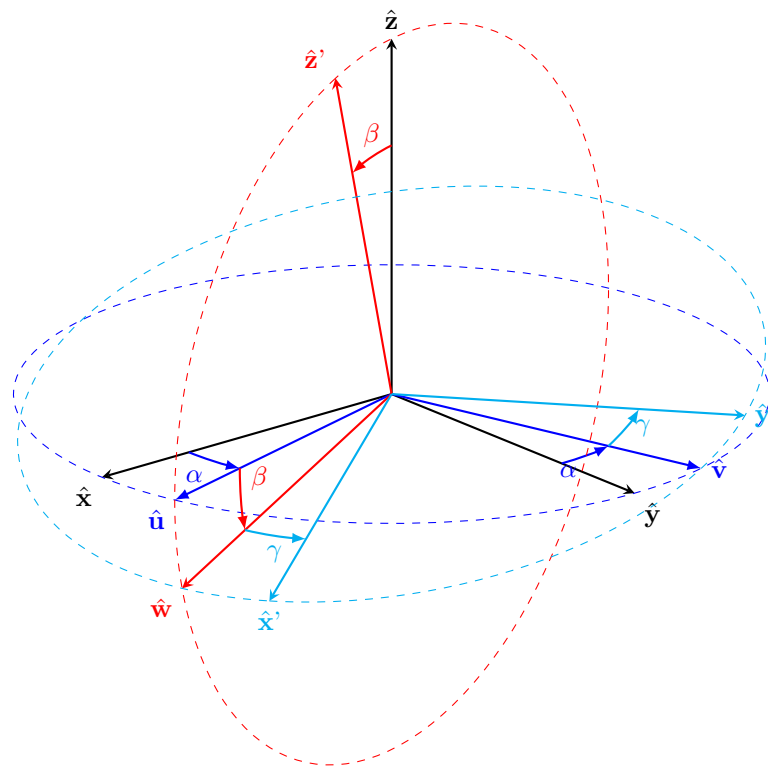
Figure 3.2: *A rotation with Euler Angles (α, β, γ) from coordinate system $\boldsymbol{E}$ with unit vectors $(\hat{\boldsymbol{x}}, \hat{\boldsymbol{y}}, \hat{\boldsymbol{z}})$ to coordinate system $\boldsymbol{F}$ with unit vectors $(\hat{\boldsymbol{x}}', \hat{\boldsymbol{y}}', \hat{\boldsymbol{z}}')$ First we rotate with α around the z-axis, than we rotate with β around the v-axis, and last we rotate around the z-axis with γ. [Figure source code: [Depriester, 2017]]*

.

This rotation can be summarized with the Euler Angles (α, β, γ) (sometimes denoted with (θ, ψ, ϕ)), and rotates **E** to an arbitrary system **F**. The order in which we apply the rotations is not unique, in fact there are six orders in which we can rotate the system, this particular one is called the z-y-z rotation, for obvious reasons.

---

[1]See also: `http://demonstrations.wolfram.com/EulerAngles/` by Frederick W. Strauch

3.2.2 SPHERICAL HARMONICS ROTATION AND THE WIGNER D MATRIX

The reason why we need Euler angles is the following property. Let u be a function defined on the unit sphere, and let P be a point on the unit sphere represented in coordinate system $\mathbf{E}$ by (θ, ϕ), we can write $u(\theta, \phi) = \sum_{l,m} M_l^m Y_l^m(\theta, \phi)$ (under reasonable assumptions for u). Rotate $\mathbf{E}$ with Euler angles (α, β, γ) such that we arrive in $\mathbf{F}$, and let (θ', ϕ') be the representation of P in $\mathbf{F}$. Then:

$$u(\theta', \phi') = \sum_{l=0}^{\infty} \sum_{m'=-l}^{l} M_l^{m'} Y_l^{m'}(\theta', \phi') \tag{3.1}$$

where

$$M_l^{m'} = \sum_{m=-l}^{l} D_l^{m'm} M_l^m \tag{3.2}$$

The D-coefficients ("D" for Darstellung, meaning "representation" in German) are given by:

$$D_l^{m',m} = e^{i(m\gamma + m'\alpha)} d_l^{m'm}(\beta) \tag{3.3}$$

where the d-coefficients are the elements of Wigner's small d-matrix [2]

$$d_l^{m'm} = (-1)^{m'-m}[(l+m')!(l-m')!(l+m)!(l-m)!]^{1/2} \sum_s \left[\frac{(-1)^{m'-m+s}}{(l+m-s)!s!(m'-m+s)!(l-m'-s)!} \right.$$
$$\left. (\cos\beta/2)^{2l+m-m'-2s}(\sin\beta/2)^{m'-m+2s} \right] \tag{3.4}$$

where the sum over s runs from all values for which the factorials are positive [for a short overview, see also: [Gimbutas and Greengard, 2009], or at the source itself [Wigner, 1927]]. We also set $d_l^{m'm}(\beta) = 0$ if $|m| > l$, this will be convenient later on.

If we assume $\beta << 1$ we can approximate the Wigner small d matrix as a matrix with only diagonal an off-diagonal entries (see [Hoffmann, 2018]). The first order approximations of the three first Wigner small d matrices are:

$$d_1(\beta) = \begin{pmatrix} 1 \end{pmatrix}$$

$$d_2(\beta) = \begin{pmatrix} \cos^2\left(\frac{\beta}{2}\right) & -\frac{\sin(\beta)}{\sqrt{2}} & \sin^2\left(\frac{\beta}{2}\right) \\ \frac{\sin(\beta)}{\sqrt{2}} & \cos(\beta) & -\frac{\sin(\beta)}{\sqrt{2}} \\ \sin^2\left(\frac{\beta}{2}\right) & \frac{\sin(\beta)}{\sqrt{2}} & \cos^2\left(\frac{\beta}{2}\right) \end{pmatrix} = \begin{pmatrix} 1 & -\frac{\beta}{\sqrt{2}} & 0 \\ \frac{\beta}{\sqrt{2}} & 1 & -\frac{\beta}{\sqrt{2}} \\ 0 & \frac{\beta}{\sqrt{2}} & 1 \end{pmatrix} + \mathcal{O}(\beta^2)$$

$$d_3(\beta) = \begin{pmatrix} 1 & -\beta & 0 & 0 & 0 \\ \beta & 1 & -\sqrt{\frac{3}{2}}\beta & 0 & 0 \\ 0 & \sqrt{\frac{3}{2}}\beta & 1 & -\sqrt{\frac{3}{2}}\beta & 0 \\ 0 & 0 & \sqrt{\frac{3}{2}}\beta & 1 & -\beta \\ 0 & 0 & 0 & \beta & 1 \end{pmatrix} + \mathcal{O}(\beta^2)$$

Here m varies over the columns and m' over the rows. Notice that the only entry on the diagonal is '1', and to make a good first order approximation we only need the off-diagonal elements $m' = m \pm 1$.

---

[2] Eugene Wigner was a Hungarian-American theoretical physicist, who performed significant research in the field of quantum mechanics, even earning him the Nobel Prize in Physics in 1963. The D-matrix also originated from rotations in quantum mechanics.

3.3   The Fourier coefficients for edge-on observation

Now we will apply rotation with Euler angles to the situation from figure 3.1 for an edge-on observation. We repeat the scheme from paragraph 2.2. Suppose we take coordinate system $\mathbf{P}$ as the planets frame, in which the albedo map is independent of the time (which is the inhabitants perspective): $M_P(\theta_p, \phi_p) = \sum_{l=0}^{\infty} \sum_{m=-l}^{l} M_l^m Y_l^m(\theta_p, \phi_p)$. Now the suggestive naming of the angles from section 3.1 is useful. If we want to get from the observers coordinate system $\mathbf{O}$ to $\mathbf{P}$ we take the Euler angles $(\alpha, \beta, \Omega t - \alpha)$ [3]. Thus if we want to invert this rotation, we rotate the map in the $\mathbf{P}$ frame with angles $(\alpha - \Omega t, -\beta, -\alpha)$. This gives that our map in $\mathbf{O}$ looks like:

$$M_O(\theta_p, \phi_p) = \sum_{l=0}^{\infty} \sum_{m'=-l}^{l} \left[\sum_{m=-l}^{l} e^{i(m(-\alpha)+m'(\alpha - \Omega t))} d_l^{m'm}(-\beta) M_l^m \right] Y_l^{m'}(\theta_p, \phi_p) \tag{3.5}$$

Now we return to the derivation of the Fourier coefficients of the light-curve from chapter 2. We have that the light-curve of a planet is given by:

$$
\begin{aligned}
f(\phi, \Phi) &= \frac{1}{\pi R^2} \iint_{\mathbb{D}} (-\hat{\mathbf{r}} \cdot \hat{\mathbf{s}})(\hat{\mathbf{s}} \cdot \hat{\mathbf{o}}) M(\mathbf{s}, t) d^2 S \\
&= \sum_{l=0}^{\infty} \sum_{m,m'} \frac{M_l^m}{\pi R^2} d_l^{m',m} e^{-i(m'\Phi + (m-m')\alpha)} \iint_{\mathbb{D}} (-\hat{\mathbf{r}} \cdot \hat{\mathbf{s}})(\hat{\mathbf{s}} \cdot \hat{\mathbf{o}}) Y_l^{m'}(\mathbf{s}) d^2 S \\
&= \sum_{l=0}^{\infty} \sum_{m,m'} \frac{s^2 M_l^m}{\pi R^2} d_l^{m',m} e^{-i(m'\Phi + (m-m')\alpha)} y_l^{m'} \int_0^{2\pi} \cos^+(\phi_p) \cos^+(\phi_p - \phi - \pi) e^{im'\phi_p} d\phi_p
\end{aligned}
$$

The equations and steps we make here are similar to those that we have already taken in chapter 2, but now with an extra term and summation that accounts for the rotation of the planet's axis. We can retrieve the Fourier coefficients in the same way as we did before, we take the inner product of f with $e^{i(n\Phi + k\phi)}$:

$$
\begin{aligned}
(2\pi)^2 f_k^n &= \int_0^{2\pi} \int_0^{2\pi} f(\phi, \Phi) e^{-i(k\phi + n\Phi)} d\phi d\Phi \\
&= \sum_{l=0}^{\infty} \sum_{m,m'} \frac{s^2 M_l^m d_l^{m',m} y_l^{m'} e^{-i(m-m')\alpha}}{\pi R^2} \\
&\quad \int_0^{2\pi} \int_0^{2\pi} \left[e^{-im'\Phi} \int_0^{2\pi} \cos^+(\phi_p) \cos^+(\phi_p - \phi - \pi) e^{im'\phi_p} d\phi_p \right] e^{-i(k\phi + n\Phi)} d\phi d\Phi \\
&= \sum_{l=0}^{\infty} \sum_{m,m'} \frac{s^2 M_l^m d_l^{m',m} y_l^{m'} e^{-i(m-m')\alpha}}{\pi R^2} 2\pi \delta_{m',-n} \\
&\quad \int_0^{2\pi} \int_0^{2\pi} \cos^+(\phi_p) \cos^+(\phi_p - \phi - \pi) e^{i(m'\phi_p - k\phi)} d\phi_p d\phi \\
&= \sum_{l=0}^{\infty} \sum_{m,m'} \frac{s^2 M_l^m d_l^{m',m} y_l^{m'} e^{-i(m-m')\alpha}}{\pi R^2} 2\pi \delta_{m',-n} \mathcal{G}_k^{-m'} \\
&= \frac{2s^2}{R^2} \mathcal{G}_k^n \sum_{l=|n|}^{\infty} y_l^{-n} \left[\sum_{m=-l}^{l} d_l^{-n,m}(-\beta) e^{-i(m+n)\alpha} M_l^m \right]
\end{aligned}
$$

The equation has the same structure as equations 2.11, which we found in chapter 2. The difference is that we are now summing over two indices, which means that every spherical harmonic can contribute to every coefficient in the light-curve. The equation for the Fourier-coefficients of the light-curve in terms of the coefficients of the map is:

$$\boxed{f_k^n = \frac{s^2}{R^2} \sum_{l=|n|}^{\infty} \sum_{m=-l}^{l} \left[2(-1)^k c_k c_{k+n} y_l^{-n} d_l^{-n,m}(-\beta) e^{-i(m+n)\alpha} \right] M_l^m} \tag{3.6}$$

---

[3] The reason for the inclusion of $-\alpha$ in the last angle is that for $\beta=0$, any value of α should return the same light-curve, and this term guaranties that it does so. This will be shown at the end of this paragraph.

Similar to the table from chapter two, the values of the coefficients (divided by a factor of s^2/R^2) can be put together in a linear transformation $\mathbf{f} = A_{\alpha,\beta}(\mathbf{M})$, and we can represent any part of it as a matrix. Such a part of A can be seen in table 3.1. For readability purposes, the coefficients are Taylor expander around $\beta = 0$, and only the zeroth and first order terms in β are displayed. If we compare this table to table 2.1, we can see that every non-zero entry has a copied itself to the left and/or the the right, depending on the value of m.

Finally, if we substitute $\beta = 0$ equation 3.6, we get:

$$[f_k^n]_{\beta=0} = \left[\frac{s^2}{R^2} \sum_{l=|n|}^{\infty} \sum_{m=-l}^{l} \left[2(-1)^k c_k c_{k+n} y_l^{-n} d_l^{-n,m}(-\beta) e^{-i(m+n)\alpha} \right] M_l^m \right]_{\beta=0}$$

$$= \frac{s^2}{R^2} \sum_{l=|n|}^{\infty} \sum_{m=-l}^{l} \left[2(-1)^k c_k c_{k+n} y_l^{-n} \delta_{-n,m} e^{-i(m+n)\alpha} \right] M_l^m$$

$$= \frac{s^2}{R^2} \sum_{l=|n|}^{\infty} \left[2(-1)^k c_k c_{k+n} y_l^{-n} e^{-i(-n+n)\alpha} \right] M_l^{-n}$$

$$= \frac{s^2}{R^2} \sum_{l=|n|}^{\infty} 2(-1)^k c_k c_{k+n} y_l^{-n} M_l^{-n}$$

This is just equation 2.11 for a planet with no tilt.

3.4   The Fourier coefficients for face-on observation

Last, the expression of the Fourier coefficients for an edge-on observation has been determined. There is one major difference between what we did in the last paragraph and what we will do now: there is no dependence on α. If you look on top of the planet, there is only one way in which the planet can be tilted: the direction of β.

Once again: in the planet's frame, the albedo map is given by $M_P(\theta_p, \phi_p) = \sum_{l=0}^{\infty} \sum_{m=-l}^{l} M_l^m Y_l^m(\theta_p, \phi_p)$. Now, if we want to go from the observers frame to the planet's frame we rotate with $(0,\beta,\Omega t)$. We get the albedo map:

$$M_O(\theta_p, \phi_p) = \sum_{l=0}^{\infty} \sum_{m'=-l}^{l} \left[\sum_{m=-l}^{l} e^{-im'\Omega t} d_l^{m'm}(-\beta) M_l^m \right] Y_l^{m'}(\theta_p, \phi_p) \tag{3.7}$$

Substituting this in the light-curve equation gives:

$$
\begin{aligned}
f(\phi, \Phi) &= \sum_{l,m,m'} \frac{M_l^m d_l^{m'm}}{\pi R^2} e^{-im'\Phi} \iint_{\mathbb{D}} (-\hat{\mathbf{r}} \cdot \hat{\mathbf{s}})(\hat{\mathbf{s}} \cdot \hat{\mathbf{o}}) Y_l^{m'}(\mathbf{s}) d^2 S \\
&= \sum_{l,m,m'} \frac{M_l^m d_l^{m'm}}{\pi R^2} e^{-im'\Phi} \int_0^{2\pi} \int_0^1 \left[\cos^+(\phi_p - \phi - \pi)\sqrt{1-z^2} \right] z \left[\mathcal{N}_l^{m'} P_l^{m'}(z) e^{im'\phi_p} \right] s^2 dz d\phi_p \\
&= \sum_{l,m,m'} \frac{M_l^m d_l^{m'm}}{\pi R^2} \int_0^1 \mathcal{N}_l^{m'} z \sqrt{1-z^2} P_l^{m'}(z) dz \int_0^{2\pi} \cos^+(\phi_p - \phi - \pi) e^{im'(\phi_p - \Phi)} d\phi_p \\
&= \sum_{l,m,m'} \frac{s^2 d_l^{m'm}}{\pi R^2} M_l^m y_l^{m'} \int_0^{2\pi} \cos^+(\phi_p - \phi - \pi) e^{im'(\phi_p - \Phi)} d\phi_p
\end{aligned}
$$

And we project this on the base functions of f:

$$
\begin{aligned}
(2\pi)^2 f_k^n &= \iint f(\phi, \Phi) e^{-i(k\phi + n\Phi)} d\phi d\Phi \\
&= \frac{s^2}{\pi R^2} \sum_{l,m,m'} M_l^m d_l^{m'm} y_l^{m'} \iiint \cos^+(\phi_p - \phi - \pi) e^{im'(\phi_p - \phi)} e^{-i(k\phi + n\Phi)} d\phi d\Phi d\phi_p \\
&= \frac{s^2}{\pi R^2} \sum_{l,m,m'} M_l^m d_l^{m'm} y_l^{m'} (2\pi \delta_{m',-n}) \mathcal{G}_k^{-m'}
\end{aligned}
$$

And after filling in the definition for $\mathcal{G}$ from equation 2.13 on page 21, we get:

$$\boxed{f_k^n = \frac{2s^2}{R^2}(-1)^n c_n \delta_{n,-k} \sum_{l=|n|}^{\infty} \sum_{m=-l}^{l} y_l^{-n} d_l^{-nm}(-\beta) M_l^m} \tag{3.8}$$

Such a part of the transformation can be seen in table 3.2. In can be shown that is we substitute $\beta = 0$, we return to the expression of equation 2.14.

3.5   Recovering Earths albedo map with known axial tilt

In this section we present the results of application(s) of the methods that we have discussed in this chapter to Earths albedo map. The theory has been applied to other albedo maps as well. The results of this can be found in the appendix.

Equations 3.6 and 3.8, combined with our knowledge of the pseudoinverse from chapter 2.3, gives us a method to recover the map of an exoplanet with known axial tilt. Given an input map M, and axial tilt α and β, we can simulate a recovery of the map:

$$\hat{\mathbf{M}} = [A(\alpha, \beta)]^+ \mathbf{f} \approx [A(\alpha, \beta)]^+ A(\alpha, \beta)_{20} \mathbf{M}_{20}$$

where the subscript 20 denotes that we take only the spherical harmonics with $L = 20$ in account for contributions to the light-curve. An appropriate value for the maximum of l in the recovered map can be determined by looking at the number of independent columns in A. As we will demonstrate in the second part of this section, for $|n| \leq 3$, we need $l \leq 7$, irrespective of whether this is edge-on or face-on.

The results of this process can be seen in figures 3.3, 3.4 and 3.5 for edge-on observations, and figure 3.6 for face-on observations. The results for the edge-on observations are presented for three different values for α and three different values for β. Each figure has a constant value of α. In the top row, the original surface map is displayed, along with the maximum recoverable map:

$$\sum_{l=0}^{L} \sum_{m=-l}^{l} M_l^m Y_l^m(\theta_p, \phi_p)$$

In the second row, the reconstructed maps are plotted, each column corresponds to a value of β. In the third row, the reconstructed maps are plotted over the original map.

Since the face-on observation has no α dependence, only one figure is needed. However, we now have two observations per β value: observations of the north- and south-pole. The reconstructed maps of these observations can be found in the second and third row respectively. Besides the Earth, some other planets and artificial maps have also been tested. The results of this can be found in appendix B (edge-on observation) and C (face-on observation).

Table 3.1: *The transformation from equation 3.6 (edge-on observation), linearized in β around $\beta = 0$. The coefficients have been multiplied with a factor R^2/s^2.*

	M_0^0	M_1^{-1}	M_1^0	M_1^1	M_2^{-2}	M_2^{-1}	M_2^0	M_2^1	M_2^2	M_3^{-3}	M_3^{-2}	M_3^{-1}	M_3^0	M_3^1	M_3^2	M_3^3
f_{-2}^{-2}	0	0	0	0	0	0	0	$\frac{4\sqrt{2/15}e^{i\alpha}}{45\pi^{5/2}}\beta$	$\frac{4\sqrt{2/15}}{45\pi^{5/2}}$	0	0	0	0	0	0	0
f_{-1}^{-2}	0	0	0	0	0	0	0	0	0	0	0	0	0	0	0	0
f_{0}^{-2}	0	0	0	0	0	0	0	$-\frac{4\sqrt{2/15}e^{i\alpha}}{3\pi^{5/2}}\beta$	$\frac{4\sqrt{2/15}}{3\pi^{5/2}}$	0	0	0	0	0	0	0
f_{1}^{-2}	0	0	0	0	0	0	0	$\frac{e^{i\alpha}}{2\sqrt{30}\pi}\beta$	$-\frac{1}{2\sqrt{30}\pi}$	0	0	0	0	0	0	0
f_{2}^{-2}	0	0	0	0	0	0	0	$-\frac{4\sqrt{2/15}e^{i\alpha}}{3\pi^{5/2}}\beta$	$\frac{4\sqrt{2/15}}{3\pi^{5/2}}$	0	0	0	0	0	0	0
f_{-2}^{-1}	0	0	0	0	0	0	0	0	0	0	0	0	0	$-\frac{1}{256}\sqrt{\frac{7}{3\pi}}$	0	0
f_{-1}^{-1}	0	0	$-\frac{1}{64}e^{i\alpha}\sqrt{\frac{3}{\pi}}\beta$	$\frac{1}{32}\sqrt{\frac{3}{2\pi}}$	0	0	0	0	0	0	0	0	$\frac{1}{256}e^{i\alpha}\sqrt{\frac{7}{\pi}}\beta$	$\frac{1}{256}\sqrt{\frac{21}{\pi}}$	$-\frac{1}{256}e^{-i\alpha}\sqrt{\frac{35}{6\pi}}\beta$	0
f_{0}^{-1}	0	0	$\frac{3}{64}e^{i\alpha}\sqrt{\frac{3}{\pi}}\beta$	$\frac{1}{32}(-3)\sqrt{\frac{3}{2\pi}}$	0	0	0	0	0	0	0	0	$\frac{1}{256}(-3)e^{i\alpha}\sqrt{\frac{7}{\pi}}\beta$	$-\frac{\sqrt{21}}{256}$	$\frac{1}{256}e^{-i\alpha}\sqrt{\frac{105}{2\pi}}\beta$	0
f_{1}^{-1}	0	0	$\frac{1}{64}(-3)e^{i\alpha}\sqrt{\frac{3}{\pi}}\beta$	$\frac{3}{32}\sqrt{\frac{3}{2\pi}}$	0	0	0	0	0	0	0	0	$\frac{3}{256}e^{i\alpha}\sqrt{\frac{7}{\pi}}\beta$	$\frac{1}{256}\sqrt{\frac{7}{3\pi}}$	$-\frac{1}{256}e^{-i\alpha}\sqrt{\frac{105}{2\pi}}\beta$	0
f_{2}^{-1}	0	0	$\frac{1}{64}e^{i\alpha}\sqrt{\frac{3}{\pi}}\beta$	$-\frac{1}{32}\sqrt{\frac{3}{2\pi}}$	0	0	0	0	0	0	0	0	$-\frac{1}{256}e^{i\alpha}\sqrt{\frac{7}{\pi}}\beta$	0	$\frac{1}{256}e^{-i\alpha}\sqrt{\frac{35}{6\pi}}\beta$	0
f_{-2}^{0}	$\frac{4}{27\pi^{5/2}}$	0	0	0	0	$\frac{2\sqrt{2/15}e^{i\alpha}}{9\pi^{5/2}}\beta$	$-\frac{4}{27\sqrt{5}\pi^{5/2}}$	$\frac{2\sqrt{2/15}e^{-i\alpha}}{9\pi^{5/2}}\beta$	0	0	0	0	0	0	0	0
f_{-1}^{0}	$-\frac{1}{12\sqrt{\pi}}$	0	0	0	0	$-\frac{e^{i\alpha}}{4\sqrt{30}\pi}\beta$	$\frac{1}{12\sqrt{5\pi}}$	$-\frac{e^{-i\alpha}}{4\sqrt{30}\pi}\beta$	0	0	0	0	0	0	0	0
f_{0}^{0}	$\frac{4}{3\pi^{5/2}}$	0	0	0	0	$\frac{2\sqrt{2/15}e^{i\alpha}}{\pi^{5/2}}\beta$	$-\frac{4}{3\sqrt{5}\pi^{5/2}}$	$\frac{2\sqrt{2/15}e^{-i\alpha}}{\pi^{5/2}}\beta$	0	0	0	0	0	0	0	0
f_{1}^{0}	$-\frac{1}{12\sqrt{\pi}}$	0	0	0	0	$-\frac{e^{i\alpha}}{4\sqrt{30}\pi}\beta$	$\frac{1}{12\sqrt{5\pi}}$	$-\frac{e^{-i\alpha}}{4\sqrt{30}\pi}\beta$	0	0	0	0	0	0	0	0
f_{2}^{0}	$\frac{4}{27\pi^{5/2}}$	0	0	0	0	$\frac{2\sqrt{2/15}e^{i\alpha}}{9\pi^{5/2}}\beta$	$-\frac{4}{27\sqrt{5}\pi^{5/2}}$	$\frac{2\sqrt{2/15}e^{-i\alpha}}{9\pi^{5/2}}\beta$	0	0	0	0	0	0	0	0
f_{-2}^{1}	0	$\frac{1}{32}\sqrt{\frac{3}{2\pi}}$	$\frac{1}{64}e^{-i\alpha}\sqrt{\frac{3}{\pi}}\beta$	0	0	0	0	0	0	0	0	$-\frac{1}{256}\sqrt{\frac{7}{3\pi}}$	$-\frac{1}{256}e^{-i\alpha}\sqrt{\frac{7}{\pi}}\beta$	0	0	0
f_{-1}^{1}	0	$\frac{1}{32}(-3)\sqrt{\frac{3}{2\pi}}$	$\frac{1}{64}(-3)e^{-i\alpha}\sqrt{\frac{3}{\pi}}\beta$	0	0	0	0	0	0	0	$\frac{1}{256}e^{i\alpha}\sqrt{\frac{35}{6\pi}}\beta$	$\frac{1}{256}\sqrt{\frac{21}{\pi}}$	$\frac{3}{256}e^{-i\alpha}\sqrt{\frac{7}{\pi}}\beta$	0	0	0
f_{0}^{1}	0	$\frac{3}{32}\sqrt{\frac{3}{2\pi}}$	$\frac{3}{64}e^{-i\alpha}\sqrt{\frac{3}{\pi}}\beta$	0	0	0	0	0	0	0	$-\frac{1}{256}e^{i\alpha}\sqrt{\frac{105}{2\pi}}\beta$	$-\frac{\sqrt{21}}{256}$	$\frac{1}{256}(-3)e^{-i\alpha}\sqrt{\frac{7}{\pi}}\beta$	0	0	0
f_{1}^{1}	0	$-\frac{1}{32}\sqrt{\frac{3}{2\pi}}$	$-\frac{1}{64}e^{-i\alpha}\sqrt{\frac{3}{\pi}}\beta$	0	0	0	0	0	0	0	$\frac{1}{256}e^{i\alpha}\sqrt{\frac{105}{2\pi}}\beta$	$\frac{1}{256}\sqrt{\frac{7}{3\pi}}$	$\frac{1}{256}e^{-i\alpha}\sqrt{\frac{7}{\pi}}\beta$	0	0	0
f_{2}^{1}	0	0	0	0	0	0	0	0	0	0	$-\frac{1}{256}e^{i\alpha}\sqrt{\frac{35}{6\pi}}\beta$	0	0	0	0	0
f_{-2}^{2}	0	0	0	0	$\frac{4\sqrt{2/15}}{3\pi^{5/2}}$	$\frac{4\sqrt{2/15}e^{-i\alpha}}{3\pi^{5/2}}\beta$	0	0	0	0	0	0	0	0	0	0
f_{-1}^{2}	0	0	0	0	$-\frac{1}{2\sqrt{30}\pi}$	$-\frac{e^{-i\alpha}}{2\sqrt{30}\pi}\beta$	0	0	0	0	0	0	0	0	0	0
f_{0}^{2}	0	0	0	0	$\frac{4\sqrt{2/15}}{3\pi^{5/2}}$	$\frac{4\sqrt{2/15}e^{-i\alpha}}{3\pi^{5/2}}\beta$	0	0	0	0	0	0	0	0	0	0
f_{1}^{2}	0	0	0	0	0	0	0	0	0	0	0	0	0	0	0	0
f_{2}^{2}	0	0	0	0	$-\frac{4\sqrt{2/15}}{45\pi^{5/2}}$	$-\frac{4\sqrt{2/15}e^{-i\alpha}}{45\pi^{5/2}}\beta$	0	0	0	0	0	0	0	0	0	0

Table 3.2: The transformation from equation 3.8 (face-on observation), linearized in β around $\beta = 0$. The coefficients have been multiplied with a factor R^2/s^2.

	M_0^0	M_1^{-1}	M_1^0	M_1^1	M_2^{-2}	M_2^{-1}	M_2^0	M_2^1	M_2^2	M_3^{-3}	M_3^{-2}	M_3^{-1}	M_3^0	M_3^1	M_3^2	M_3^3
f_{-2}^{-2}	0	0	0	0	0	0	0	0	0	0	0	0	0	0	0	0
f_{-1}^{-2}	0	0	0	0	0	0	0	0	0	0	0	0	0	0	0	0
f_{0}^{-2}	0	0	0	0	0	0	0	0	0	0	0	0	0	0	0	0
f_{1}^{-2}	0	0	0	0	0	0	0	0	0	0	0	0	0	0	0	0
f_{2}^{-2}	0	0	0	0	0	0	0	0	0	0	0	0	0	0	0	0
f_{-2}^{-1}	0	0	0	0	0	0	0	0	0	0	0	0	0	0	0	0
f_{-1}^{-1}	0	0	0	0	0	0	0	0	0	0	0	0	0	0	0	0
f_{0}^{-1}	0	0	0	0	0	0	0	0	0	0	0	0	0	0	0	0
f_{1}^{-1}	0	0	0	0	0	0	0	0	0	0	0	0	0	0	0	0
f_{2}^{-1}	0	0	0	0	0	0	0	0	0	0	0	0	0	0	0	0
f_{-2}^{0}	0	0	0	0	0	$-\frac{\beta}{5\sqrt{6}}$	$\frac{1}{15}$	$\frac{\beta}{5\sqrt{6}}$	0	0	0	0	0	0	0	0
f_{-1}^{0}	0	0	0	0	0	0	0	0	0	0	0	0	0	0	0	0
f_{0}^{0}	$\frac{2}{3}$	0	$-\frac{\beta}{2\sqrt{2}}$	0	0	0	0	0	0	0	0	0	0	0	0	0
f_{1}^{0}	0	$-\frac{\pi\beta}{8\sqrt{2}}$	$\frac{\pi}{8}$	$\frac{\pi\beta}{8\sqrt{2}}$	0	0	0	0	0	0	0	0	0	0	0	0
f_{2}^{0}	0	0	$\frac{\beta}{2\sqrt{2}}$	0	0	0	0	0	0	0	$-\frac{1}{2}\sqrt{\frac{5}{2}}\beta$	0	$-\frac{\sqrt{3}\beta}{2}$	0	$\frac{1}{2}\sqrt{\frac{5}{2}}\beta$	0
f_{-2}^{1}	0	0	0	0	$\frac{6}{5}$	$\frac{6\beta}{5}$	0	0	0	$\frac{15}{16}\sqrt{\frac{3}{2}}\pi\beta$	$-\frac{15}{16}\sqrt{\frac{5}{2}}\pi\beta$	$-\frac{15}{16}\pi$	0	0	0	0
f_{-1}^{1}	0	$\frac{1}{2}$	0	0	0	0	0	0	0	0	0	$\frac{1}{2}$	0	0	0	0
f_{0}^{1}	0	0	0	0	$\frac{4\beta}{5}$	$-\frac{4}{5}$	$-\frac{2\sqrt{6}\beta}{5}$	$\frac{4}{5}$	$\frac{4\beta}{5}$	0	0	$\frac{1}{32}\sqrt{3\pi}\beta$	$-\frac{\pi}{32}$	$-\frac{1}{32}\sqrt{3\pi}\beta$	0	0
f_{1}^{1}	0	0	0	$\frac{1}{2}$	0	0	0	0	0	0	0	0	0	$\frac{1}{2}$	0	0
f_{2}^{1}	0	0	0	0	0	0	0	$-\frac{6\beta}{5}$	$-\frac{6}{5}$	0	0	0	0	$\frac{15\pi}{16}$	$\frac{15}{16}\sqrt{\frac{5}{2}}\pi\beta$	$\frac{15}{16}\sqrt{\frac{3}{2}}\pi\beta$
f_{-2}^{2}	0	0	0	0	0	0	0	0	0	0	0	0	0	0	0	0
f_{-1}^{2}	0	0	0	0	0	0	0	0	0	0	0	0	0	0	0	0
f_{0}^{2}	0	0	0	0	0	0	0	0	0	0	0	0	0	0	0	0
f_{1}^{2}	0	0	0	0	0	0	0	0	0	0	0	0	0	0	0	0
f_{2}^{2}	0	0	0	0	0	0	0	0	0	0	0	0	0	0	0	0

Figure 3.3: *Recovery of the map of Earth for $\alpha = 0°$. In the top row, one can see the original surface, along with the best obtainable surface. In the second row, one can see the reconstructed maps for $\beta = 1°, 30°$, and $90°$ in the first, second and third column respectively. These reconstructions are shown superimposed on the original map in the third row.*
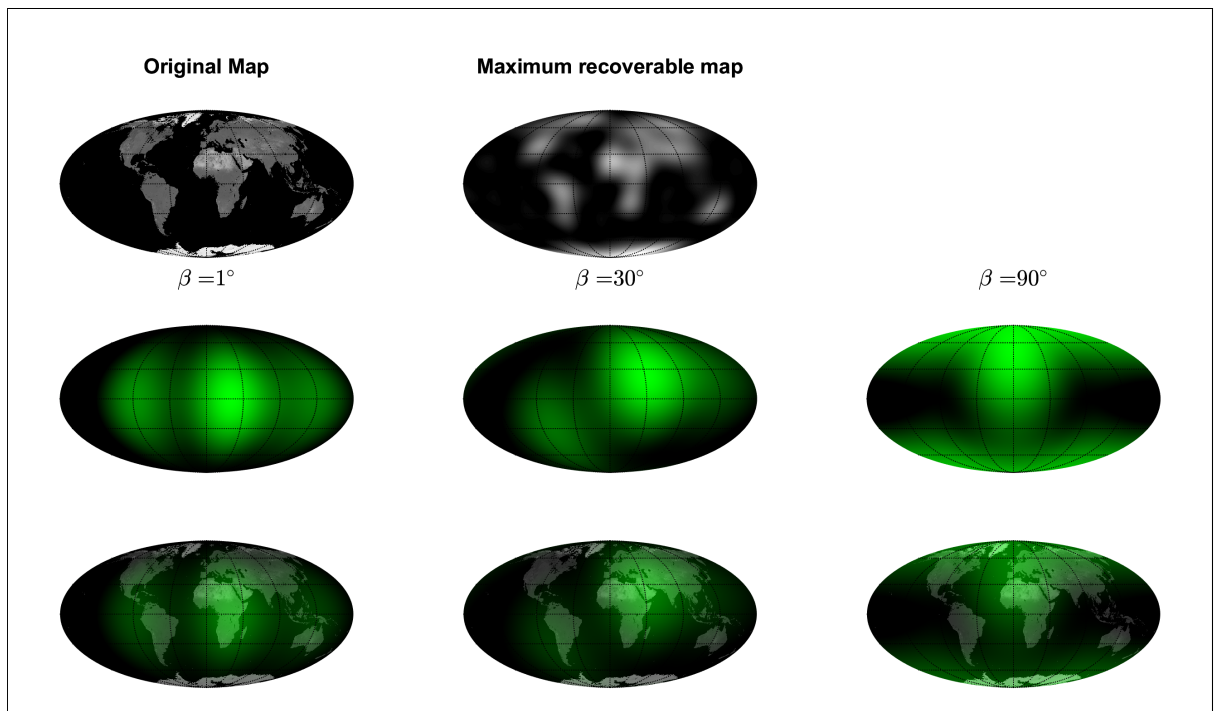
Figure 3.4: *Recovery of the map of Earth for $\alpha = 90°$. The layout is the same as in figure 3.3*
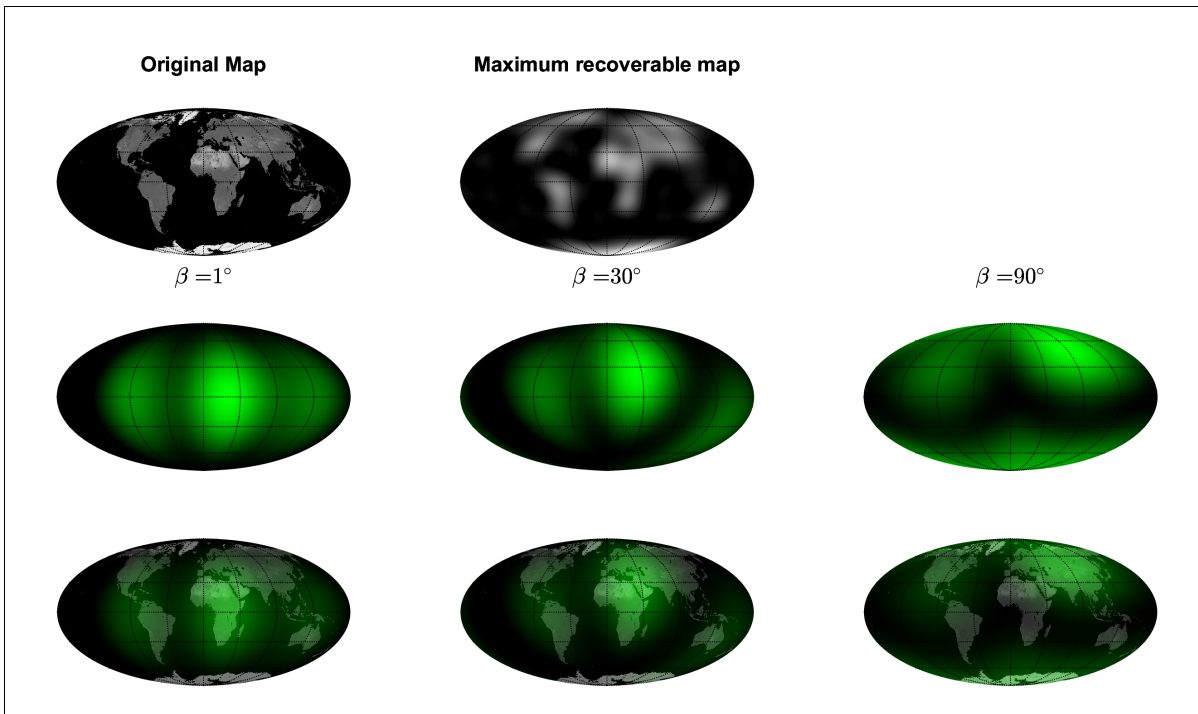
Figure 3.5: *Recovery of the map of Earth for $\alpha = 180°$. The layout is the same as in figure 3.3.*
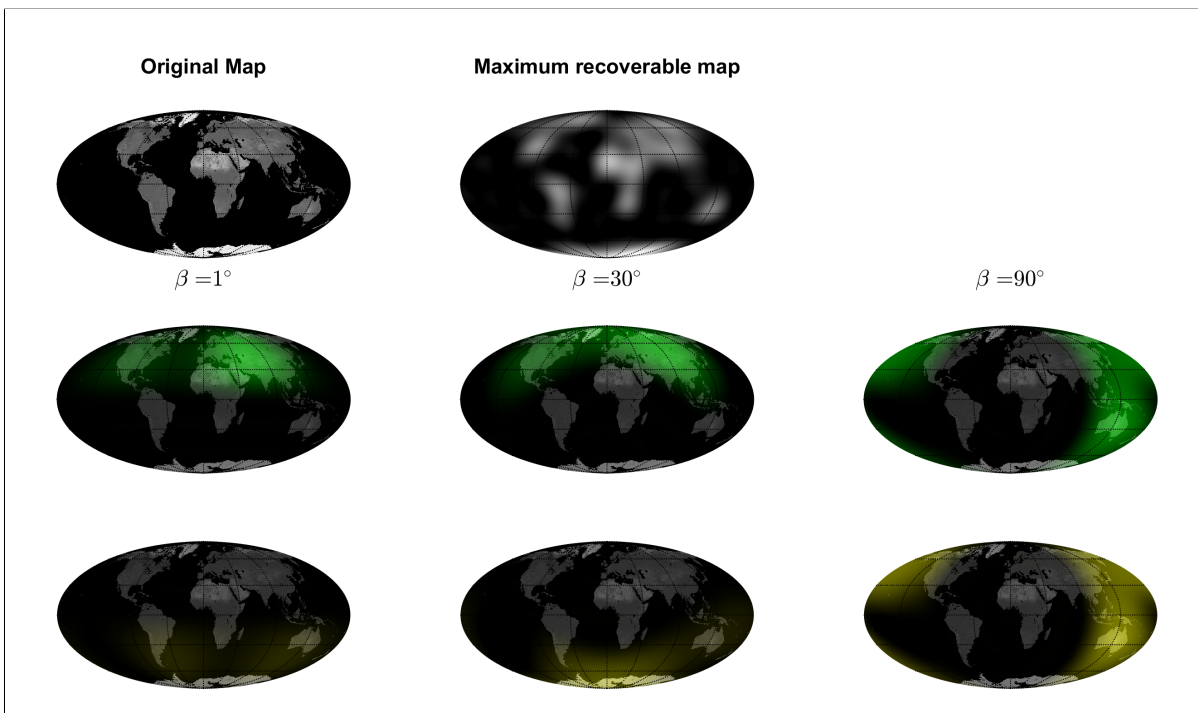
Figure 3.6: *Reconstruction of Earth's albedo map for face-on observation. In the first row, the original map and the map with spherical harmonics up to $l = 10$ are plotted. In the second and third row, the reconstructed maps for observations of the north-, and south-pole respectively are plotted superimposed on the original map. This has been done for $\beta = 1°, 30°$, and $90°$ in the first, second and third column respectively.*

3.6   Symmetries

If we use this method for the edge-on observation, there are a few symmetries in this problem. In order to check that the transformation is correct, we can check that these symmetries hold. Some can be proven directly, whereas others have to be tested numerically. We perform this test on the map which consists only of circles. This map can be found in appendix B and C. We use this map since it has no symmetries in both the longitudinal and latitudinal direction.

3.6.1   SYMMETRIES IN THE SURFACE MAP

- When $\beta = 0$, mirroring the map with respect to the equator shouldn't affect the signal. This means that $M(\theta, \phi) \to M(\pi - \theta, \phi)$. Filling in the surface map gives:

$$M(\pi - \theta, \phi) = \sum_{l,m} M_l^m Y_l^m(\pi - \theta, \phi) = \sum_{l,m} M_l^m (-1)^{l+m} Y_l^m(\theta, \phi)$$

And substituting $M_l^m \to (-1)^{l+m} M_l^m$ in equation 2.11 gives:

$$f_k^n = \frac{2s^2}{R^2}(-1)^k c_k c_{k+n} \sum_{l=|n|}^{\infty} M_l^{-n}(-1)^{l-n} y_l^{-n}$$

Which is not yet the original light-curve. However, given the fact that for odd values of $l + m$ we have $y_l^m = 0$ (from 2.2 on page 17), we can conclude that the only spherical harmonics that contribute to the signal have even $l - n$, hence $(-1)^{l-n} = 1$, and the expression reduces to the original.
In figure 3.7, one can see that this actually does work. In the upper panel, we take input β to be 0. To show that this does not work for $\beta \neq 0$ (and it shouldn't), the lower panel shows the same reconstructions, but with input $\beta = 40°$.

3.6.2   SYMMETRIES IN THE AXIAL TILT

- For input $\beta = 0°$, all values of α result the same light-curve. This has already been verified in section 3.3.

- For input $\beta = 180°$, the value of α should not influence the reconstructed map, since the spin axis is again perpendicular to the orbital plane. That this is true can be seen in figure 3.8, where the circle map has been recovered with input value $\beta = 180°$ and two different values of α. As can be seen, the recovered maps are the same.

- Secondly, for every spin axis we can find a situation with an anti-parallel spin axis. Replace α by $\pi + \alpha$ and β by $\pi - \beta$, the direction of the spin axis does not change, but the north and south pole are swapped. In the transformation matrix, the extra π that is added to α results in a factor $e^{-i(m+n)\pi} = (-1)^{m+n}$. The substitution in the wigner-d matrix does not give a nice expression, see equation 3.4. But we can look at the results to verify this. Given an input value α and β, a surface map is reconstructed with the original values, and with $\pi + \alpha$ and $\pi - \beta$, see figure 3.9. The two reconstructed maps are clearly the same, the maximum difference between the two maps is 2×10^{-5} and 4×10^{-5} for subfigures a and b respectively. We shall use this later, and refer to it as the **anti-parallel spin axis symmetry**.
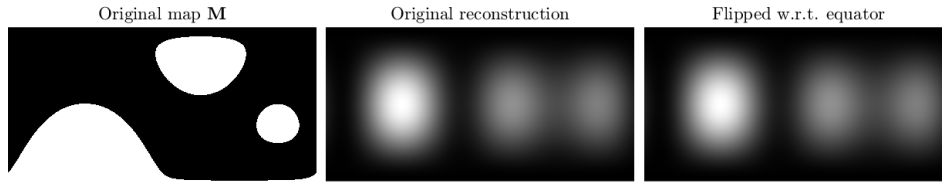
(a) $\alpha_{in} = 0°$ and $\beta_{in} = 0°$
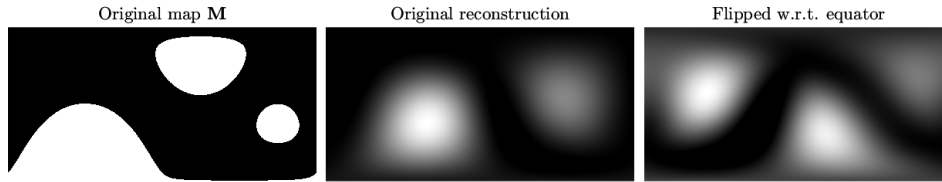
(b) $\alpha_{in} = 0°$ and $\beta_{in} = 40°$

Figure 3.7: *Recovered maps with mirrored input with respect to the equator. Negative albedo is displayed as black.*
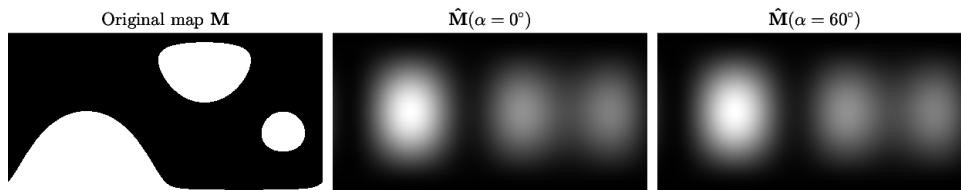
Figure 3.8: *Recovered maps with input $\beta = 180°$ and two different values of α.*
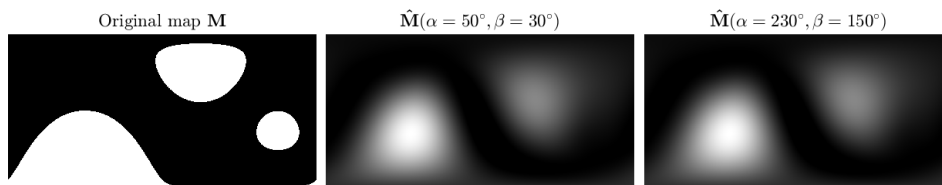
(a) $\alpha_{in} = 50°$ and $\beta_{in} = 30°$
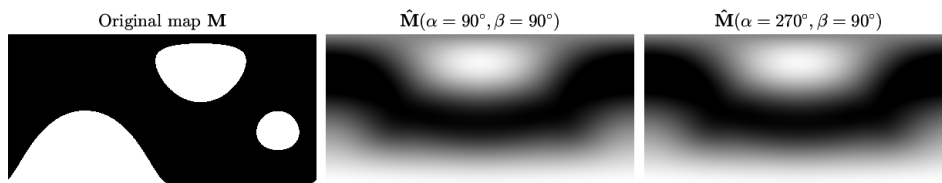
(b) $\alpha_{in} = 90°$ and $\beta_{in} = 90°$

Figure 3.9: *Recovered maps with the same input and two different output values of α and β. The output values have $\alpha_2 = 180° + \alpha_1$, and the $\beta_2 = 180° - \beta_1$. This implies that the spin axes are anti-parallel.*

3.7 The problem of unknown axial tilt

Up till now, we have assumed that we know the angles that determine the axial tilt of the planet. But in practice, the values of α and β are unknown to the observer. It is however not impossible to retrieve these if one uses other techniques, the presence of exomoons could provide information about the axial tilt, but it would further restrain the possible occasions in which one can apply this theory. If we want this reconstruction to be self-contained, we also need estimate α and β from the light-curve. One method would be to minimize the distance $\|\mathbf{f} - A(\alpha, \beta)\mathbf{M}\|$.

$$(\hat{\alpha}, \hat{\beta}) = \underset{(\alpha, \beta) \in [0, 2\pi] \times [0, \pi]}{\arg\min} \|\mathbf{f} - A(\alpha, \beta)\hat{\mathbf{M}}(\alpha, \beta)\| \tag{3.9}$$

Here, $\hat{\mathbf{M}}(\alpha, \beta)$ is the estimated map for given α and β. The $\arg\min$ operator outputs the points on the domain at which the function is minimized see [Wikipedia, 2019]. We have already seen how to find this best estimate in chapter 2, so a solution to this problem can be approximated by laying down a grid of values for α and β and calculate which ones can reproduce a signal which is most similar to $\mathbf{f}$. For this method to work, it is crucial that the range of A is different for different values of α and β. In other words: $\text{Col}(A(\alpha, \beta))$ needs to be unique for every α and β. Surprisingly, it turns out that this is not the case. We will prove this by showing that

$$\text{Col}(A(\alpha, \beta)) = \text{Col}(A(0, 0))$$

for any value of α and β. Therefore, a "best" map can be found for any value of α and β. This property makes the method from equation 3.9 useless.

Edge-on

Let $\mathbf{A}_l^m(\alpha, \beta)$ be a column from the matrix, and choose any value of l, m. We are going to show that $\mathbf{A}_l^m(\alpha, \beta)$ is a linear combination of columns $\mathbf{A}_l^{m'}(0, 0)$. Define an entry of the matrix A as

$$A_{k,l}^{n,m}(\alpha, \beta) := \frac{2s^2}{R^2}(-1)^k c_k c_{k+n} y_l^{-n} d_l^{-n,m}(\beta) e^{-i(m+n)\alpha} \tag{3.10}$$

where k and n indicate that this element is in the row corresponding to f_k^n, and l and m indicate that this element is in the column of M_l^m. Note that, as we have seen in chapter 2:

$$A_{k,l}^{n,-n}(0, 0) = \frac{2s^2}{R^2}(-1)^k c_k c_{k+n} y_l^{-n} \tag{3.11}$$

If we compare these two expressions, we can note that (for $|n| < l$):

$$A_{k,l}^{n,m}(\alpha, \beta) = A_{k,l}^{n,-n}(0, 0) \left[d_l^{-n,m}(\beta) e^{-i(m+n)\alpha} \right]$$

which is independent of the value of k. So the part of $\mathbf{A}_l^m(\alpha, \beta)$ with a fixed value of n is a multiple of $A_{k,l}^{n,-n}(0, 0)$. If we combine this with the fact that $\mathbf{A}_l^{-n}(0, 0)$ is 0 in rows where $n' \neq n$, we get:

$$\mathbf{A}_l^m(\alpha, \beta) = \sum_{n=-l}^{l} \mathbf{A}_l^{-n}(0, 0) \left[d_l^{-n,m}(\beta) e^{-i(n+m)\alpha} \right] \tag{3.12}$$

This proves our claim for edge-on observations.

Face-on

Let $\mathbf{A}_l^m(\alpha, \beta)$ be a column from the matrix, and choose any value of l, m. We are going to show that $\mathbf{A}_l^m(\alpha, \beta)$ is a linear combination of columns $\mathbf{A}_l^{m'}(0, 0)$. As can be seen in equation 3.8, an entry of A is given as:

$$A_{k,l}^{n,m}(\alpha, \beta) = \frac{2s^2}{R^2}(-1)^n c_n \delta_{n,-k} y_l^{-n} d_l^{-nm}(-\beta) \tag{3.13}$$

$$A_{k,l}^{n,-n}(0, 0) = \frac{2s^2}{R^2}(-1)^n c_n \delta_{n,-k} y_l^{-n} \tag{3.14}$$

Such that

$$A_{k,l}^{n,m}(\alpha, \beta) = d_l^{-nm}(-\beta) A_{k,l}^{n,-n}(0,0) \tag{3.15}$$

We can use that every spherical harmonic contributes to only one light-curve coefficient, to conclude that :

$$\mathbf{A}_l^m(\alpha, \beta) = \sum_{n=-l}^{l} \mathbf{A}_l^{-n} d_l^{-nm}(-\beta) \tag{3.16}$$

And that completes the proof for the face-on case.

Consequences

This fact has two consequences. First: the number of independent column's of the matrix is the same for all values of α and β, but depending on the observation (edge/face-on). For the edge-on case we have that:

$$\text{Rank}(A) = 1 + 2 \min\{L, N\} \tag{3.17}$$

and the more complicated expression for the face-on case:

$$\text{rank}(A) = \begin{cases} 1 & \text{if } \min\{L, N, K\} = 0 \\ 3 + 2 \left\lfloor \frac{\min\{L,N,K\}}{2} \right\rfloor & \text{else} \end{cases} \tag{3.18}$$

which is a result from the fact that the c_n coefficients are 0 for all odd n except $n = \pm 1$. The rank is determined by the largest even number that is equal or smaller than the smallest of the three numbers.

The second consequence of our observation is more severe: if we have a light curve, than for all values of α and β we can construct an albedo map which can exactly reproduce this light curve. Thus the observer cannot determine α and β via this method.

CHAPTER 4

FINDING AXIAL TILT

In chapter 3, we found that the introduction of axial tilt to the motion of the planet did not change the column space of the transformation matrix A. This meant that for each tilt orientation a surface map exists that fits perfectly to the light-curve. Hence, there no information of α and β is present in the signal for edge-, and face-on observations. That ends it for the pseudo-inverse. But there are other methods to recover the axial tilt from the light-curve. Yuka Fujii and Hajime Kawahara have already demonstrated that is is possible to retrieve β for face-on orbits in [Fujii and Kawahara, 2011], and for orbits with θ_o ranging from 30° to 60° in [Fujii and Kawahara, 2012]. We shall treat the method that was used there, along with a number of other alternatives to the pseudoinverse method.

4.1   Tikhonov Regularization

When a linear optimization problem is not well posed, extra assumptions often have to be made to find an acceptable solution. This process is called the 'regularization'. It adds a 'penalty' for unwanted behavior of the solution, and combines this with the original formulation of the problem. One of the most common forms of this is Tikhonov Regularization [Hansen, 2010] [1] [2]. This method introduces two new elements: it assumes a prior albedo map, called $\mathbf{M}_p$, ,and has a control parameter λ, which controls the weight of the penalty function. The new problem is to find a set of parameters that minimizes a cost function $C_{\alpha,\beta,\lambda}$:

$$(\hat{\alpha}, \hat{\beta}, \hat{\lambda}) = \underset{(\alpha,\beta,\lambda):\lambda \geq 0}{\arg\min} \; C_{\alpha,\beta,\lambda} \tag{4.1}$$

Where the cost function is given by the sum of our original cost function and the penalty function:

$$C_{\alpha,\beta,\lambda} = \underbrace{\|\mathbf{f} - A(\alpha,\beta)\hat{\mathbf{M}}(\alpha,\beta)\|_2^2}_{\text{original cost function}} + \lambda^2 \underbrace{\|\mathbf{M}_p - \hat{\mathbf{M}}(\alpha,\beta)\|_2^2}_{\text{penalty function}} \tag{4.2}$$

Thus Tikhonov regularization penalizes estimates that lie further from the prior map, so there must be a good reason to suspect this prior map is right. Since we do not know anything about the surface of the exoplanet, except for the fact that we must have that $0 \leq M \leq 1$, we use a homogeneous map as prior. This map should be chosen such that it corresponds to the average value of the light-curve f_0^0.

The solution to the Tikhonov regularization is known. For any triplet (α, β, λ), the map which minimizes $C_{\alpha,\beta,\lambda}$, $\hat{\mathbf{M}}$, is given by:

$$\hat{\mathbf{M}}(\alpha,\beta) = V\Sigma_\lambda U^H(\mathbf{f} - A(\alpha,\beta)\mathbf{M}_p) + \mathbf{M}_p \tag{4.3}$$

Where U and V are the matrices from the singular value decomposition of A, see section 2.4 on page 25: $A = U\Sigma V^H$. Σ_λ is a modified version of Σ, such that:

$$(\Sigma_\lambda)_{ij} = \begin{cases} 0 & i \neq j \\ \frac{\Sigma_{ii}}{\Sigma_{ii}^2 + \lambda^2} = \frac{\sigma_i}{\sigma_i^2 + \lambda^2} & i = j \end{cases} \tag{4.4}$$

---

[1] After Russian mathematician Andrey Tikhonov

[2] This is the method that has been used in [Fujii and Kawahara, 2011] and [Fujii and Kawahara, 2012]

Notice that $\Sigma_0^+ = \Sigma$. We can expand equation 4.3 into a form which is more useful to us:

$$\hat{\mathbf{M}}(\alpha, \beta) = V\Sigma_\lambda U^H(\mathbf{f} - A(\alpha, \beta)\mathbf{M}_p) + \mathbf{M}_p$$
$$= V\Sigma_\lambda U^H \mathbf{f} - V\Sigma_\lambda U^H U\Sigma V^H \mathbf{M}_p + \mathbf{M}_p$$
$$= V\Sigma_\lambda U^H \mathbf{f} + (I - V\Sigma_\lambda \Sigma V^H)\mathbf{M}_p$$

If we plug this back in equation 4.2, we get:

$$C_{\alpha,\beta,\lambda} = \|\mathbf{f} - A(\alpha, \beta)\hat{\mathbf{M}}(\alpha, \beta)\|_2^2 + \lambda^2 \|\mathbf{M}_p - \hat{\mathbf{M}}(\alpha, \beta)\|_2^2$$
$$= \|\mathbf{f} - U\Sigma V^H V\Sigma_\lambda U^H \mathbf{f} - A(I - V\Sigma_\lambda \Sigma V^H)\mathbf{M}_p\|_2^2 + \lambda^2 \|V\Sigma_\lambda U^H \mathbf{f} - V\Sigma_\lambda \Sigma V^H \mathbf{M}_p\|_2^2$$
$$= \|(I - U\Sigma\Sigma_\lambda U^H)\mathbf{f} - A(I - V\Sigma_\lambda \Sigma V^H)\mathbf{M}_p\|_2^2 + \lambda^2 \|V\Sigma_\lambda U^H \mathbf{f} - V\Sigma_\lambda \Sigma V^H \mathbf{M}_p\|_2^2$$

Succes of the Tikhonov regularization

The method however fails to retrieve the values of α and β. See for example figure 4.1, where this method has been applied to a face-on observation of the circle map from appendix B. One can see the cost function for every pair of β and λ on the left. The average cost function for all values of λ, as well as the standard deviation, have been graphed on the right. One can see that the standard daviation is roughly 15 orders of magnitude smaller than the average value. This could be due to a combination of two things:

- The column space of A is constant, such that U does not really change.

- It has been observed that the singular values of A are also constant. The number of singular values is equal to the rank of A (see section 3.7).

Indeed, if the first one changes there is no need for this method, we could obtain the axial tilt with the technique from chapter 3. If the second one changes, Σ_λ changes with it.
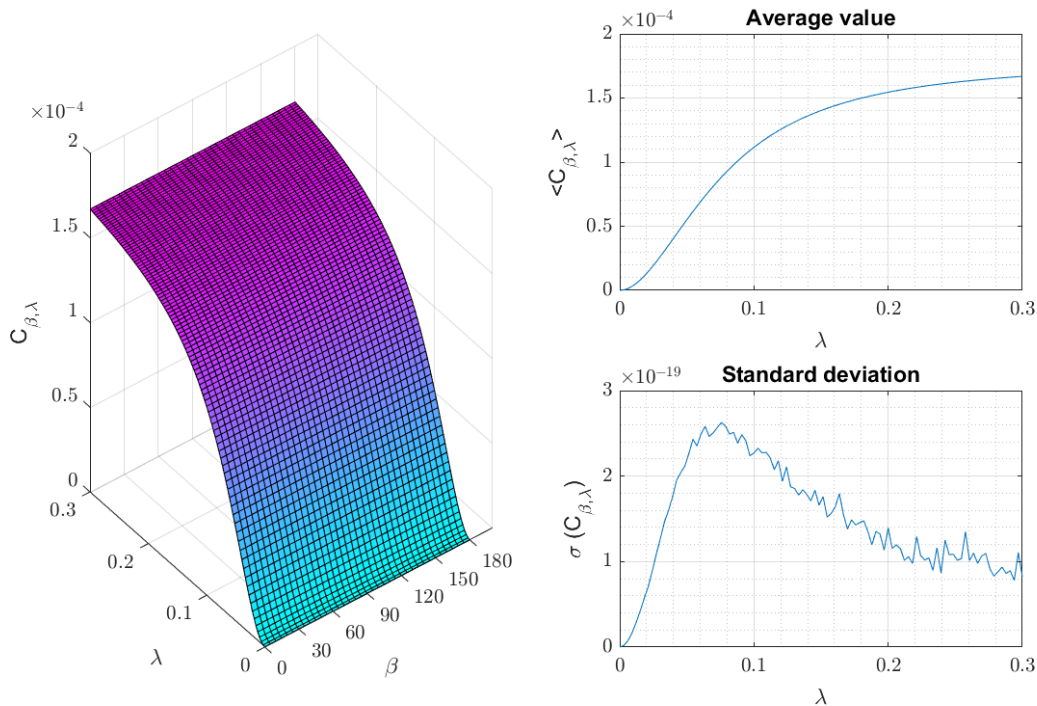
Figure 4.1: *Application of the Tikhonov regularization on a face-on observation of the Circle map (see appendix B), with input $\beta = 30°$. On the left, the cost function $C_{\beta,\lambda}$. On the upper and lower right, the average value and standard deviation in the cost function for constant λ respectively. It can be seen that there is no β dependence in the cost-function. Therefore, β cannot be estimated.*

4.2   Positive albedo map

Since all physical albedo maps must have $0 \leq M \leq 1$, it is undesirable that the recovered map has negative values. However, this has been neglected so far. An example of this can be seen in 2.9 on page 31, where the albedo of the reconstructed map becomes negative on the Pacific Ocean.

There are several ways to use this observation, three are presented here. All rely on the expectation that in the correct values for the axial tilt will give a reconstructed map that comes closest to being physical. They have a similar input as the least squares, and Tikhonov regularization: for every value of the axial tilt, we compute a function that is an indicator for the "amount of positive albedo", referred to as the function $R(\alpha, \beta)$, the definition of R depends on the used method. The output axial tilt is the one that maximizes this specific function R, see [Wikipedia, 2019] for the arg max function:

$$(\hat{\alpha}, \hat{\beta}) = \underset{(\alpha, \beta)}{\arg \max} \, R(\alpha, \beta) \tag{4.5}$$

All of these methods have been tested with as input: the circle map (from appendix B), $\alpha = 50°$ (so edge-on observation), and $\beta = 30°$. The results are plotted in the left panels of figure 4.2.

To get an understanding of what is really a contour generated by the method, and what is a numerical error, we use the anti-parallel spin axis symmetry from section 3.6. In this section, and specifically in figure 3.9, we have shown that with the same input obliquity as used over here, two output axial tilts (α, β), and $(\pi + \alpha, \pi - \beta)$ result in the same surface map, hence they should return the same output value for the methods presented over here. Thus in the right panel, the difference of the output value for these two axial tilts is plotted:

$$R(\alpha, \beta) - R(\pi + \alpha, \pi - \beta) \tag{4.6}$$

for $(\alpha, \beta) \in [0, 180°] \times [0, 90°]$. The extreme values of this give an indication for the size of the numerical error.

A method based on the 2-norm

Since we now have a preference for positive albedo, we could try to maximize the constant term of the map, and use:

$$R(\alpha, \beta) = \frac{\hat{M}_0^0(\alpha, \beta)^2}{\|\hat{\mathbf{M}}(\alpha, \beta)\|_2^2} = \frac{M_0^0(\alpha, \beta)^2}{\iint |\hat{M}(\theta, \phi)|^2 d^2 S} \tag{4.7}$$

in equation 4.5. The second equality holds because of the Parseval identity. Working out the denominator gives:

$$\begin{aligned}
\|\hat{\mathbf{M}}\|_2^2 &= \|A^+ \mathbf{f}\|_2^2 \\
&= (A^+ \mathbf{f})^H A^+ \mathbf{f} \\
&= \mathbf{f}^H (A^+)^H A^+ \mathbf{f} \\
&= \mathbf{f}^H (V \Sigma^+ U^H)^H V \Sigma^+ U^H \mathbf{f} \\
&= \mathbf{f}^H U (\Sigma^+)^H \Sigma^+ U^H \mathbf{f}
\end{aligned}$$

It has already been observed that the singular values of A, as well as its column space, do not depend on the axial tilt of the planet. Therefore, $\|\hat{\mathbf{M}}\|_2^2$ does not depend on the axial tilt, and R reduces to:

$$R(\alpha, \beta) == \equiv M_0^0(\alpha, \beta)^2$$

However, the influence of M_0^0 on the light-curve does not depend on the axial tilt (tilting the homogeneous map gives the same map). Therefore, R is not a function of the axial tilt, and this version of the method cannot be used to determine α and β. This is also verified in figure 4.2a; it can be seen that the largest difference is in the order of 10^{-13}.

A method based on the infinity norm

Our preference for positive albedo can also be used by looking at the ratio between the maximum and minimum value of the map:

$$R(\alpha, \beta) = \frac{\max \hat{M}(\alpha, \beta)}{|\min \hat{M}(\alpha, \beta)|} \tag{4.8}$$

If this method is used, we choose the map that has the smallest "spikes" with negative albedo. This seems a good option, but it has its downsides. It takes only the outliers into account. Suppose that we have two surface maps: M_1, which is largely positive, but has one big negative spike, and M_2, which has the same maximum as M_1, but is constantly negative almost everywhere. This method has no preference, while M_1 is better map from a physical point of view.

In figure 4.2b, we can see that the outcome of this method is also not acceptable. On the right panel, one can see that the maximum value of $R(\alpha, \beta) - R(\pi + \alpha, \pi - \beta)$ is around ± 0.0001, giving an approximation for the numerical error. On the left panel, one can see that the maximum difference in R is 0.0002. Therefore, all of the visible contrast is possibly due to numerical errors.

A method based on the 1-norm

A third alternative, which is even more refined, would be to choose the map with the smallest total amount of negative albedo according to the 1-norm:

$$R(\alpha, \beta) = \frac{\iint |\hat{M}^+(\theta, \phi)| d^2 S}{\iint |\hat{M}(\theta, \phi)| d^2 S} = \frac{\|M^+(\alpha, \beta)\|_1}{\|M(\alpha, \beta)\|_1} \tag{4.9}$$

but, just as with equation 4.8, we cannot simplify this expression. We can only rely on our intuition when we say that this might work. The results of this method are plotted in figure 4.2c. In the right panel, we can see that the order of magnitude of the numerical error is ± 0.0001. In the left panel we see that the largest contrast is 0.0004. Thus the contrast is of the same order of magnitude as the numerical error, and the axial tilt can also not be recovered with this method[3].

---

[3]Furthermore, there is no extreme value at the input axial tilt.
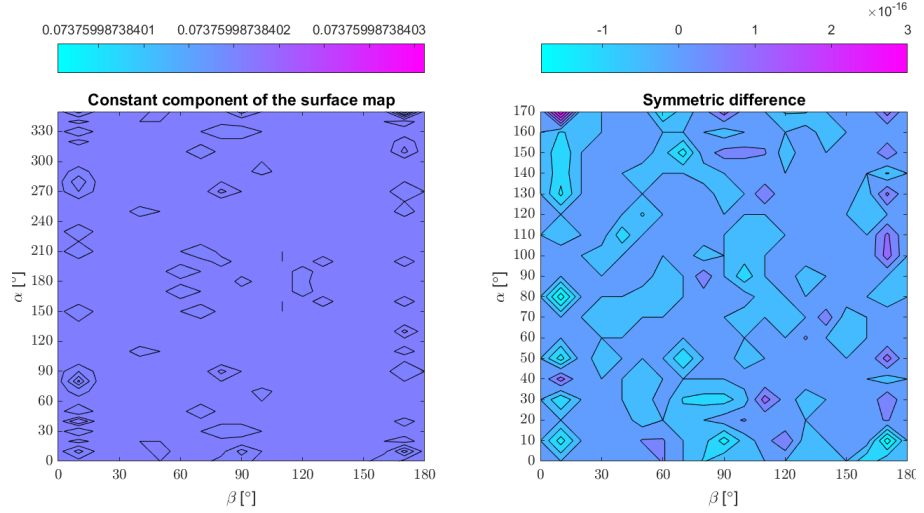
(a) *Results with equation 4.7*
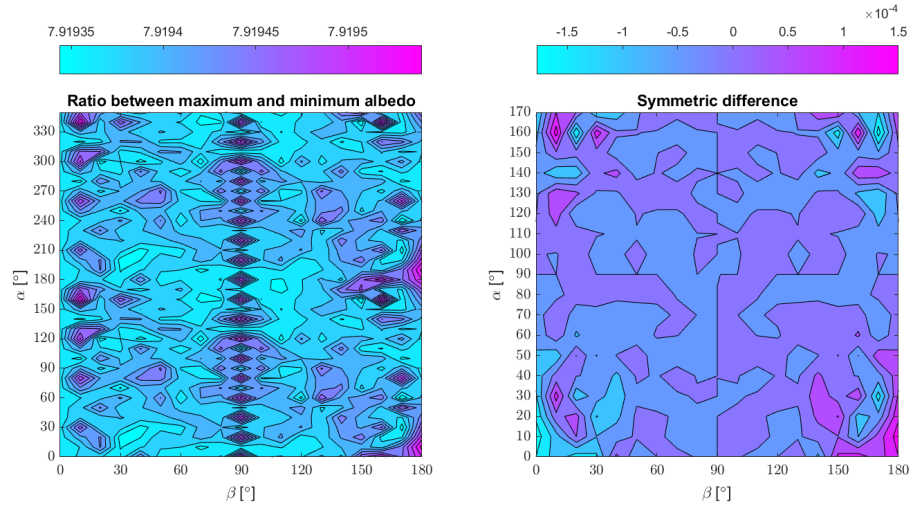
(b) *Results with equation 4.8*
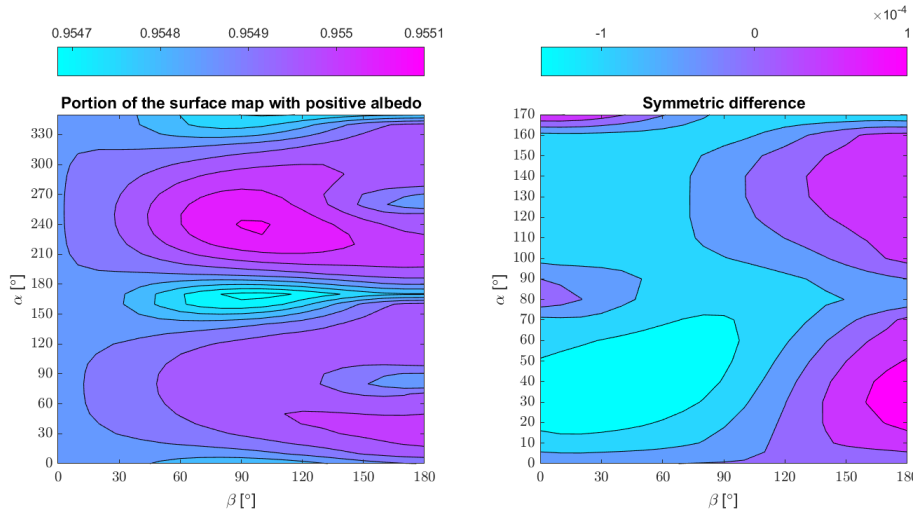
(c) *Results with equation 4.9*

Figure 4.2: *Estimation of the axial tilt with the maximization method from section 4.2. Input is the circle map from appendix B, $(\alpha, \beta) = (50°, 30°)$, edge-on observed. On the left panels, one can see the values R from equations 4.8, 4.7, and 4.9 (top to bottom). On the right, the difference of R for anti-parallel spin axis: $R(\alpha, \beta) - R(\pi + \alpha, \pi - \beta)$.*

CHAPTER 5

DISCUSSION AND CONCLUSION

The aim of this research was to develop an alternative approach to spin-orbit tomography, looking at the relation between the Fourier components of the reflective light-curve and the albedo map coefficients in the basis of spherical harmonics. In the first chapter, we discussed the properties of the reflective light-curve, and derived a general equation for the light-curve under the assumption of Lambertian reflection. In chapter 2 and sections 3.1 through 3.6, we worked out this equation for edge-on and face-on observations, and discussed how a surface map can be reconstructed if we know the axial tilt. In section 3.7 and chapter 4, we discussed possible methods to reconstruct the surface map if the tilt is unknown.

Recovering the albedo map with known axial tilt (chapters 2 and 3)

In chapters 2 and 3, we have seen that we can relate the reflective light-curve and the albedo map of an exoplanet by decomposing them in a basis of complex exponentials and spherical harmonics respectively:

$$M(\theta_p, \phi_p) = \sum_{l=0}^{\infty} \sum_{m=-l}^{l} M_l^m Y_l^m(\theta_p, \phi_p) \qquad \approx \sum_{l=0}^{L} \sum_{m=-l}^{l} M_l^m Y_l^m(\theta_p, \phi_p)$$

$$f(\phi, \Phi) = \sum_{k=-\infty}^{\infty} \sum_{n=-\infty}^{\infty} f_k^n e^{i(k\phi + n\Phi)} \qquad \approx \sum_{k=-K}^{K} \sum_{n=-N}^{N} f_k^n e^{i(k\phi + n\Phi)}$$

The approximations are necessary for practical reasons and are determined by the following three coefficients:

1. L, which determines the number of spherical harmonics are taken in account.

2. K, which determines the amount of detail of which the annual rotation can be observed.

3. N, which determines the amount of detail of which the diurnal rotation can be observed.

We calculated the linear transformation $\mathcal{A} : \mathbb{R}^{\infty} \to \mathbb{R}^{\infty}$ that expresses the Fourier coefficients of the reflective light-curve, f_k^n as a function of the albedo surface map coefficients M_l^m, and axial tilt (α, β). We denote this function as $\mathbf{f} = \mathcal{A}(\alpha, \beta, \mathbf{M})$. If only a finite number of coefficients are taken into account, as in the approximations mentioned above, this transformation reduces to the matrix $A(\alpha, \beta) : \mathbb{R}^{(L+1)^2} \to \mathbb{R}^{(2N+1)(2K+1)}$, and matrix-vector equation $\mathbf{f} = A(\alpha, \beta)\mathbf{M}$. Expressions for these transformations can be found in equations 3.6 and 3.8 for edge-on and face-on observations respectively.

   With these expressions, we can compute the best estimate map $\hat{\mathbf{M}}$ that generated the light-curve $\mathbf{f}$ if the axial tilt (α, β) and observation situation are known. This can be done by projecting $\mathbf{f}$ onto $\mathrm{Col}(A(\alpha, \beta))$ by $\hat{\mathbf{M}} = A^+(\alpha, \beta)\mathbf{f}$. This has been done for the surface map of the Earth in chapter 3 and for a variety of other maps in appendices B and C. A curious observation is that for all of the reconstructed maps with zero tilt and edge-on observation, the map appears to be separable: $M(\theta_p, \phi_p) =$

$m(\phi_p)\sin^2(\theta_p)$. The only spherical harmonics that can be written in this form are Y_2^{-2} and Y_2^2, but these are not the only functions that contribute to $\hat{\mathbf{M}}$.

We have deduced that the rank of A is determined by the three integers N, K, and L. It is given by

$$\text{rank}(A) = 1 + 2\min\{N, L\} \tag{5.1}$$

for edge-on observations, and

$$\text{rank}(A) = \begin{cases} 1 & \text{if } \min\{L, N, K\} = 0 \\ 3 + 2\left\lfloor \frac{\min\{L,N,K\}}{2} \right\rfloor & \text{else} \end{cases} \tag{5.2}$$

for face-on observations, and has been found to be independent of the value of the axial tilt.

The null-space of A

There are surface maps that have no contribution to the reflective light-curve at all, as can be seen by taking a look at the null-space of A. Most notably, for edge on observations with zero axial tilt, all maps of the form Y_l^0, with $l > 2$ are in the null space of A. These are the functions that can be written as $Y_l^0(\theta_p, \phi_p) \sim P_l^0(\arccos(\theta_p))$, the functions with constant value over the longitude. Since planets like Jupiter are composed of these bands, see figure 5.1, the albedo map of these planets will be hard to reconstruct. In appendices B and C, it can be seen that there the reconstruction of Jupiters albedo map has never been successful [1]. One can see what happens if an element of the null space is added to the recovered map in figure 5.2.
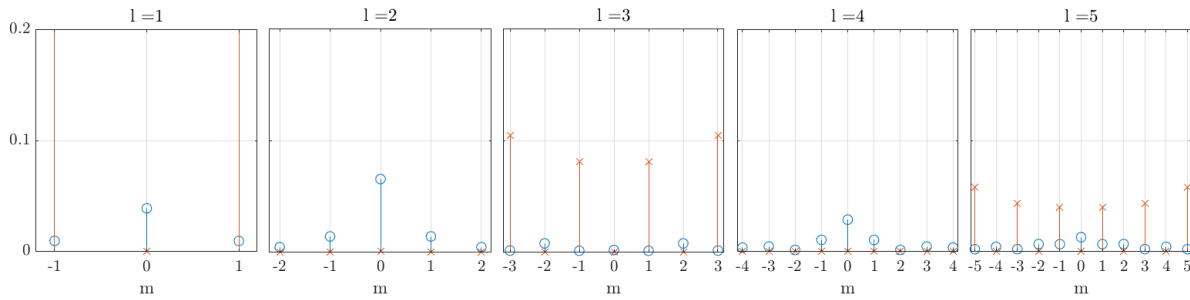
Figure 5.1: *The map coefficients from Jupiter 'o', and the map of unit-Φ from the appendix. Notice the dominance of the coefficients with $m = 0$ for Jupiter, and the coefficients with large m for Unit-Φ.*
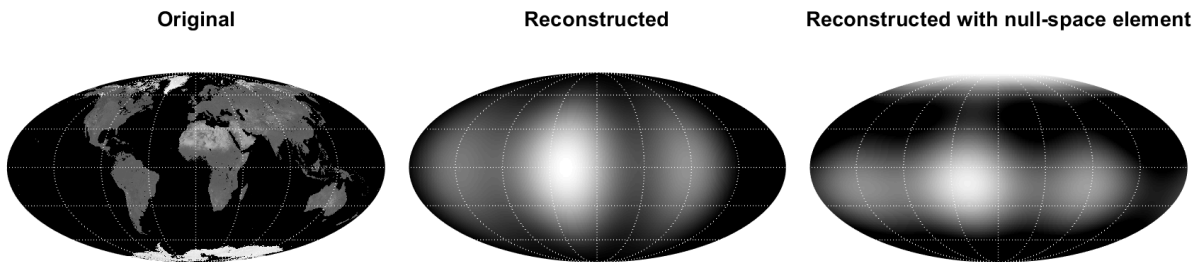
Figure 5.2: *Reconstructed map modified with null space*

Symmetries (section 3.6)

We have checked that the transformation A behaves as it is expected to. It has been verified that for edge-on observations with zero tilt, the map can be mirrored with respect to the equator without affecting the light-curve, and that we can shift the longitudinal zero of the map, and recover the same map.

---

[1]Furthermore, the obliquity of Jupiter is only $3°$, such that its bands can never be observed, at least not with this method.

Most notably, we have observed that there is anti-parallel spin axis symmetry in figure 3.9. In the recovery of the map, it is irrelevant whether we choose the axial tilt such that the north pole has positive z component, or the south pole has; The recovered map is the same.

Recovering the albedo map with unknown axial tilt (section 3.7 and chapter 4)

In the first chapters we had seen how surface maps can be reconstructed if we know what the value of the axial tilt was. In chapter 4, we let this go, since in reality, the axial tilt is unknown to the observer and needs to be estimated from the light-curve. A number of possible methods have been discussed. We speak of an input axial tilt as the axial tilt that generates the light-curve, the actual property of the system. Then we take the light-curve, and apply some (to be discussed) operation to it while varying the output axial tilt. The estimated axial tilt is the output axial tilt that gives the most desired outcome.

We started with the most straightforward manner of determining the axial tilt. If a light-curve $\mathbf{f}$ is generated by an exoplanet with input tilt (α_i, β_i), an estimated map where the output value of the axial tilt is equal to the input will be able to generate the same curve. Other output axial tilts can therefore only generate a light-curve that looks less like $\mathbf{f}$. In other words, if the column space of A changes, we can pick the output axial tilt.

1. Calculate the best estimate map for any value of the output axial tilt (α, β) by projecting $\mathbf{f}$ on $\text{Col}(A(\alpha, \beta))$, such that $\hat{\mathbf{M}}(\alpha, \beta) = A^+(\alpha, \beta)\mathbf{f}$.

2. Calculate the distance between the light-curve from the estimated map and the actual light-curve: $\|\mathbf{f} - A(\alpha, \beta)\hat{\mathbf{M}}(\alpha, \beta)\|_2^2$.

3. Take the estimate values of α and β, $\hat{\alpha}$ and $\hat{\beta}$ respectively, as

$$(\hat{\alpha}, \hat{\beta}) = \underset{(\alpha,\beta)\in[0,2\pi]\times[0,\pi]}{\arg\min} \|\mathbf{f} - A(\alpha, \beta)\hat{\mathbf{M}}(\alpha, \beta)\|$$

However, it was found in 3.7 on page 47 that $\text{Col}(A(\alpha, \beta))$ was independent of the value of the axial tilt for both edge-on and face-on observations. This means that the output value of step 2 is a constant, and we do not find $(\hat{\alpha}, \hat{\beta})$ in step 3.

In chapter 4, we looked at two alternative methods that could possibly retrieve the axial tilt along with the albedo map. These methods are:

- Tikhonov regularization

- Positive albedo maximization

Tikhonov regularization is the method that as been used in (among others) [Fujii and Kawahara, 2012]. The method starts with the original objective, the minimization of $\|\mathbf{f} - A\hat{\mathbf{M}}\|_2$, and introduces a prior map and penalizes estimates that lie far from this prior. This penalty function makes its way in the new solution by modifying the singular values of $A(\alpha, \beta)$, thus using a property of A that we had not yet exploited. However, we found that not only $\text{Col}(A)$, but also the singular values are also independent of the axial tilt. This meant that Tikhonov regularization could not provide a solution. This is in contrast to what had been found in [Fujii and Kawahara, 2011], where the axial tilt has been estimated for face-on orbits using Tikhonov regularization. In this paper, however, the surface map was divided in pixels, and the reflective light-curve was analyzed in the time domain. This results in matrix coefficients that can only be computed numerically. This might have changed the properties of A, i.e. $\text{Col}(A)$ or the singular values of A might have become a function of the axial tilt.

But irrespective of the reason why, Tikhonov regularization is ineffective with this variant of spin-orbit tomography. The second method that had been looked at in chapter 4 involved the maximization of the positive albedo. Though unphysical, it has turned out that in many of the sample cases that have been considered in this report, the reconstructed map had areas with negative albedo. And though this is undesirable (though not uncommon, see [Fujii and Kawahara, 2012]), it could be used to reconstruct the axial tilt. It seems reasonable that the reconstruction, when using the same output as input axial tilt, gives a surface map that comes closest (or at least close to) a surface that is physical, whereas an output axial tilt that is way different from the input might give a map that is unphysical. So this method looks at the reconstructed map of all axial tilts, and chooses the one that has the highest level of "physicality".

We discussed three methods that quantify the "physicality" of a surface map. These methods were, in the same order as treated in chapter 4, based on the 2-, ∞-, and 1-norm of the map. The first method, the maximization of the constant term, did not qualify at all; it was shown that is it mathematically impossible to differentiate between different values of the axial tilt with this method. The second method, the maximization of the ratio between the most positive and most negative albedo, could not be worked out in a similar way as the first method could. So, it had to be tested. In figure 4.2b the results were shown, and it could be concluded that this method could not differentiate between different axial tilts. The third method, the maximization of the ratio between the surface integral over the positive albedo and the surface integral over the absolute value of the albedo, generated similar results, as can be seen in figure 4.2c.

This meant that we have not found a method to retrieve the albedo map if the axial tilt is unknown to the (face-on or edge-on) observer.

Further research

Further research into the subject may be conducted in three areas.

When we reconstructed the map, we have projected the light-curve onto $\text{Col}(A)$. However, as has been shown in chapter 2 and briefly discussed earlier in this chapter, we can add any vectors from the null-space to the reconstructed map and maintain the original signal. This might be used to create a surface map that has no negative albedo values, as has been the case in almost all of the reconstructed maps from this report.

The fact that we have not found any method to retrieve the axial tilt from the reflected light-curve does of course not imply that it does not exist. Other methods could exist that not only use the mathematical description of the problem but also the physical context, as we have done when we looked at the negative albedo. One could use that the albedo is not only bound from below, but also from above (limited by 1).

The contrast with the results that we have found in this report and the ones that have been published by Fujii and Kawahara is surprising and certainly notable. Further research might be conducted in the difference between the two methods, why the one seems to generate good results and the other one does not.

Bibliography

[Beekman, 2016] Beekman, M. (2016). Reflective light-curves of ellipsoidally-shaped outer solar-system objects and exoplanets. Bachelor thesis, Delft University of Technology.

[Borucki et al., 2009] Borucki, W., Koch, D., Jenkins, J., Sesselov, D., Gilliand, R., Batalha, N., Latham, D., Caldwell, D. adn Basri, G., Brown, T., Christensen-Dalsgaard, J., Cochran, W., DeVore, E., Dunhamm, E. adn Dupree, A., Gautier, T., Geary, J., Gould, A., Howell, S., Kjeldsen, H., Lissauer, J., Meibom, S., Morrison, D., and Tarter, J. (2009). Kepler's optical phase curve of the exoplanet hat-p-7b. *Science*, 325.

[Cowan, 2014] Cowan, N. (2014). The exoplanet opportunity: Top-down planetary science. *Eos, Transactions, American Geophysical Union*, 95.

[Cowan and Agol, 2008] Cowan, N. and Agol, E. (2008). Inverting phase functions to map exoplanets. *Nature*, 434.

[Cowan and Fujii, 2017] Cowan, N. and Fujii, Y. (2017). Mapping exoplanets. *The Springer Handbook of Exoplanets.*

[Depriester, 2017] Depriester, D. (2017). Représentation des angles d'euler avec tikz. http://blog.dorian-depriester.fr/latex/tikz/representation-des-angles-deuler-avec-tikz. Last accessed October 24, 2018.

[Fujii and Kawahara, 2010] Fujii, Y. and Kawahara, H. (2010). Global mapping of earth-like exoplanets from scattered light curves. *The Astrophysical Journal*, 720.

[Fujii and Kawahara, 2011] Fujii, Y. and Kawahara, H. (2011). Mapping clouds and terrain of earth-like planets from photometric variability: demonstration with planets in face-on orbits. *The Astrophysical Journal Letters*, 739(2).

[Fujii and Kawahara, 2012] Fujii, Y. and Kawahara, H. (2012). Mapping earth analogs from photometric variability: Spin-orbit tomography for planets in inclined orbits. *The Astrophysical Journal*, 755(2).

[Gimbutas and Greengard, 2009] Gimbutas, Z. and Greengard, L. (2009). A fast and stable method for rotating spherical harmonic expansions. *Journal of Computational Physics*, 228:5621–5627.

[Goldstein, 1950] Goldstein, H. (1950). *Classical Mechanics.* Addison Wesley, South-Carolina.

[Griffiths, 2004] Griffiths, D. (2004). *Introduction to Quantum Mechanics.* Cambridge University Press, Cambridge.

[Hansen, 2010] Hansen, P. C. (2010). *Discrete Inverse Problems: Insight and Algorithms.* Society for Industrial and Applied Mathematics, Philadelphia, PA, USA.

[Hecht, 2017] Hecht, E. (2017). *Optics.* Pearson Higher Education Inc, Essex.

[Hoffmann, 2018] Hoffmann, S. E. (2018). Uniform analytic approximation of wigner rotation matrices. *Journal of Mathematical Physics*, 59.

[Knutson et al., 2007] Knutson, H., Charbonneau, D., Allen, L., Fortney, J., Agol, E., Cowan, N., Showman, A., Cooper, C., and Megeath, S. (2007). A map of the day–night contrast of the extrasolar planet hd 189733b. *Nature*, 447.

[Koppal, 2014] Koppal, S. J. (2014). *Lambertian Reflectance*, pages 441–443. Springer US, Boston, MA.

[Mol, 2018] Mol, M. (2018). Eclipses by exomoons. Bachelor thesis, Delft University of Technology.

[NASA, 2006] NASA (2006). Cassini's best maps of jupiter (cylindrical map). https://solarsystem.nasa.gov/resources/13050/cassinis-best-maps-of-jupiter-cylindrical-map/. Last accessed April 23, 2019.

[NASA, 2017a] NASA (2017a). Albedo (1 month). https://neo.sci.gsfc.nasa.gov/view.php?datasetId=MCD43C3_M_BSA. Last accessed August 13, 2018.

[NASA, 2017b] NASA (2017b). Want to see the surface of another earth? use our sun. https://exoplanets.nasa.gov/news/1461/want-to-see-the-surface-of-another-earth-use-our-sun/. Last accessed May 30, 2019.

[NASA, 2018] NASA (2018). Exoplanet historic timeline. https://exoplanets.nasa.gov/alien-worlds/historic-timeline. Last accessed March 31, 2019.

[of New Hampshire, 2014] of New Hampshire, U. (2014). Cosmic ray telescope for the effects of radiation. http://crater-web.sr.unh.edu/albedomap.html. Last accessed April 9, 2019.

[Oppenheim, 2014] Oppenheim, A. V. (2014). *Signals and Systems*. Pearson Higher Education Inc., Essex.

[Russel, 1905] Russel, H. (1905). On the light variations of asteroids and satellites. *The Astrophysical Journal*, 24.

[Russel, 1916] Russel, H. (1916). On the albedo of planets and their satellites. *The Astrophysical Journal*, 43.

[Society, 2018] Society, T. P. (2018). Global surveyor tes albedo map of mars. http://www.planetary.org/multimedia/space-images/mars/mars-global-surveyor-tes-albedo-map-mars.html. Last accessed April 9, 2019.

[Strang, 2006] Strang, G. (2006). *Linear Algebra*. Brooks/Cole.

[Tinetti et al., 2012] Tinetti, G., Beaulieu, J. P., Henning, T., Meyer, M., Micela, G., Ribas, I., Stam, D., Swain, M., Krause, O., Ollivier, M., Pace, E., Swinyard, B., Aylward, A., van Boekel, R., Coradini, A., Encrenaz, T., Snellen, I., Zapatero-Osorio, M. R., Bouwman, J., Cho, J. Y.-K., Coudé de Foresto, V., Guillot, T., Lopez-Morales, M., Mueller-Wodarg, I., Palle, E., Selsis, F., Sozzetti, A., Ade, P. A. R., Achilleos, N., Adriani, A., Agnor, C. B., Afonso, C., Allende Prieto, C., Bakos, G., Barber, R. J., Barlow, M., Batista, V., Bernath, P., Bézard, B., Bordé, P., Brown, L. R., Cassan, A., Cavarroc, C., Ciaravella, A., Cockell, C., Coustenis, A., Danielski, C., Decin, L., De Kok, R., Demangeon, O., Deroo, P., Doel, P., Drossart, P., Fletcher, L. N., Focardi, M., Forget, F., Fossey, S., Fouqué, P., Frith, J., Galand, M., Gaulme, P., González Hernández, J. I., Grasset, O., Grassi, D., Grenfell, J. L., Griffin, M. J., Griffith, C. A., Grözinger, U., Guedel, M., Guio, P., Hainaut, O., Hargreaves, R., Hauschildt, P. H., Heng, K., Heyrovsky, D., Hueso, R., Irwin, P., Kaltenegger, L., Kervella, P., Kipping, D., Koskinen, T. T., Kovács, G., La Barbera, A., Lammer, H., Lellouch, E., Leto, G., Lopez Morales, M., Lopez Valverde, M. A., Lopez-Puertas, M., Lovis, C., Maggio, A., Maillard, J. P., Maldonado Prado, J., Marquette, J. B., Martin-Torres, F. J., Maxted, P., Miller, S., Molinari, S., Montes, D., Moro-Martin, A., Moses, J. I., Mousis, O., Nguyen Tuong, N., Nelson, R., Orton, G. S., Pantin, E., Pascale, E., Pezzuto, S., Pinfield, D., Poretti, E., Prinja, R., Prisinzano, L., Rees, J. M., Reiners, A., Samuel, B., Sánchez-Lavega, A., Forcada, J. S., Sasselov, D., Savini, G., Sicardy, B., Smith, A., Stixrude, L., Strazzulla, G., Tennyson, J., Tessenyi, M., Vasisht, G., Vinatier, S., Viti, S., Waldmann, I., White, G. J., Widemann, T., Wordsworth, R., Yelle, R., Yung, Y., and Yurchenko, S. N. (2012). EChO. Exoplanet characterisation observatory. *Experimental Astronomy*, 34:311–353.

[Visser and van der Bult, 2015] Visser, P. and van der Bult, F. (2015). Fourier spectra from exoplanets with polar caps and ocean glint. *Astronomy and Astrophysics*, 579.

[Wigner, 1927] Wigner, E. (1927). *Group Theory and its Application to the Quantum Mechanics of Atomic Spectra*. Academic Press, New-York.

[Wikipedia, 2018a] Wikipedia (2018a). Euler angles. https://en.wikipedia.org/wiki/Euler_angles. Last accessed October 24, 2018.

[Wikipedia, 2018b] Wikipedia (2018b). Spherical harmonics. https://en.wikipedia.org/wiki/Spherical_harmonics. Last accessed August 14, 2018.

[Wikipedia, 2019] Wikipedia (2019). Arg max. https://en.wikipedia.org/wiki/Arg_max. Last accessed May 13, 2019.

Appendices

Appendix A

Some properties of the spherical harmonics

The spherical harmonics are the solutions of the Laplace equation $\nabla^2 f = 0$ on a sphere. After separation of variables, one obtains the equations

$$f(r, \theta, \phi) = R(r)Y(\theta, \phi) = R(r)\Theta(\theta)\Phi(\phi) \tag{A.1}$$

$$-m^2 = \frac{1}{\Phi}\frac{d^2\Phi}{d\phi^2} \tag{A.2}$$

$$m^2 = -l(l+1)\sin^2(\theta) + \frac{\sin(\theta)}{\Theta}\frac{d}{d\theta}\left(\sin(\theta)\frac{d\Theta}{d\theta}\right) \tag{A.3}$$

the solutions of equations A.2 and A.3 are $e^{im\phi}$ and $P_l^m(\arccos(\theta))$ respectively. The spherical harmonic Y_l^m is given by the product of Θ and Φ: $Y_l^m(\theta, \phi) \sim P_l^m(\arccos(\theta))e^{im\phi}$, where they are normalized such that they form a orthonormal basis on the Hilbert space of square integrable functions:

$$Y_l^m(\theta, \phi) = \mathcal{N}_l^m P_l^m(\arccos(\theta))e^{im\phi} \tag{A.4}$$

$$\mathcal{N}_l^m = \sqrt{\frac{(2l+1)}{4\pi}\frac{(l-m)!}{(l+m)!}} \tag{A.5}$$

$$\iint\limits_{\text{sphere}} Y_l^m Y_{l'}^{m'} d^2 S = \delta_{l,l'}\delta_{m,m'} \tag{A.6}$$

$$M(\theta, \phi) = \sum_{l,m} M_l^m Y_l^m(\theta, \phi) \tag{A.7}$$

Symmetry

$$Y_l^{-m}(\theta, \phi) = (-1)^m \overline{Y_l^m(\theta, \phi)} \tag{A.8}$$

$$Y_l^m(\theta, \phi + \pi) = (-1)^m Y_l^m(\theta, \phi) \tag{A.9}$$

$$Y_l^m(\pi - \theta, \phi) = (-1)^{l+m} Y_l^m(\theta, \phi) \tag{A.10}$$
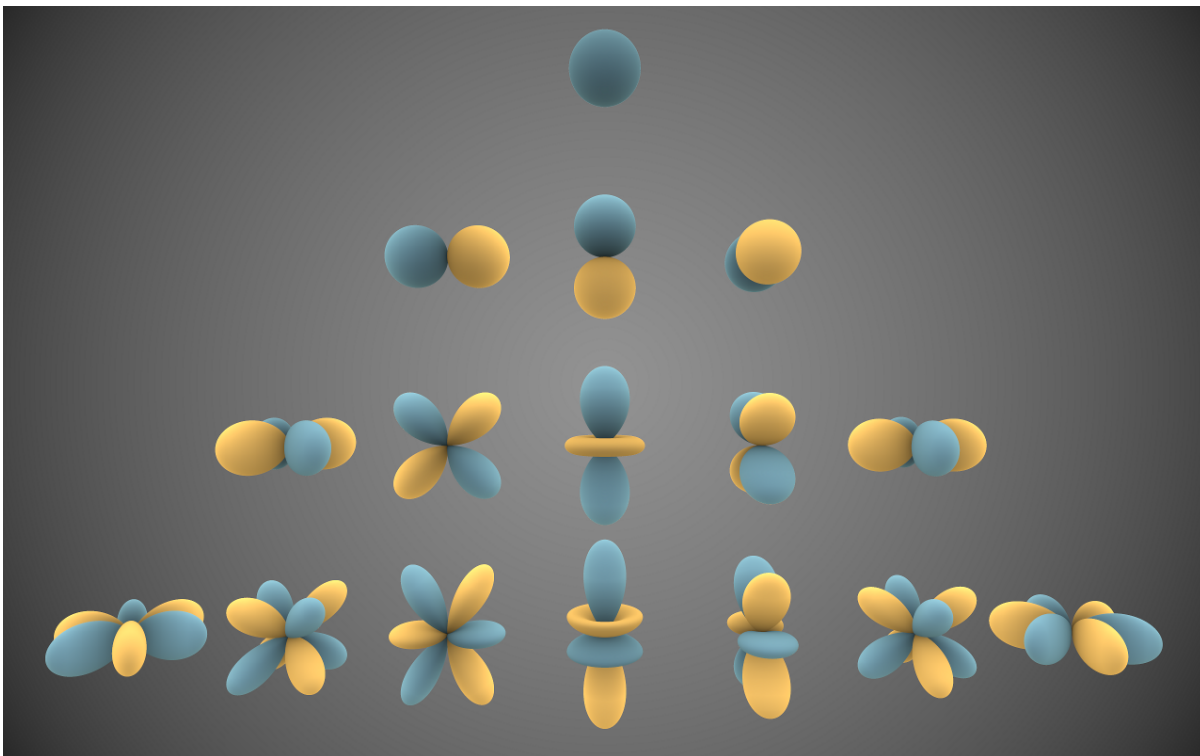
Figure A.1: *Visual representations of the first few real spherical harmonics. Blue portions represent regions where the function is positive, and yellow portions represent where it is negative. The distance of the surface from the origin indicates the value of in angular direction. Source : [Wikipedia, 2018b]*

.

Appendix B

Additional recovered maps for edge-on observation

In chapter 3, we recovered the map of the Earth for known values of β and α. Due to the way the continents are aligned, it is not always visible whether or not the result is acceptable, so other maps have also been used:

- An albedo map of the moon from [of New Hampshire, 2014] has been used. This map has been plotted onto a sphere in figure B.1d, and the result of the edge-on reconstruction can be found in figure B.5.

- An albedo map of the moon from [Society, 2018] has been used. This map has been plotted onto a sphere in figure B.1e, and the result of the edge-on reconstruction can be found in figure B.6.

- An albedo map of the moon from [NASA, 2006] has been used. This map has been plotted onto a sphere in figure B.1f, and the result of the edge-on reconstruction can be found in figure B.7.

- In addition to these three real objects, three artificial planets have been created. The first of these 'planets' is Unit-Θ. This map is given by:

$$M_\Theta(\theta, \phi) = \mathbb{1}_{[0,\pi/2]}(\theta)$$

  This map is displayed in figure B.1a, and the results of the reconstruction can be found in figure B.2.

- The second artificial planets is Unit-Φ. This map is given by:

$$M_\Phi(\theta, \phi) = \mathbb{1}_{[\pi,2\pi]}(\phi)$$

  This map is displayed in figure B.1b, and the results of the reconstruction can be found in figure B.3.

- The last artificial planet is the circle map. This map consists of three circles with albedo 1, put onto a sphere. This map is displayed in figure B.1c, and the results of the reconstruction can be found in figure B.4.

(a) *The planet Unit-Θ*

(b) *The planet Unit-Φ*

(c) *The Circle planet*

(d) *The Moon*

(e) *The planet Mars*

(f) *The planet Jupiter*
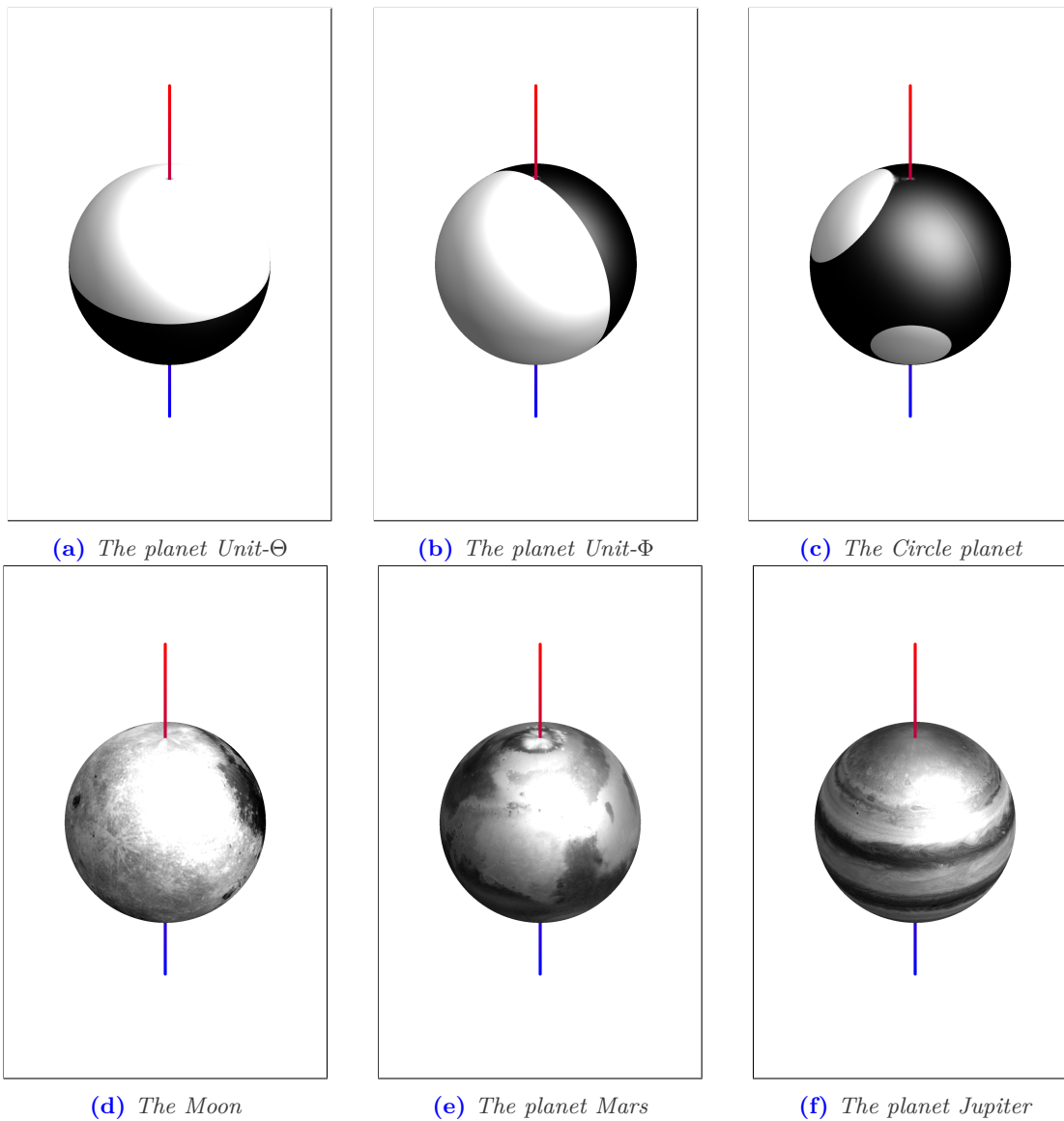
Figure B.1: *Maps of our imaginary planets. The red line indicates the position of the north pole, the blue line indicates the location of the south pole.*

(a) $\alpha = 0°$

(b) $\alpha = 90°$

(c) $\alpha = 180°$
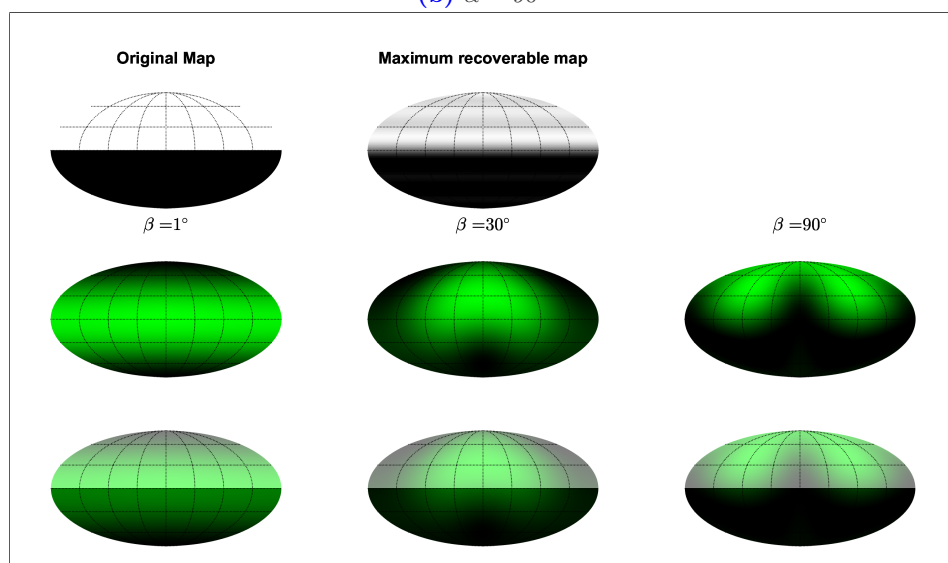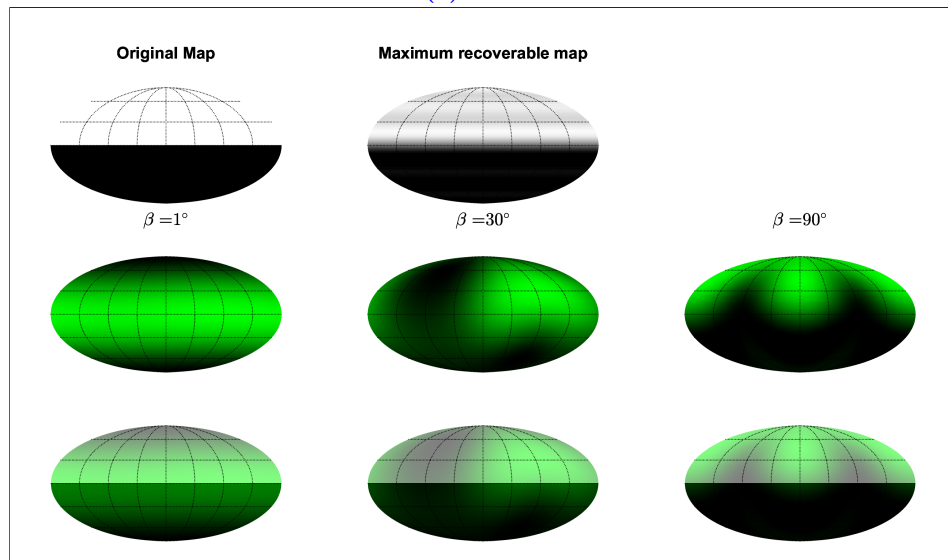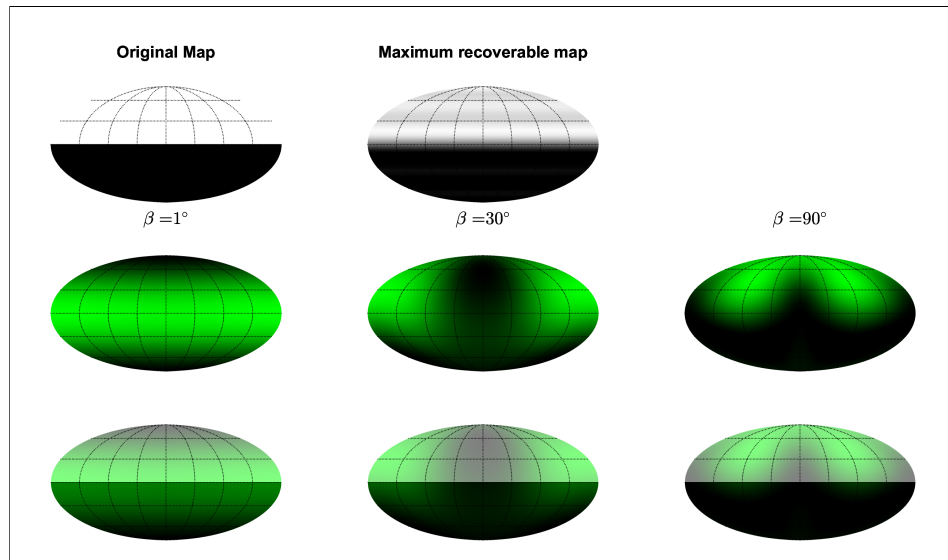
Figure B.2: *Recovery of the map of Unit-Θ for $\alpha = 0°, 90°$, and $180°$. In the top row, one can see the original surface, along with the best obtainable surface. In the second row, one can see the reconstructed maps for $\beta = 1°, 30°$, and $90°$ in the first, second and third column respectively. These reconstructions are shown superimposed on the original map in the third row.*
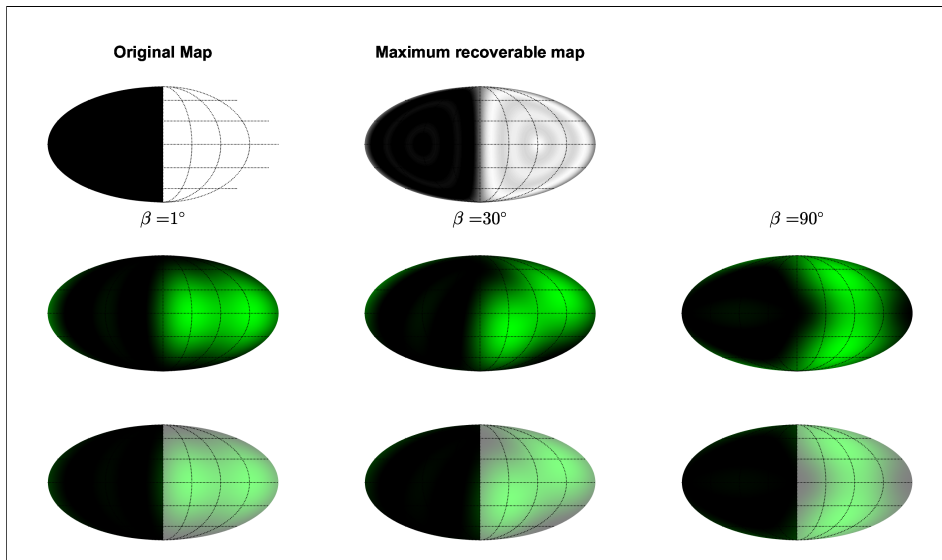
(a) $\alpha = 0°$
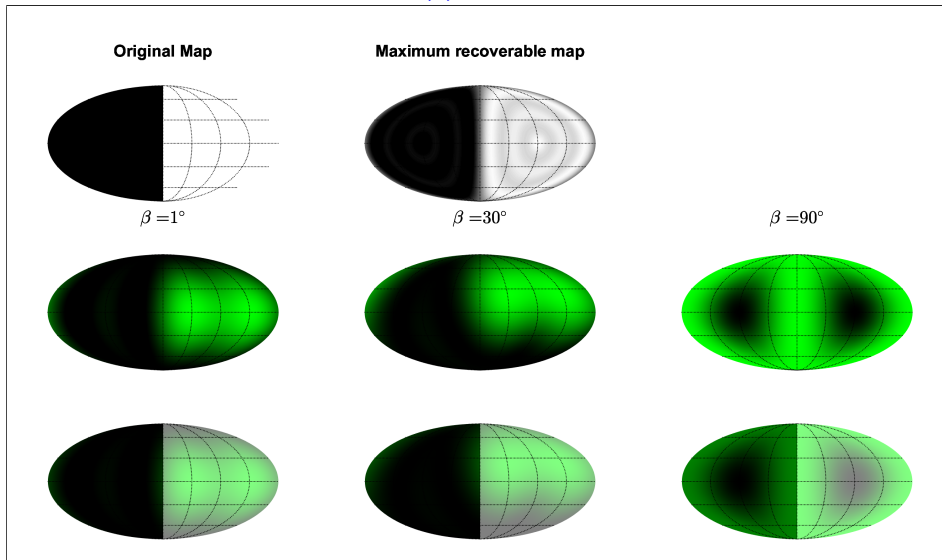
(b) $\alpha = 90°$
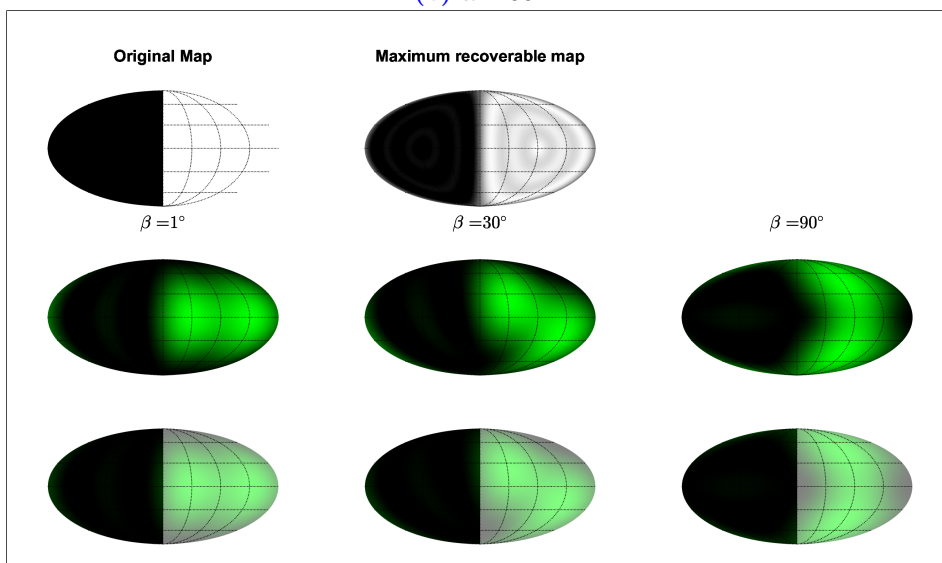
(c) $\alpha = 180°$

Figure B.3: *Recovery of the map of Unit-Φ for $\alpha = 0°, 90°$, and $180°$. In the top row, one can see the original surface, along with the best obtainable surface. In the second row, one can see the reconstructed maps for $\beta = 1°, 30°$, and $90°$ in the first, second and third column respectively. These reconstructions are shown superimposed on the original map in the third row.*
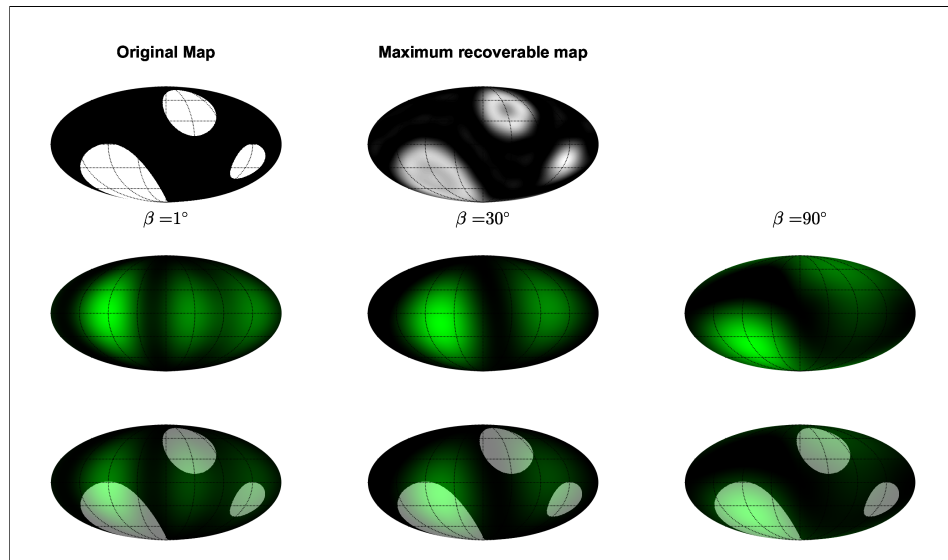
(a) $\alpha = 0°$
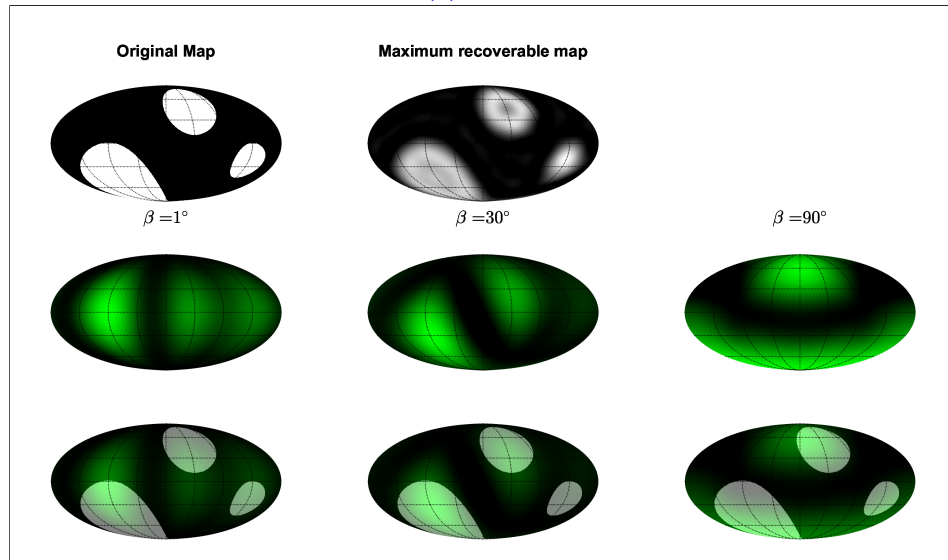
(b) $\alpha = 90°$
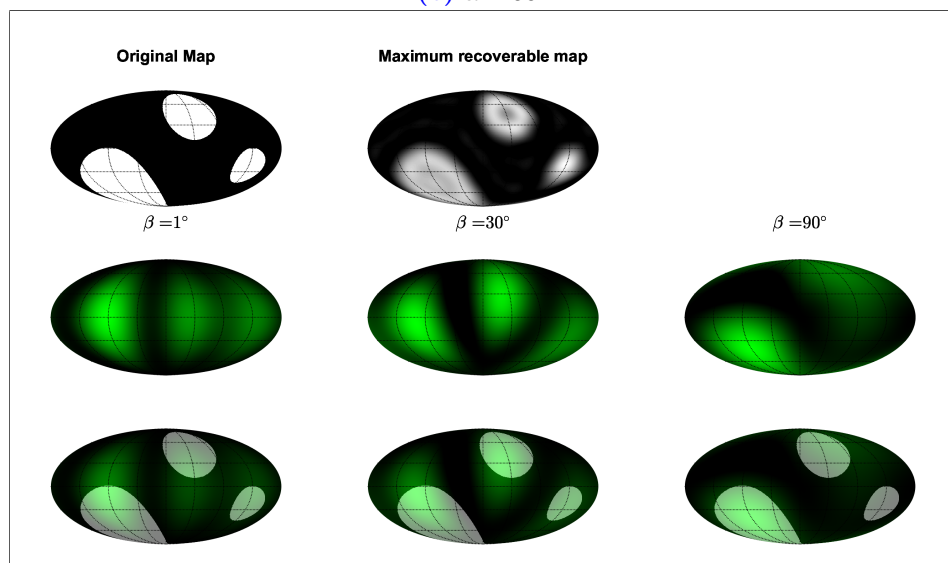
(c) $\alpha = 180°$

Figure B.4: *Recovery of the map of the circle planet for $\alpha = 0°, 90°$, and $180°$. In the top row, one can see the original surface, along with the best obtainable surface. In the second row, one can see the reconstructed maps for $\beta = 1°, 30°$, and $90°$ in the first, second and third column respectively. These reconstructions are shown superimposed on the original map in the third row.*
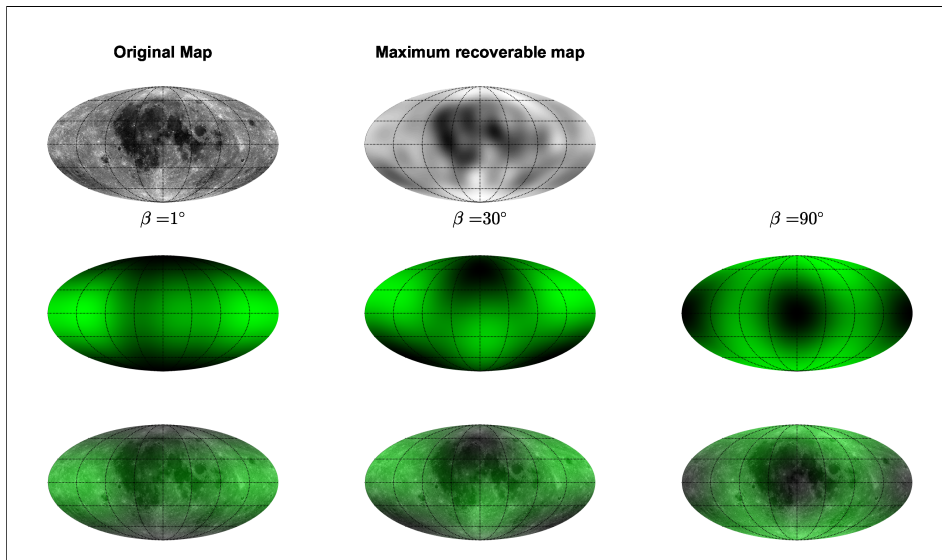
(a) $\alpha = 0°$
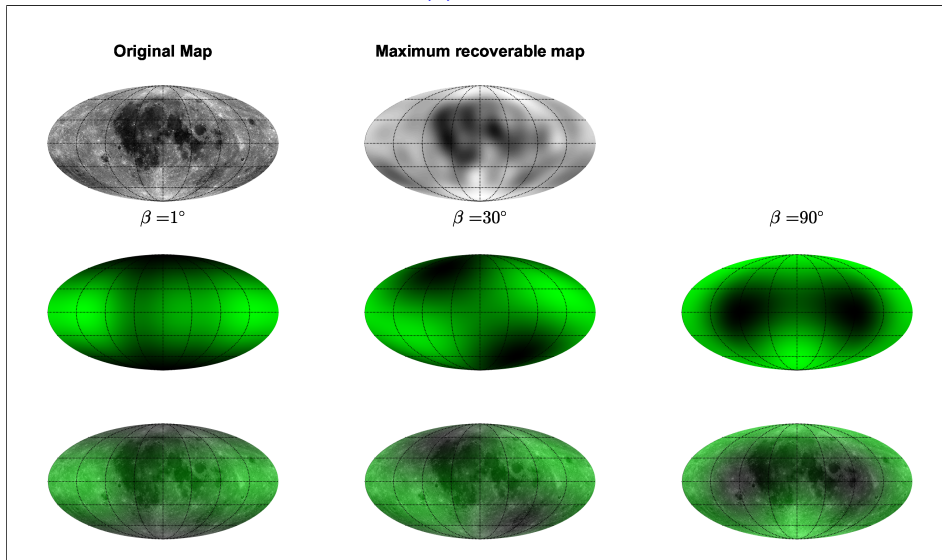
(b) $\alpha = 90°$
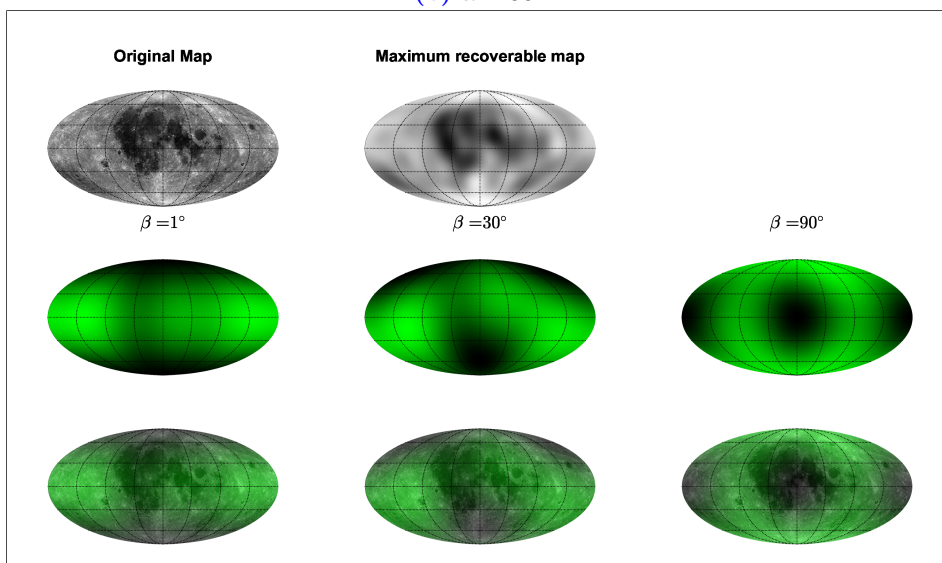
(c) $\alpha = 180°$

Figure B.5: *Recovery of the map of the Moon for $\alpha = 0°, 90°$, and $180°$. In the top row, one can see the original surface, along with the best obtainable surface. In the second row, one can see the reconstructed maps for $\beta = 1°, 30°$, and $90°$ in the first, second and third column respectively. These reconstructions are shown superimposed on the original map in the third row.*
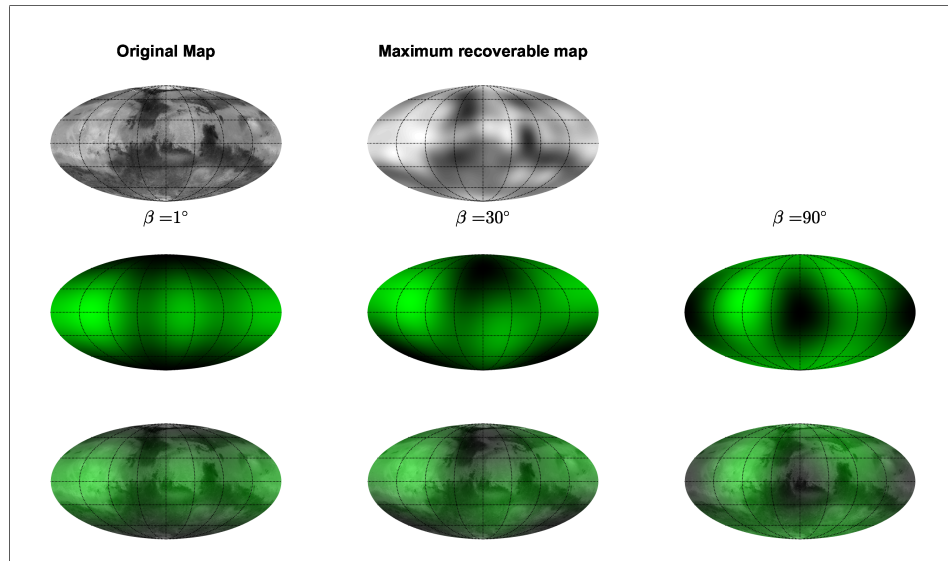
(a) $\alpha = 0°$
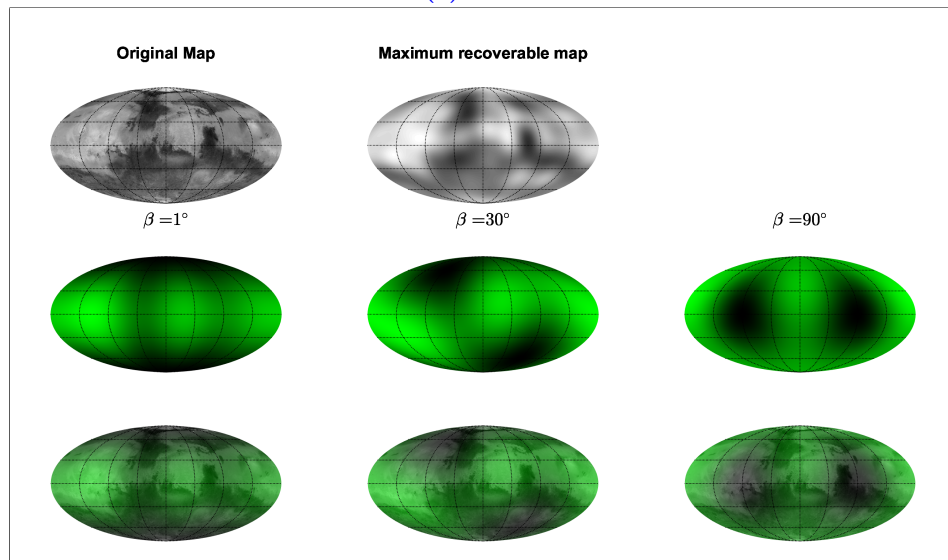
(b) $\alpha = 90°$
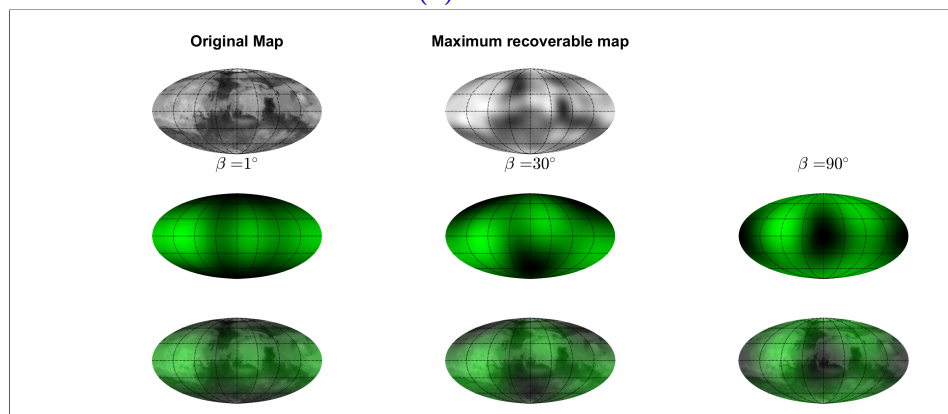
(c) $\alpha = 180°$

Figure B.6: *Recovery of the map of Mars for $\alpha = 0°, 90°$, and $180°$. In the top row, one can see the original surface, along with the best obtainable surface. In the second row, one can see the reconstructed maps for $\beta = 1°, 30°$, and $90°$ in the first, second and third column respectively. These reconstructions are shown superimposed on the original map in the third row.*
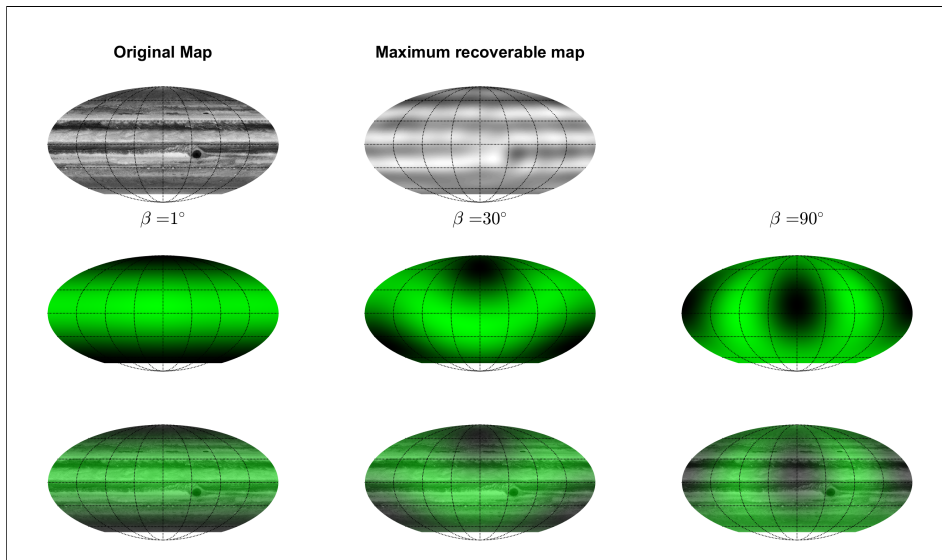
(a) $\alpha = 0°$
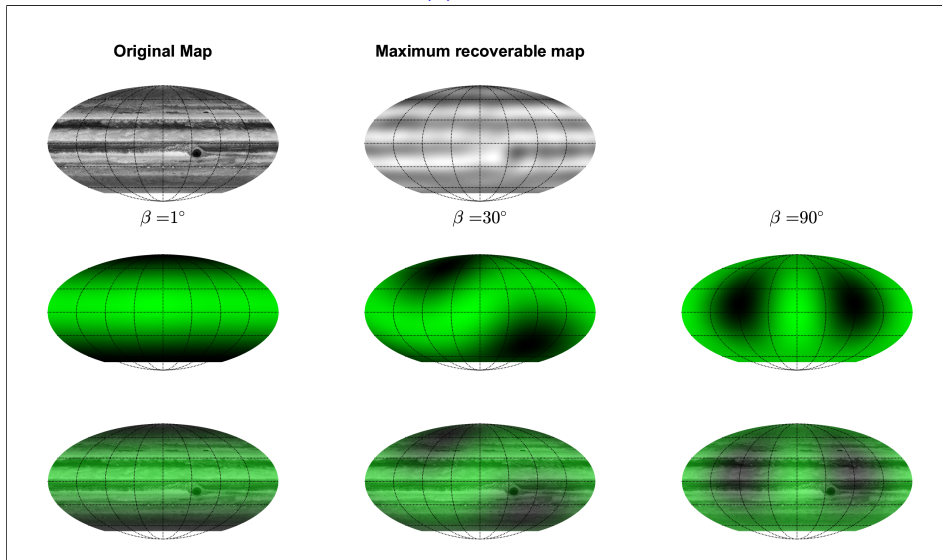
(b) $\alpha = 90°$
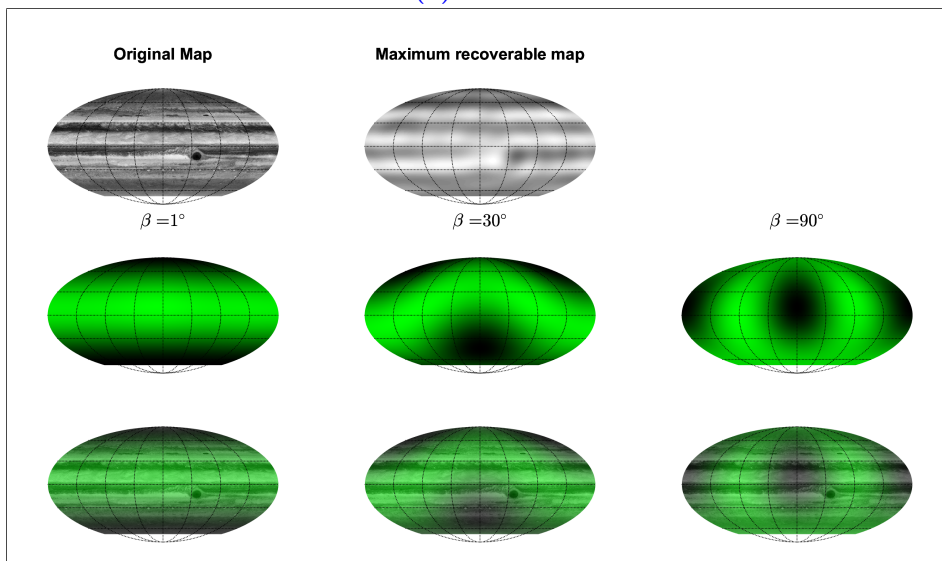
(c) $\alpha = 180°$

Figure B.7: *Recovery of the map of Jupiter for $\alpha = 0°, 90°$, and $180°$. In the top row, one can see the original surface, along with the best obtainable surface. In the second row, one can see the reconstructed maps for $\beta = 1°, 30°$, and $90°$ in the first, second and third column respectively. These reconstructions are shown superimposed on the original map in the third row.*

Appendix C

Additional recovered maps for face-on observation

In chapter 4, we recovered the map of Earth for known axial tilt β. Due to the way the continents are aligned, it is not always visible whether or not the result is acceptable, so the maps of the planets with constant albedo along the latitude and longitude have been used. These are the same planets as in Appendix B.
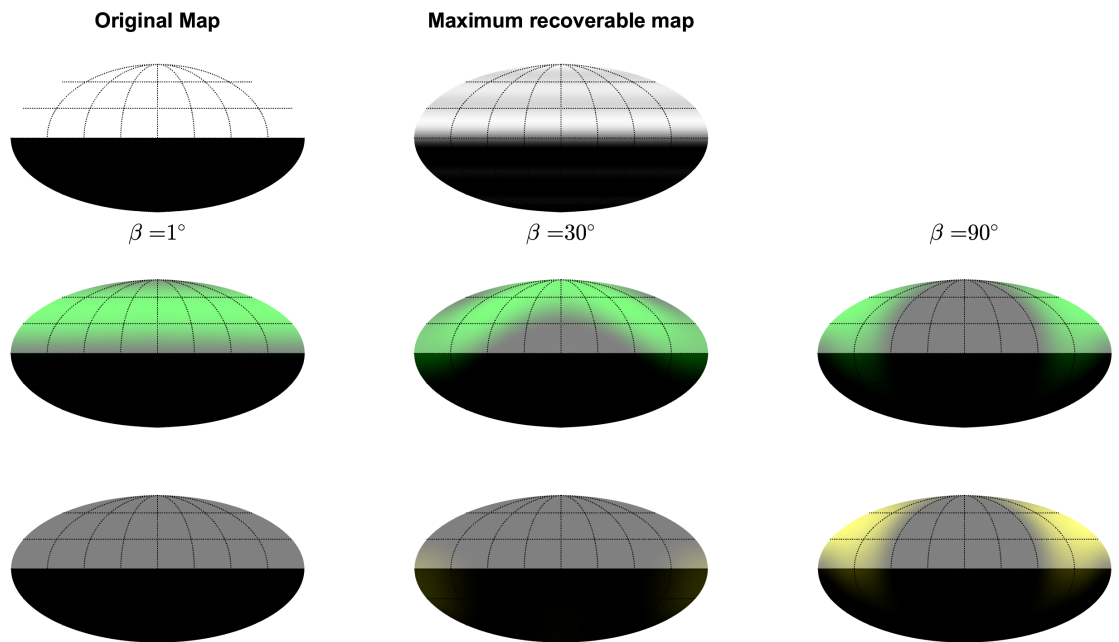
Figure C.1: *Reconstruction of UnitΘ's albedo map for face-on observation. In the first row, the original map and the map with spherical harmonics up to $l = 10$ are plotted. In the second and third row, the reconstructed maps for observations of the north-, and south-pole respectively are plotted superimposed on the original map. This has been done for $\beta = 1°, 30°$, and $90°$ in the first, second and third column respectively.*
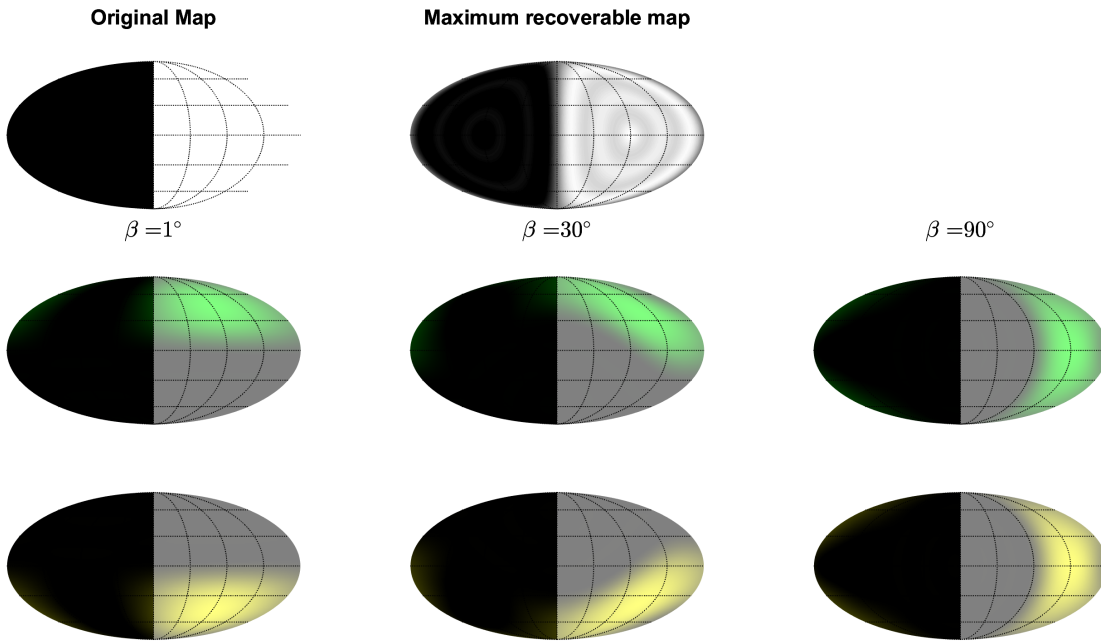
Figure C.2: *Reconstruction of UnitΦ's albedo map for face-on observation. In the first row, the original map and the map with spherical harmonics up to $l = 10$ are plotted. In the second and third row, the reconstructed maps for observations of the north-, and south-pole respectively are plotted superimposed on the original map. This has been done for $\beta = 1°, 30°$, and $90°$ in the first, second and third column respectively.*
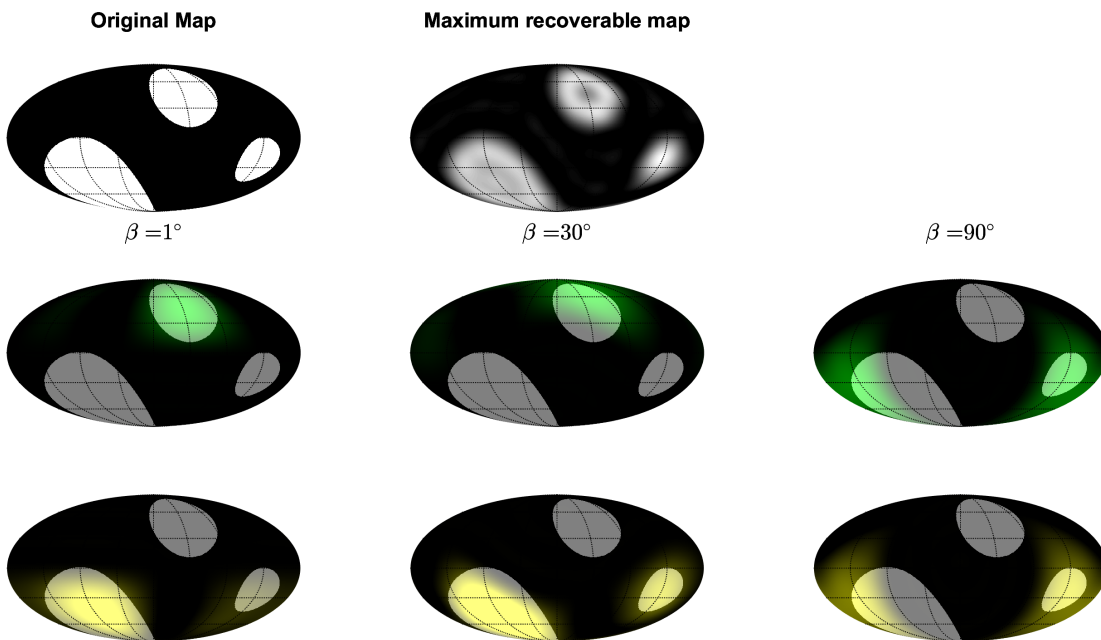
Figure C.3: *Reconstruction of Circles's albedo map for face-on observation. In the first row, the original map and the map with spherical harmonics up to $l = 10$ are plotted. In the second and third row, the reconstructed maps for observations of the north-, and south-pole respectively are plotted superimposed on the original map. This has been done for $\beta = 1°, 30°$, and $90°$ in the first, second and third column respectively.*
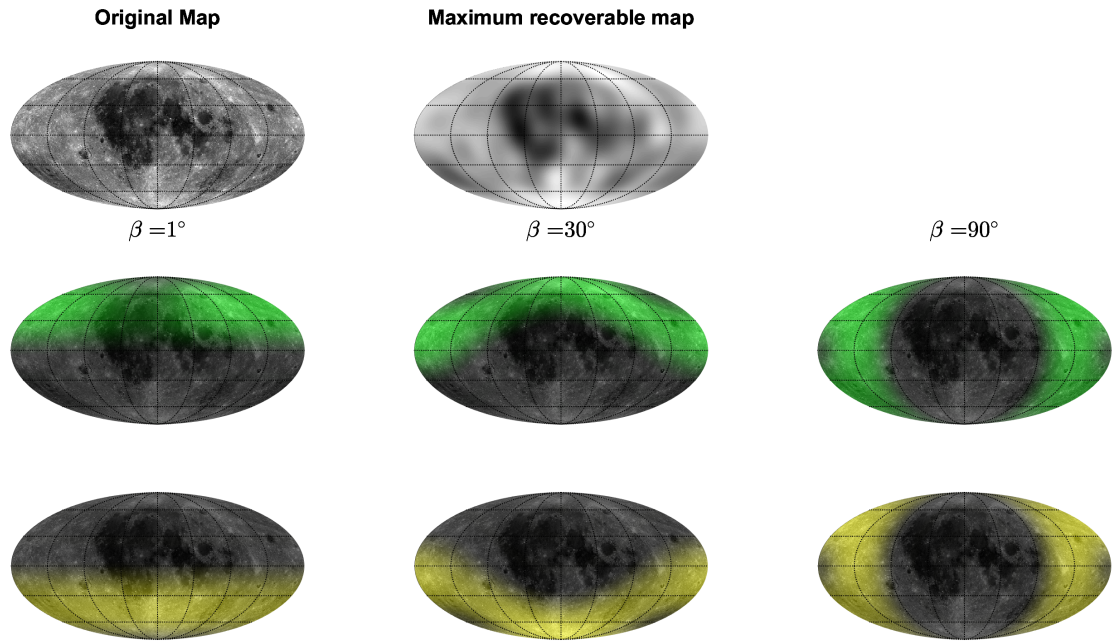
Figure C.4: *Reconstruction of Moon's albedo map for face-on observation. In the first row, the original map and the map with spherical harmonics up to $l = 10$ are plotted. In the second and third row, the reconstructed maps for observations of the north-, and south-pole respectively are plotted superimposed on the original map. This has been done for $\beta = 1°, 30°,$ and $90°$ in the first, second and third column respectively.*
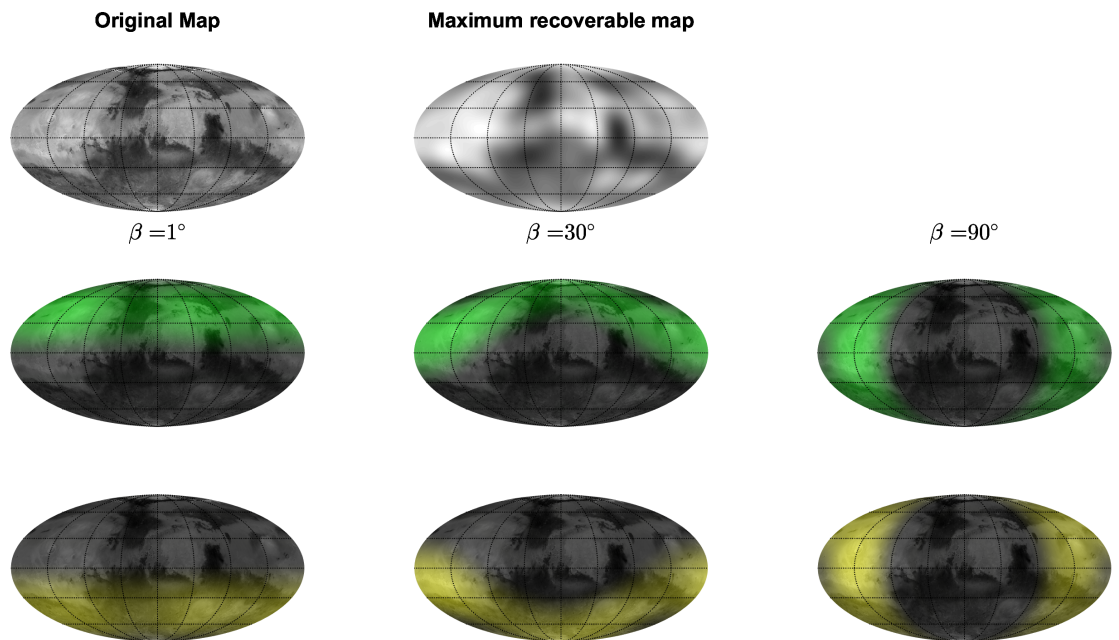
Figure C.5: *Reconstruction of Mars's albedo map for face-on observation. In the first row, the original map and the map with spherical harmonics up to $l = 10$ are plotted. In the second and third row, the reconstructed maps for observations of the north-, and south-pole respectively are plotted superimposed on the original map. This has been done for $\beta = 1°, 30°,$ and $90°$ in the first, second and third column respectively.*
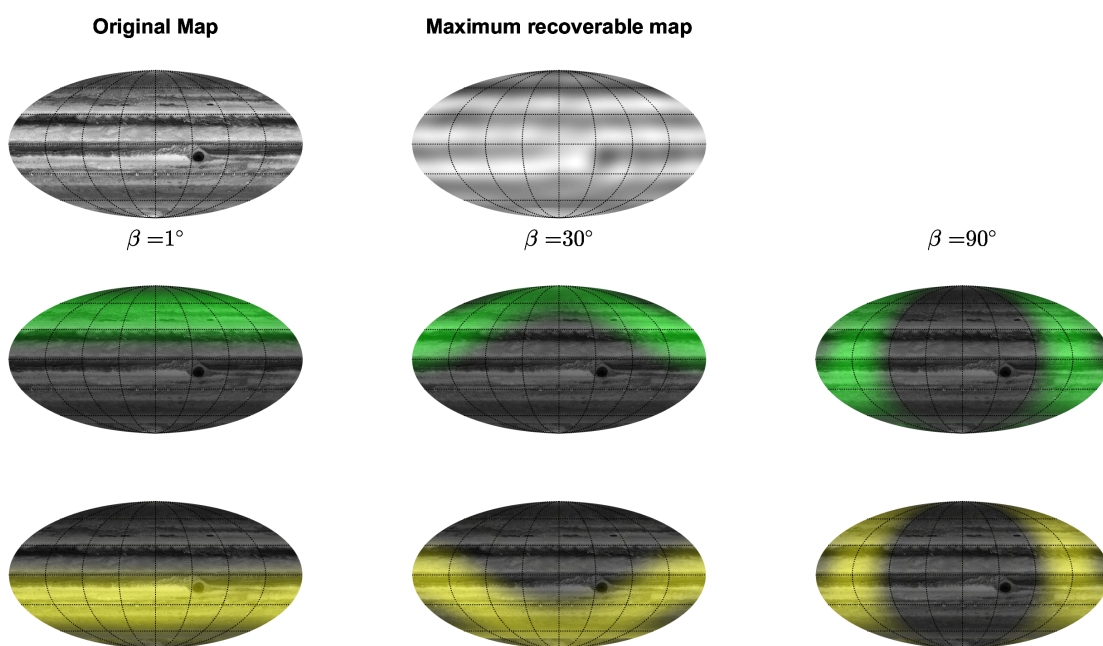
Figure C.6: *Reconstruction of Jupiter's albedo map for face-on observation. In the first row, the original map and the map with spherical harmonics up to $l = 10$ are plotted. In the second and third row, the reconstructed maps for observations of the north-, and south-pole respectively are plotted superimposed on the original map. This has been done for $\beta = 1°, 30°,$ and $90°$ in the first, second and third column respectively.*

Appendix D

Least squares, linearized

In chapter 4, we looked at alternative methods of recovering the axial tilt. We needed this because the column space of A did not change with the axial tilt. If this were the case, these methods would be redundant. Here, we present a method that could have been used. It relies on the same principle of the from section 3.7, but incorporates unknown tilt.

We start from the problem of section 3.7. The problem looks like:

$$\hat{\beta} = \underset{\beta \in [0,\pi]}{\arg\min} \|\mathbf{f} - A(\beta)\hat{\mathbf{M}}\|_2^2 \tag{D.1}$$

where $\hat{\mathbf{M}}$ is the best estimate for $\mathbf{M}$ given a value of β. The square in equation D.1 in not necessary, but makes calculations easier.

There are two equations we can use to determine $\hat{\beta}$ and $\hat{\mathbf{M}}$, we need to be in a minimum of $\|\mathbf{f} - A(\beta)\hat{\mathbf{M}}\|_2^2$, so we use partial derivatives and set them equal two 0. This can be interpreted with 2.5. We get the system of equations

$$\begin{cases} \frac{\partial}{\partial \hat{\mathbf{M}}} \|\mathbf{f} - A(\beta)\hat{\mathbf{M}}\|_2^2 &= 0 \\ \frac{\partial}{\partial \beta} \|\mathbf{f} - A(\beta)\hat{\mathbf{M}}\|_2^2 &= 0 \end{cases} \tag{D.2}$$

now, there is a intermediate step we need to make. We do not know the partial derivative of A to β because it contains the Wigner matrix, and even if we would, solving this equation would be hard if not impossible. To solve this, we linearize $A(\beta)$ in β, resulting in $A \approx A_0 + \beta A_1$. Substituting this for A gives the system of equations

$$\begin{cases} (A_0 + \beta A_1)^T (\mathbf{f} - (A_0 + \beta A_1)) = 0 \\ \hat{\mathbf{M}}^T A_1^T (\mathbf{f} - (A_0 + \beta A_1)\hat{\mathbf{M}}) = 0 \end{cases}$$

Solving this for β gives

$$\hat{\beta} = \frac{\hat{\mathbf{M}}^T A_1^T \mathbf{f} - \hat{\mathbf{M}}^T A_1^T A_0 \hat{\mathbf{M}}}{\hat{\mathbf{M}}^T A_1^T A_1 \hat{\mathbf{M}}}$$

and substituting this back gives an expression for $\hat{\mathbf{M}}$:

$$\hat{\mathbf{M}} = \left[(A_0 + \beta A_1)^T (A_0 + \beta A_1) \right]^{-1} (A_0 + \beta A_1)^T \mathbf{f}$$

and we recognize over here our old friend, the pseudoinverse of $A_0 + \beta A_1$. After simplifying, the system of equations we have is:

$$\begin{cases} \hat{\beta} = \frac{(A_1 \hat{\mathbf{M}})^T (\mathbf{f} - A_0 \hat{\mathbf{M}})}{\|A_1 \hat{\mathbf{M}}\|_2} \\ \hat{\mathbf{M}} = (A_0 + \beta A_1)^+ \mathbf{f} \end{cases} \tag{D.3}$$

This system of equations cannot be solved further. A solution could be found by iterating, starting with $\beta = 0$.

Appendix E

Code

All of the code that has been used in this report is available on request at:
`S.J.M.vanOosterom@student.tudelft.nl`